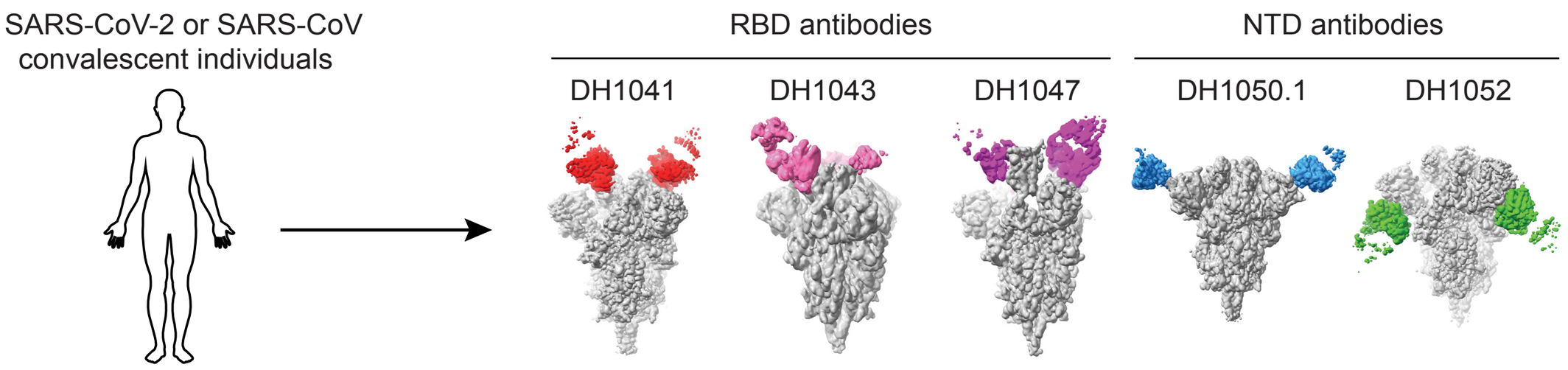
SARS-CoV-2 or SARS-CoV convalescent individuals
RBD antibodies
NTD antibodies
DH1041
DH1043
DH1047
DH1050.1
DH1052

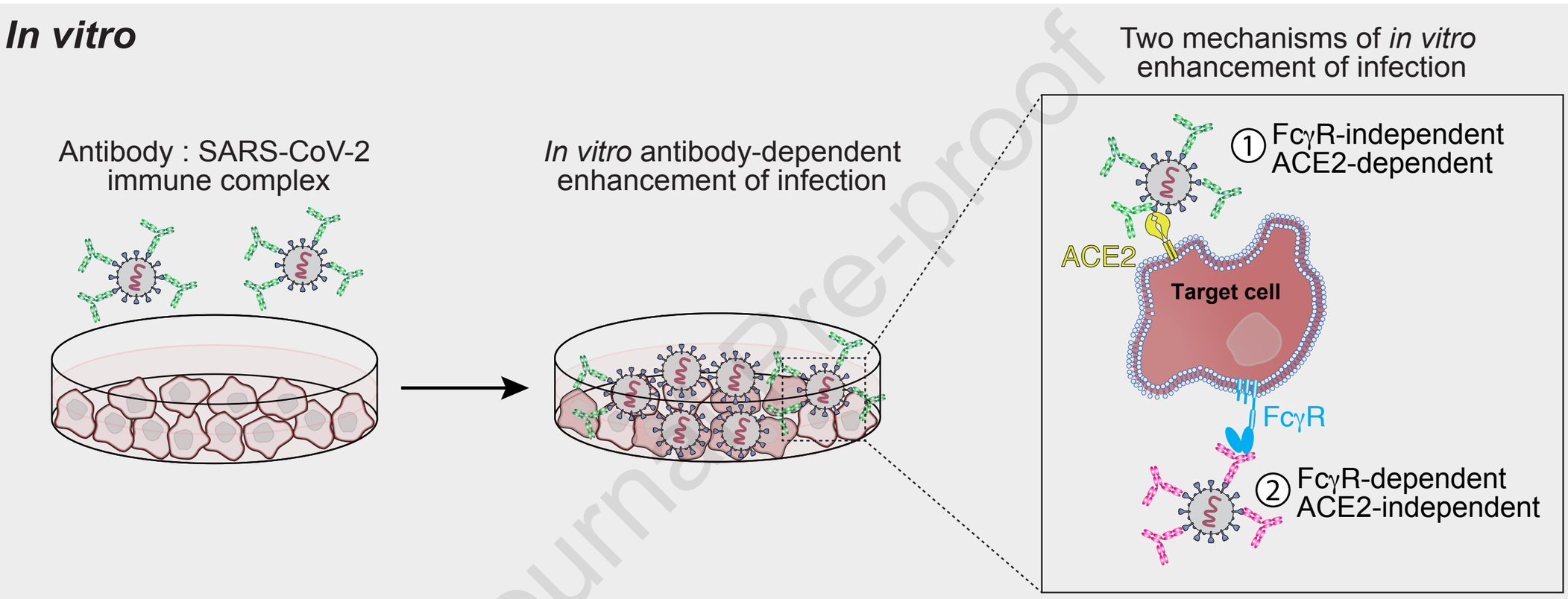
In vitro
Antibody : SARS-CoV-2 immune complex
In vitro antibody-dependent enhancement of infection
Two mechanisms of in vitro enhancement of infection
① FcγR-independent ACE2-dependent
ACE2
Target cell
FcγR
② FcγR-dependent ACE2-independent

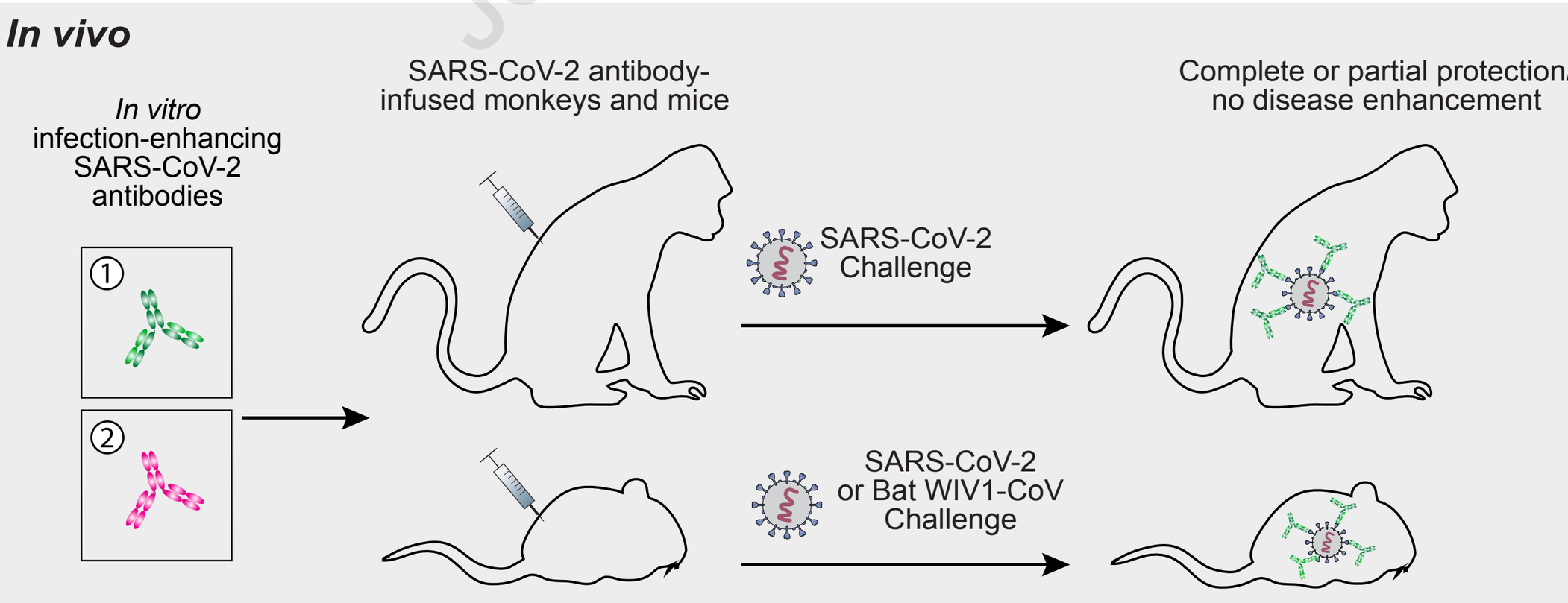
In vivo
In vitro infection-enhancing SARS-CoV-2 antibodies
①
②
SARS-CoV-2 antibody-infused monkeys and mice
SARS-CoV-2 Challenge
SARS-CoV-2 or Bat WIV1-CoV Challenge
Complete or partial protection/ no disease enhancement

In vitro and *in vivo* functions of SARS-CoV-2 infection-enhancing and neutralizing antibodies

Dapeng Li[1,2,15], Robert J. Edwards[1,2,15], Kartik Manne[1,2,15], David R. Martinez[3,15], Alexandra Schäfer[3,15], S. Munir Alam[1,2], Kevin Wiehe[1,2], Xiaozhi Lu[1,2], Robert Parks[1,2], Laura L. Sutherland[1,2], Thomas H. Oguin III[1,2], Charlene McDanal[4], Lautaro G. Perez[4], Katayoun Mansouri[1,2], Sophie M. C. Gobeil[1,2], Katarzyna Janowska[1,2], Victoria Stalls[1,2], Megan Kopp[1,2], Fangping Cai[1,2], Esther Lee[1,2], Andrew Foulger[1,2], Giovanna E. Hernandez[1,2], Aja Sanzone[1,2], Kedamawit Tilahun[1,2], Chuancang Jiang[1,2], Longping V. Tse[3], Kevin W. Bock[4], Mahnaz Minai[4], Bianca M. Nagata[4], Kenneth Cronin[1,2], Victoria Gee-Lai[1,2], Margaret Deyton[1,2], Maggie Barr[1,2], Tarra Von Holle[1,2], Andrew N. Macintyre[1,2], Erica Stover[1,2], Jared Feldman[6], Blake M. Hauser[6], Timothy M. Caradonna[6], Trevor D. Scobey[3], Wes Rountree[1,2], Yunfei Wang[1,2], M. Anthony Moody[1,7], Derek W. Cain[1,2], C. Todd DeMarco[1,2], Thomas N. Denny[1,2], Christopher W. Woods[1,2,8], Elizabeth W. Petzold[8], Aaron G. Schmidt[6,9], I-Ting Teng[10], Tongqing Zhou[10], Peter D. Kwong[10,11], John R. Mascola[10], Barney S. Graham[10], Ian N. Moore[4], Robert Seder[10], Hanne Andersen[12], Mark G. Lewis[12], David C. Montefiori[5], Gregory D. Sempowski[1,2], Ralph S. Baric[3], Priyamvada Acharya[1,5], Barton F. Haynes[1,2,13,*], Kevin O. Saunders[1,5,13,14,16*]

[1]Duke Human Vaccine Institute, Duke University School of Medicine, Durham, NC 27710, USA

[2]Department of Medicine, Duke University School of Medicine, Durham, NC 27710, USA

[3]Department of Epidemiology, University of North Carolina at Chapel Hill, Chapel Hill, NC 27599, USA

[4]Infectious Disease Pathogenesis Section, Comparative Medicine Branch, National Institute of Allergy and Infectious Diseases, National Institutes of Health, Bethesda, MD 20892, USA.

[5]Department of Surgery, Duke University, Durham, NC 27710, USA

[6]Ragon Institute of MGH, MIT and Harvard, Cambridge, MA 02139, USA

[7]Department of Pediatrics, Duke University School of Medicine, Durham, NC 27710, USA

[8]Center for Applied Genomics and Precision Medicine, Duke University Medical Center, Durham, NC 27710, USA

[9]Department of Microbiology, Harvard Medical School, Boston, MA 02115, USA

[10]Vaccine Research Center, National Institute of Allergy and Infectious Diseases (NIAID), NIH, Bethesda, MD 20892, USA

[11]Department of Biochemistry and Molecular Biophysics, Columbia University, New York, NY 10032, USA

[12]BIOQUAL, Rockville, MD 20850, USA

[13]Department of Immunology, Duke University School of Medicine, Durham, NC 27710, USA

[14]Department of Molecular Genetics and Microbiology, Duke University School of Medicine, Durham, NC 27710, USA

[15]These authors contributed equally

[16]Lead Contact: kevin.saunders@duke.edu (K.O.S.)

[*]Correspondence: barton.haynes@duke.edu (B.F.H.) and kevin.saunders@duke.edu (K.O.S.)

Summary (150 words)

SARS-CoV-2 neutralizing antibodies (NAbs) protect against COVID-19. A concern regarding SARS-CoV-2 antibodies is whether they mediate disease enhancement. Here, we isolated NAbs against the receptor-binding domain (RBD) and the N-terminal domain (NTD) of SARS-CoV-2 spike from individuals with acute or convalescent SARS-CoV-2 or a history of SARS-CoV infection. Cryo-electron microscopy of RBD and NTD antibodies demonstrated function-specific modes of binding. Select RBD NAbs also demonstrated Fc receptor-γ (FcγR)-mediated enhancement of virus infection *in vitro*, while five non-neutralizing NTD antibodies mediated FcγR-independent *in vitro* infection enhancement. However, both types of infection-enhancing antibodies protected from SARS-CoV-2 replication in monkeys and mice. Three of 46 monkeys infused with enhancing antibodies had higher lung inflammation scores compared to controls. One monkey had alveolar edema and elevated bronchoalveolar lavage inflammatory cytokines. Thus, while *in vitro* antibody-enhanced infection does not necessarily herald enhanced infection *in vivo*, increased lung inflammation can rarely occur in SARS-CoV-2 antibody-infused macaques.

Keywords

SARS-CoV-2, COVID-19, neutralizing antibody, receptor-binding domain, N-terminal domain, electron micrograph, *in vivo* protection, infection enhancement

Introduction

The severe acute respiratory syndrome coronavirus 2 (SARS-CoV-2) has caused a global pandemic with over 157 million cases and 3 million deaths (https://coronavirus.jhu.edu). While the ultimate solution to control the COVID-19 pandemic is a safe and effective vaccine, neutralizing Ab (NAb) prophylaxis or treatment of infection may help to control the pandemic (Graham, 2020; Sempowski et al., 2020). Prophylactic or therapeutic use of SARS-CoV-2 NAbs in non-human primates (Baum et al., 2020a; Jones et al., 2020; Zost et al., 2020a) or rodent models (Hassan et al., 2020; Rogers et al., 2020; Wu et al., 2020) have protected against SARS-CoV-2 infection. Potent SARS-CoV-2 NAbs reported to date predominantly target the RBD region (Baum et al., 2020b; Brouwer et al., 2020; Cao et al., 2020; Hansen et al., 2020; Ju et al., 2020; Liu et al., 2020a; Pinto et al., 2020; Robbiani et al., 2020; Rogers et al., 2020; Shi et al., 2020; Wrapp et al., 2020a; Wu et al., 2020). In contrast, neutralizing SARS-CoV-2 NTD antibodies (Abs) exhibit more modest neutralization potency (Brouwer et al., 2020; Chi et al., 2020; Wec et al., 2020; Zost et al., 2020a; Zost et al., 2020b).

A safety concern for clinical use of antibodies is antibody-dependent enhancement (ADE) of infection. ADE *in vitro* has been reported for respiratory syncytial virus vaccination, dengue virus vaccination, or dengue virus infection (Arvin et al., 2020). ADE is often mediated by Fc receptors for IgG (FcγRs), complement receptors (CRs) or both, and is most commonly observed in monocytes/macrophages and B cells (Iwasaki and Yang, 2020; Ubol and Halstead, 2010). *In vitro* studies have demonstrated FcγR-mediated ADE of SARS-CoV infection of ACE2-negative cells (Jaume et al., 2011; Kam et al., 2007; Wan et al., 2020; Wang et al., 2014; Yilla et al., 2005; Yip et al., 2016; Yip et al., 2014). Additional research has demonstrated FcγR-independent infection enhancement of SARS-CoV in Vero cells, and isolated an Ab that may have enhanced lung viral load and pathology *in vivo* (Wang et al., 2016). The ability of SARS-CoV-2 S Abs to mediate infection enhancement *in vivo* is unknown, but is a theoretical concern for COVID-19 vaccine development (Arvin et al., 2020; Bournazos et al., 2020; Haynes et al., 2020; Iwasaki and Yang, 2020).

Here, we identified potent *in vitro* neutralizing RBD and NTD Abs as well as *in vitro* infection-enhancing RBD and NTD Abs from individuals infected with SARS-CoV or SARS-CoV-2. Negative stain electron microscopy (NSEM) and cryo-electron microscopy (cryo-EM) revealed distinct binding patterns and the precise epitopes of infection-enhancing and neutralizing Abs. *In vitro* studies demonstrated that select RBD Abs mediated FcγR-dependent infection enhancement, whereas the NTD Abs induced FcγR-independent infection enhancement.

However, using monkey and mouse models of SARS-CoV-2 infection, none of the *in vitro* infection-enhancing Abs enhanced SARS-CoV-2 virus replication or infectious virus in the lung *in vivo*. Three of 46 monkeys had lung pathology or bronchoalveolar lavage (BAL) cytokine levels greater than controls. However, repeat studies with dose ranges of *in vitro* enhancing Abs did not increase lung pathology. Thus, *in vitro* infection-enhancing RBD and NTD Abs controlled virus *in vivo* and was rarely associated with enhanced lung pathology.

RESULTS

Isolation of neutralizing and infection-enhancing SARS-CoV-2 Abs

SARS-CoV-2-reactive monoclonal Abs from plasmablasts or SARS-CoV-2-reactive memory B cells were isolated (Liao et al., 2009; Liao et al., 2013) from a SARS-CoV-2 infected individual 11, 15 and 36 days post-onset of symptoms. To identify neutralizing Abs against both SARS-CoV and SARS-CoV-2, SARS-CoV-2 S-reactive B cells were isolated from an individual infected with SARS-CoV ~17 years prior to sample collection (***Figures 1A-B, S1A-D***). From 1,737 total B cells, we isolated 463 Abs that bound to SARS-CoV-2 S or nucleocapsid proteins in high-throughput binding screens (***Figure 1C; Table S1***). We selected 187 Abs using high binding magnitude, cross-reactivity with human CoVs, high somatic mutation frequency, and long HCDR3 as selection criteria. Downselected Abs were examined for neutralization of SARS-CoV-2 pseudovirus and replication-competent SARS-CoV-2. Forty-four of 81 RBD Abs exhibited neutralization of SARS-CoV-2 pseudovirus or replication-competent virus (***Figures S1E-J; Tables S2***). Ten of forty-one NTD Abs neutralized SARS-CoV-2 in the 293T/ACE2 pseudovirus and plaque reduction assays, at an IC_{50} as low as 39 ng/mL (***Figures S1K-M; Tables S2***). In addition, 5 non-neutralizing NTD Abs enhanced SARS-CoV-2 pseudovirus infection in 293T/ACE2 and replication-competent SARS-CoV-2 nano-luciferase virus infection of Vero cells (***Figure 1D,E***) (Huo et al., 2020) . NTD Ab infection enhancement was dependent on ACE2 expression. Both ACE2-expressing 293T cells used for pseudovirus assays and Vero cells lack FcγR expression (Takada et al., 2007). Thus, NTD enhancement of SARS-CoV-2 infection was FcγR-independent.

To assess FcγR-dependent infection enhancement, 100 S-reactive IgG1 Abs were tested for their ability to facilitate SARS-CoV-2 infection of TZM-bl cells expressing various FcγRs, but lacking ACE2 and TMPRSS2 (***Tables S2)***. Three or five Abs enabled SARS-CoV-2 infection of TZM-bl cells expressing either FcγRI or FcγRIIb

respectively (***Figures 1F-J***). The antigen-binding fragments (Fabs) of these Abs did not mediate infection enhancement of TZM-bl cells expressing FcγRI or FcγRIIb, demonstrating Fc-dependence for enhancement (***Figures 1K-L***). Thus, RBD Abs can be either neutralizing in ACE2-expressing 293T cells, infection-enhancing in the FcγR-expressing TZM-bl cells, or both (***Figure 2A***). NTD Abs can either be neutralizing or infection-enhancing in the $ACE2^{+}$ 293T cells or VeroE6 cells (***Figure 2A***).

Characterization of infection-enhancing Spike Abs

We compared the phenotypes and binding modes of RBD Abs that either did not enhance or enhanced infection in order to elucidate differences between them. The selected RBD Abs neutralized SARS-CoV-2 pseudovirus and/or replication-competent virus in ACE2-expressing cells (***Figures 2A and S2***), despite five of these Abs mediating infection enhancement in ACE2-negative, FcγR-positive TZM-bl cells (***Figures 1F-L, 2A, and S2***). Both types of selected RBD Abs blocked ACE2 binding to S protein and both types of RBD Abs bound to S with high affinities (range = 0.1 to 9 nM)(***Table S3, Figure 2A***). Thus, the infection-enhancing or non-enhancing RBD Abs showed similarities in ACE2 blocking, affinity, and neutralization of ACE2-dependent SARS-CoV-2 infection (***Figure 2A***).

For six representative RBD Abs, we obtained NSEM reconstructions of Fabs in complex with stabilized S ectodomain trimer. Infection-enhancing RBD Abs DH1041 and DH1043 bound with a vertical approach (***Figure 2B***), parallel to the central axis of the S trimer, similar to non-infection-enhancing Abs DH1042 and DH1044 (***Figure 2C***). The epitopes of Abs DH1041, DH1042, and DH1043 overlapped with that of the ACE-2 receptor (Wec et al., 2020), consistent with their ability to block ACE-2 binding to S protein (***Figures 2A and S3A-B***). Their epitopes were similar to those of three previously described Abs, P2B-2F6 (Ju et al., 2020), H11-H4, and H11-D4 (***Figure S3C***) (Huo et al., 2020; Zhou et al., 2020a). The epitope of another non-infection-enhancing RBD Ab DH1044 was only slightly shifted relative to DH1041, DH1042 and DH1043 (***Figure 2C***), but resulted in DH1044 not blocking ACE2 binding (***Figures 2A and S3A-B***). The remaining two RBD Abs, DH1045 and DH1047, cross-reacted with both SARS-CoV and SARS-CoV-2 S (***Figures 2A and S2A-B***). DH1047 also reacted with bat and pangolin CoV spike proteins (***Figures 2A and S2A***). Although DH1047 mediated FcγR-dependent infection of TZM-bl cells and DH1045 did not, both Abs bound to RBD-up S conformations with a more horizontal

angle of approach (***Figures 2B-C and S3A***) (Pak et al., 2009). Thus, epitopes and binding angles of RBD Abs determined by NSEM did not discriminate between Abs that mediated FcγR-dependent infection enhancement and those that did not.

Next we characterized the Fabs of neutralizing NTD Abs DH1050.1 and DH1051 bound to stabilized S ectodomain with affinities of 16 and 19 nM respectively, whereas the infection-enhancing Ab DH1052 bound with 294 nM affinity (***Table S3***). NSEM reconstructions obtained for nine NTD Abs showed that the FcγR-independent, infection-enhancing NTD Abs (DH1053-DH1056) bound to S with their Fab constant domains directed downward toward the virus membrane (***Figure 2D***), whereas the five neutralizing NTD-directed Abs (DH1048-DH1051) bound to S with the constant domain of the Fab directed upward away from the virus membrane (***Figure 2E***). The five neutralizing Abs bound the same epitope as Ab 4A8 (Chi et al., 2020), with three of the five having the same angle of approach and heavy chain gene segment (V_H1-24) as 4A8 (***Figure S3D-F*** and ***Table S2***) (Chi et al., 2020). These NTD Abs may constitute a neutralizing Ab class that can be elicited in multiple individuals. Thus, S protein Ab epitopes and binding modes were associated with infection-enhancing activity of NTD Abs.

Competition between infection-enhancing and non-infection enhancing Abs

To determine whether infection-enhancing Abs could compete with non-infection-enhancing Abs for binding to S ectodomain, we performed surface plasmon resonance (SPR) competitive binding assays. RBD Abs segregated into two clusters, where Abs within a cluster blocked each other and Abs in different clusters did not block each other (***Figures 3A***). One cluster included Abs DH1041, DH1043 and DH1044, and the other cluster included Abs DH1046 and DH1047. NSEM reconstructions showed combinations of DH1041 and DH1047 Fabs or DH1043 and DH1047 Fabs bound simultaneously to different epitopes of the stabilized S trimer (***Figure 3B***).

NTD Abs also segregated into two clusters where one cluster included neutralizing NTD Abs and a second cluster included non-neutralizing NTD Abs (***Figures 3A and 3C***). NSEM reconstructions confirmed that the Fabs of neutralizing NTD Ab DH1050.1 and infection-enhancing NTD Ab DH1052 could simultaneously bind to distinct epitopes on a single SARS-CoV-2 S trimer (***Figure 3D***). DH1054 was unique as it was able to block both infection-enhancing and neutralizing NTD Abs (***Figures 3C***).

NTD Abs did not compete with RBD Abs for binding to S trimer (***Figure 3A***), suggesting in a polyclonal mixture of Abs, the SARS-CoV-2 S trimer could bind both RBD and NTD Abs. NSEM showed that 1 or 2

different neutralizing RBD Abs (DH1043 and DH1047) could bind to the same S protomer as neutralizing NTD Abs DH1050.1 or DH1051 (***Figure 3E***,***F***). Thus, in the presence of a polyclonal Ab response, S trimer could be bound by multiple RBD and NTD neutralizing Ab Fabs.

FcγR-independent infection-enhancement in the presence of neutralizing Abs

Structural determination of Ab binding modes demonstrated that certain infection-enhancing Abs and non-infection enhancing Abs bound to distinct epitopes on the same S protomer (***Figures 3A-F***). Infection-enhancing Ab DH1052 and neutralizing RBD Ab DH1041 were isolated from the same individual. We hypothesized that infection outcome would be dependent on which Ab was present at the highest concentration. When DH1041 neutralization was assessed in the presence of 1,325-fold excess of Ab DH1052, infection enhancement was observed when DH1041 concentration was below 10 ng/mL (***Figures 3G and S4A-C***). A nearly identical result was obtained when we examined neutralization by DH1043 (***Figures 3H and S4A-C***). In 21 SARS-CoV-2-infected humans, RBD and NTD serum IgG titers were comparable (***Figures S4D-E***). Moreover, the prevalence of DH1052 versus DH1041 Abs was assessed using blocking assays and found to be only modestly higher for DH1052 (***Figure S4F***). Thus, a ~1000-fold excess of infection-enhancing NTD Ab was required to out-compete the effect of a potent RBD neutralizing Ab *in vitro*, but such excess amounts of DH1052 was not observed during natural infection (***Figures 3G-H and S4D-F***).

Cryo-EM structural determination of RBD and NTD-directed Ab epitopes

To visualize atomic level details of their interactions with the S protein, cryo-EM was used for structural determination of selected representative Abs from the panels of RBD and NTD-directed Abs. For all three RBD-directed Abs, the cryo-EM datasets revealed heterogeneous populations of S ectodomain "2P" (S-2P) (Wrapp et al., 2020b) with at least one RBD in the "up" position (***Figure 4 and Data S1***). We did not find any unliganded S or any 3-RBD-down S population, although unliganded S-2P consistently shows a 1:1 ratio of 1-RBD-up and 3-RBD-down populations (Henderson et al., 2020; Walls et al., 2020). All S-2P trimers were stoichiometrically bound to three Fabs, with Abs bound to both up and down RBDs in an S-2P trimer.

We observed that the primary epitopes of DH1041 and DH1043 were centered on the Receptor Binding Motif (RBM; residues 483-506) of the RBD (***Figures 4A-B and Data S1***), providing structural basis for the ACE-2

blocking phenotype of these Abs. While DH1041 utilized its heavy chain complementarity determining regions (CDRs) to contact the RBM, the DH1043 paratope included both its heavy and light chains. In contrast, the epitope of Ab DH1047 was focused around the α2 and α3 helices and ß2 strand that are located outside the N-terminus of the RBM (***Figure 4C and Data S1***). DH1047 also contacted RBD residues 500-506 outside the RBM, and stacked against the N-terminal end of the α3 helix. The DH1047 paratope included heavy chain HCDR2, HCDR3 and light chain LCDR1 and LCDR3. The HCDR3 stacks against and interacts with the residues in the ß2 strand. Interactions with the ß2 strand are also mediated by HCDR2. Similar to DH1041 and DH1043, the DH1047 interacted with an "up" RBD conformation from an adjacent protomer although these interactions were not well-characterized due to disorder in that region.

We next determined cryo-EM structures of the NTD-directed neutralizing Abs, DH1050.1 (***Figure 4D***) and NTD-directed infection-enhancing Ab, DH1052 (***Figure 4E***), at 3.4 Å and 3.0 Å resolutions, respectively. The cryo-EM datasets of DH1050.1- and DH1052-bound complexes showed Fab bound to both 3-RBD-down and 1-RBD-up S-2P spikes (***Data S1***). Consistent with the NSEM reconstructions, the neutralizing Ab DH1050.1 and the non-neutralizing, infection-enhancing Ab DH1052 bound opposite faces of the NTD, with the epitope for the neutralizing Ab DH1050.1 facing the host cell membrane and the epitope for the non-neutralizing, infection-enhancing Ab DH1052 facing the viral membrane. The dominant contribution to the DH1050.1 epitope came from NTD loop region 140-158 that stacks against the Ab HCDR3 and extends farther into a cleft formed at the interface of the DH1050.1 HCDR1, HCDR2 and HCDR3 loops. The previously described NTD Ab 4A8 interacts with the same epitope in a similar manner as DH1050.1, with its elongated HCDR3 dominating interactions. Although, DH1050.1 and 4A8 (Chi et al., 2020) show a rotation relative to each other about the stacked HCDR3 and NTD 140-158 loops. The light chains of DH1050.1 and 4A8 do not contact the S protein, which is consistent with their diverse light chain gene origins (***Figure 4E and Data S1)***. The infection enhancing NTD-directed Ab DH1052 bound the NTD at an epitope facing the viral membrane and composed of residues spanning 27-32, 59-62 and 211-218, with all the CDR loops of both heavy and light chains involved in contacts with the NTD. We also observed contact of the Ab with the glycan at position 603, as well as the conformationally invariant SD2 region. Thus, we found that the RBD-directed antibodies isolated in this study influenced RBD dynamics and bound only to spike with at least one RBD in the up conformations, and in some cases, also induced the 2-RBD-up and 3-RBD-up spike

conformations. In contrast, the NTD-directed antibodies bound to both the 3-RBD-down and 1-RBD-up spikes that are present in the unliganded S-2P.

Effect of *in vitro* infection-enhancing and neutralizing NTD Abs in mouse and macaque models

Next, we assessed the effect of NTD infection-enhancing Ab DH1052 in a COVID-19 disease mouse model where aged BALB/c mice were challenged with the mouse-adapted SARS-CoV-2 MA10 strain (Leist et al., 2020a). DH1052 lacked neutralization of SARS-CoV-2 MA10 (***Figure S4G-H***). DH1052 or a control influenza Ab CH65 was given 12 hours prior to SARS-CoV-2 MA10 infection (***Figure 5A***). Throughout the four days of infection, DH1052-infused mice exhibited similar levels of body weight loss and higher survival than mice given CH65 (***Figures 5B-C***). In addition, DH1052-treated mice exhibited lower lung hemorrhagic scores, lower lung viral plaque-forming unit (PFU) titers and lower lung tissue subgenomic RNA (sgRNA) levels compared to control mice (***Figures 5D-F***). Therefore, DH1052 treatment resulted in less severe disease and reduced viral replication. FcR-mediated effector functions may have been the mechanism of suppression since DH1052 bound to mouse FcγRI and FcγRIV (***Table S4***).

We next examined the effect of infusion of NTD infection-enhancing Ab DH1052, NTD neutralizing Ab DH1050.1, or control Ab CH65 on SARS-CoV-2 infection in monkeys (Leist et al., 2020b; Rockx et al., 2020). Cynomolgus macaques were infused with 10 mg of Ab per kg body weight and three days later challenged intranasally and intratracheally with 10^5 PFU of SARS-CoV-2 (***Figure 5G***) (54). Human Ab infusion resulted in circulating concentrations ranging from 11 to 238 μg/mL in serum at day 2 post-challenge (***Figures 5H-I***). Sera with DH1050.1 neutralized SARS-CoV-2 pseudovirus and replication-competent virus, while serum containing DH1052 or CH65 did not neutralize (***Figures 5J-K***). Four of 5 macaques that received DH1052 had comparable lung inflammation to control CH65-infused macaques four days after infection (***Figures 5L and S5A***). However, one macaque (BB536A) administered DH1052 showed increased perivascular mononuclear inflammation, perivascular and alveolar edema (***Figure S5B***), and multiple upregulated BAL cytokines (***Table S5***). Immunohistologic analysis demonstrated alveolar and perivascular infiltration of M2-type macrophages in both monkey BB536A and a control monkey BB785E (***Figures S5C-E***). In contrast, macaques administered DH1050.1, a neutralizing NTD Ab, had lower lung inflammation (***Figures 5L and S5A***) and fewer infiltrating macrophages

(***Figures S5C-E***). Infusion of either DH1050.1 or DH1052 reduced viral nucleocapsid antigen (***Figures 5M and S5A)***, Envelope (E) gene sgRNA and nucleocapsid (N) gene sgRNA in the BAL (***Figures 5N-O***). In nasal swab fluid, DH1050.1 and DH1052 reduced E and N gene sgRNA in macaques with the reduction being significant when neutralizing Ab DH1050.1 was infused (***Figures 5P-Q***).

Since DH1052-mediated *in vitro* infection-enhancement increased as the Ab concentration increased (***Figures 1D-E***), we infused an additional 6 cynomolgus macaques with either 30 mg/kg of DH1052 or CH65 control Ab (***Figure S6A***). DH1052 infusion suppressed BAL viral load (***Figures S6B-D***), significantly reduced virus replication in nasal swab samples (***Figures S6E-G***), and showed no enhanced immunopathology or cytokine secretion (***Figures S6H-K, Table S5***). Thus, with high dose (30mg/kg) of DH1052 Ab, there was no infection enhancement. These results suggested that the lung pathology seen in monkey BB536A was rare and may not have been caused by Ab infusion.

FcγR-dependent, *in vitro* infection-enhancing RBD Abs do not enhance SARS-CoV-2 infection in mice

Next, we used a SARS-CoV-2 acquisition mouse model to investigate the *in vivo* relevance of RBD neutralizing Abs that also mediated *in vitro* infection-enhancement (***Figures 6A-B***). Aged BALB/c mice were injected intraperitoneally with 300 μg of Ab, and challenged with a SARS-CoV-2 mouse-adapted 2AA MA isolate 12 hours later (Dinnon et al., 2020). Mice received either *in vitro* infection-enhancing Ab DH1041, non-infection enhancing Ab DH1050.1, or a combination of both Abs. Administration of DH1041 alone or in combination with DH1050.1 protected all mice from detectable infectious virus in the lungs 48h after challenge (***Figure 6A***). In the setting of therapeutic treatment, administration of DH1041 alone or in combination with DH1050.1 12 hours after SARS-CoV-2 challenge significantly reduced lung infectious virus titers (***Figure 6B***). Thus, while RBD Ab DH1041 could mediate FcγR-dependent, *in vitro* infection enhancement, it protected mice from SARS-CoV-2 infection when administered prophylactically or therapeutically.

DH1046 and DH1047 are RBD Abs that cross-neutralize SARS-CoV, SARS-CoV-2 and bat WIV1-CoV (***Figures 2A***, ***S2A-B, S2I-L and 6C-E***). Both RBD Abs mediated FcγR-dependent, *in vitro* SARS-CoV-2 infection enhancement (***Figures 1F-L***). We assessed the ability of either DH1046 or DH1047 to enhance or protect against bat WIV1-CoV infection in HFH4-ACE2-transgenic mice (***Figures 6F-G***). Mice administered DH1046 or DH1047

before challenge had no detectable infectious virus in the lung, whereas control IgG administered mice had a mean titer of 84,896 PFU per lung lobe (***Figure 6F***). Administration of DH1047 after challenge eliminated detectable infectious virus in the lung in 3 of 5 mice (***Figure 6G***). Therapeutic administration of DH1046 reduced infectious virus titers 10-fold compared to negative control IgG (***Figure 6G***). Thus, DH1046 and DH1047 did not enhance infection *in vivo*, but rather protected mice from SARS-related bat coronavirus infection.

In vitro infection-enhancing RBD Abs in SARS-CoV-2-challenged nonhuman primates

Finally, we assessed RBD Ab infection-enhancement in cynomolgus macaques (***Figures 7A***). After Ab infusion at 10 mg/kg of body weight, serum human IgG concentrations reached 11-228 μg/mL at day 2 post-challenge (***Figures 7B-C***) and exhibited a wide range of neutralization potencies against SARS-CoV-2 (***Figures 7D-E***). Infusion of RBD Ab DH1041, DH1043, or DH1047 resulted in reduced lung inflammation, undetectable lung viral antigen (***Figures 7F-G and S5A***), and reduced sgRNA in the upper and lower respiratory tracts (***Figures 7H-K***). RBD Ab DH1046, a weaker neutralizing Ab compared to DH1041, DH1043 or DH1047 ***(Figure 2A***), did not enhance sgRNA E or N in BAL or nasal swab samples (***Figures 7H-K***), but protected only a subset of infused monkeys. Two DH1046-infused monkeys had increased lung inflammation scores due to increased total areas of inflammation compared to control Ab monkeys (***Figures 7F and S5A***), but had no evidence of perivascular or alveolar edema nor evidence of abnormal BAL cytokines (***Table S5***). Thus, these two animals had more lung involved with inflammatory macrophage infiltration but did not have pathological evidence of vascular leakage. Comparing the DH1046 group to the control IgG group, viral nucleocapsid antigen in the lung was reduced (***Figures 7G and S5A***). Thus, the weakly neutralizing Ab only partially limited virus replication and lung inflammation.

In vitro infection enhancement by RBD Abs was dependent on Ab concentration, with lower levels of Ab showing the highest magnitude of infection enhancement (***Figure 1G***). Therefore, we performed an additional passive infusion study with a series of different concentrations of DH1047 (***Figure S7A***). Cynomolgus macaques were infused with 5, 1, or 0.1 mg of DH1047 per kg of body weight resulting in a wide range of DH1047 concentrations in serum (***Figures S7B-C***). However, none of the groups of macaques had enhanced virus replication (although one monkey in the 0.1mg/kg group had higher BAL sgRNA E and N than controls) (***Figures***

S7D-G), lung inflammation (***Figures S7H-I)***, lung viral antigen (***Figures S7J-K***), or higher BAL inflammatory cytokines (***Table S5***) compared to the control IgG group.

Overall, 45 of 46 spike enhancing Ab-infused monkeys did not show enhanced virus replication in vivo, while 3 of 46 Ab-treated monkeys exhibited enhancement of lung pathology, with 1 of 46 Ab-treated monkeys had alveolar and perivascular edema and with elevated BAL inflammatory cytokines. In the case of the latter monkey, a follow-up study with 3 times the initial DH1052 Ab dose did not confirm DH1052 result in enhanced lung pathology after SARS-CoV-2 challenge.

DISCUSSION

Here, we assessed infection-enhancement by SARS-CoV-2 Abs and observed two different types of *in vitro* infection enhancement. First, RBD Abs mediated classical ADE that required FcγRs and Ab Fc for virus uptake (Lee et al., 2020). Previous studies have demonstrated that uptake of MERS-CoV or SARS-CoV has mostly been mediated by FcγRIIa on the surface of macrophages (Bournazos et al., 2020; Wan et al., 2020; Yip et al., 2016). In contrast, we identified SARS-CoV-2 RBD Abs utilized FcγRIIb or FcγRI. Second, non-neutralizing NTD Abs mediated FcγR-independent infection-enhancement in two different FcγR-negative, ACE2-expressing cell types. The mechanism of FcγR-negative *in vitro* enhancement remains unclear, but one previous study has reported that select NTD Abs can enhance S binding to ACE2 (Liu et al., 2020b).

Macrophages and other phagocytes are the target cells that take up MERS-CoV leading to infection-enhancement (Hui et al., 2020; Wan et al., 2020; Zhou et al., 2014). In contrast, neither SARS-CoV nor SARS-CoV-2 productively infect macrophages (Bournazos et al., 2020; Hui et al., 2020; Yip et al., 2016). However, a recent study demonstrated that alveolar macrophages harboring SARS-CoV-2 RNA produce T cell chemoattractants leading to T cell IFN-γ production that in turn, stimulates inflammatory cytokine release from alveolar macrophages (Grant et al., 2021). Why severe lung pathology and inflammatory cytokine production occurred in only 1 of 46 monkeys is unknown, but may relate to host-specific differences regulating inflammatory cytokine production (Bastard et al., 2020; Zhang et al., 2020). It is important to note that the one monkey that developed alveolar and perivascular edema and elevated BAL inflammatory cytokines could have been caused by Ab enhancement of disease, or could have been due to unknown factors that caused more severe disease in animal BB536A that were unrelated to DH1052 administration. That none of 6 animals infused with a higher dose

(30mg/kg) of DH1052 had enhanced pulmonary disease supports the hypothesis that the lung pathology may have been a severe case of COVID-19 lung disease unrelated to Ab infusion.

Previous studies with vaccine-induced Abs against SARS-CoV have also shown *in vitro* infection-enhancement, but no *in vivo* infection enhancement in hamsters (Kam et al., 2007). One explanation for this results may be that *in vitro* enhancing Abs may have the ability to suppress SARS-CoV-2 replication *in vivo* through non-neutralizing FcR-mediated Ab effector functions (Bournazos et al., 2020; Schafer et al., 2021). A recent study in a SARS-CoV-2 mouse model of acquisition suggested that Fc effector functions contribute to the protective activity of SARS-CoV-2 neutralizing Abs C104, C002, and C110 (Schafer et al., 2021). Thus, Ab effector functions may contribute to the outcome *in vivo*, but not be accounted for in SARS-CoV-2 enhancement or neutralization assays *in vitro*. Consistent with previous findings for human IgG (Dekkers et al., 2017), we observed that DH1052 Ab can bind to select murine FcγRs.

In vivo, SARS-CoV-2 S trimers circulate in the presence of a polyclonal Ab response. We observed bivalent and trivalent combinations of Fabs from RBD and NTD neutralizing Abs can recognize the same protomer of the S trimer. We speculate given the direction of the C-termini of the Fabs and molecular modeling that three IgGs targeting distinct epitopes may be able to interact with the same protomer, if the IgG hinge region is sufficiently flexible and the RBD is in an optimal up conformation for simultaneous engagement. Simultaneous engagement by RBD and NTD Abs could improve synergism of neutralization (Zost et al., 2020a), and avidity of the immune complexes for FcγRs on effector cells (Nagashima et al., 2011; Nagashima et al., 2008; Wang et al., 2017). These results indicate three epitopes that Ab prophylactics could target on RBD and NTD in order to occupy S trimers with multiple IgGs.

Limitations of the Study

Although rare enhanced immunopathology was observed in monkeys, it is difficult to predict whether this phenomenon will occur in the setting of human infection or vaccination. Furthermore RBD and NTD antibodies were the focus of this study, therefore whether antibodies of other specificities mediate ADE warrants further study. Additionally, the macaque model has a rather short course of infection, thus effects of SARS-CoV-2 antibody on persistent SARS-CoV-2 infection was not examined here.

Finally, administration of COVID-19 convalescent sera to over 35,000 COVID-19 patients have demonstrated the treatment to be safe and is not associated with enhanced disease (Joyner et al., 2020). Of greater importance is that both the Pfizer/BioNTech and Moderna mRNA-lipid nanoparticle (LNP) vaccine efficacy trials have completed and showed ~95% vaccine efficacy (Jackson et al., 2020; Polack et al., 2020). That the Moderna mRNA-LNP COVID-19 vaccine efficacy trial had 30 severe cases of COVID-19 occur—all in the placebo group (Baden et al., 2021), demonstrated that if ADE of infection or lung pathology will occur in humans with vaccination, it will be rare. A recent study demonstrated that suboptimal neutralizing Ab level is a significant predictor of severity for SARS-CoV-2 (Garcia-Beltran et al., 2020). Thus, even with the rarity of severe lung pathology associated with presence of anti-spike Ab in animal model studies reported here, it will be important to continue to monitor on-going COVID-19 vaccination for the possibility of vaccine associated enhanced disease when suboptimal neutralizing Ab titers are induced (Haynes et al., 2020).

ACKNOWLEDGMENTS

We thank the COVID-19 donors enrolled in the Molecular and Epidemiological Study of Suspected Infection protocol (MESSI), the MESSI clinical support team, the Duke Human Vaccine Institute (DHVI) Clinical Accessioning Unit Core and the DHVI Immunology and Virology Quality Assessment Core for sample procurement, processing and biobanking. We thank J. Gilmore, S. Slater, K. Hwang, A.Y. Abuahmad, T. Evangelous, C.Jones, K. Anasti, M. Berry, S. Venkatayogi, P.Rawls, L. Smith, J. Hwang, B. Bryan, J. Li, H. Chen, N. De Naeyer, the DHVI Flow Cytometry Facility and the Duke BMI CORE facility for technical assistance. We thank Drs. M. Gagne and D. C. Douek at the National Institutes of Health (NIH) for assistant with subgenomic RNA assays. We thank K. Soderberg, E. Donahue, A. Karlsson, A. Newman and W. Edwards for program management. COVID-19 donor sample processing, flow cytometric sorting, and replication-competent virus neutralization assays were performed in the Duke Regional Biocontainment Laboratory, which received partial support for construction from the NIH, NIAID (UC6-AI058607). This work was supported by NIH, NIAID, DAIDS grant AI142596 (B.F.H.); the State of NC funded by the Coronavirus Aid, Relief, and Economic Security Act (CARES Act) (B.F.H.); the Ting Tsung & Wei Fong Chao Foundation (B.F.H.).; NIH supplement to R01 AI145687 (P.A.); NIH grants R01AI157155 and U54CA260543 (R.S.B.); NIH F32 AI152296 (D.R.M), previous

grant NIH NIAID T32 AI007151 (D.R.M), Burroughs Wellcome Fund Postdoctoral Enrichment Program (D.R.M.), NIH NIAID U19AI142596 grant (B.F.H.); NIH R01 AI146779 and a MassCPR grant (A.G.S.); training grants: NIGMS T32 GM007753 (B.M.H. and T.M.C); T32 AI007245 (J.F.); and a cooperative agreement with DOD/DARPA (HR0011-17-2-0069; G.D.S). Cryo-EM data were collected at the National Center for Cryo-EM Access and Training and the Simons Electron Microscopy Center located at the New York Structural Biology Center, supported by the NIH Common Fund Transformative High Resolution Cryo-EM program (U24 GM129539) and by grants from the Simons Foundation (SF349247) and NY State. We thank E. Eng, C. Hernandez and D.Bobe for assistance with cryo-EM experiments. We thank M. DeLong, C. Kneifel, M. Newton, V. Orlikowski, T. Milledge, and D. Lane from the Duke Office of Information Technology and Research Computing, and Duke Research Computing (http://rc.duke.edu; NIH 1S10OD018164-01). We thank L. Pessaint, A. Cook, A.Dodson, K. Steingrebe and B. Bart at BIOQUAL for assistance with macaque studies.

AUTHOR CONTRIBUTIONS

D.L., D.R.M., A.S., X.L., S.M.A., K.C., L.V.T., T.D.S., R.P., V.G., M.D., M.B., T.V.H., T.H.O., E.L., A.F., F.C., G.E.H., A.S., K.T., C.J., L.G.P., C.M., A.M., E.S., D.W.C., K.W.B., M.M., B.M.N., and L.L.S. performed experiments and analyzed data. R.J.E., K.Mansouri, K.Manne, S.G., K.J., M.K., V.S. and P.A. performed structure experiments and analysis. W.R. and Y.W. provided statistical analyses. K.W., C.T.D., T.N.D., G.D.S., D.C.M., C.W.W., E.P., M.A.M., I.N.M., R.S., H.A., M.G.L., and R.S.B. oversaw studies. A.G.S., J.F., B.M.H, T.M.C., I.T., T.Z., P.D.K., J.M. and B.G. provided key reagents. K.O.S. and B.F.H. conceived, designed and supervised the study, and evaluated all data. D.L., R.J.E., P.A., K.O.S., and B.F.H. wrote the paper. All authors reviewed and approved the manuscript.

DECLARATION OF INTERESTS

B.F.H., G.D.S. K.O.S., R.P., D.L., P.A. and X.L. have applied for patents concerning SARS-CoV-2 Abs that are related to this work. All other authors declare no conflict of interest.

FIGURE LEGENDS

Figure 1. SARS-CoV-2 receptor-binding domain (RBD) and N-terminal domain (NTD) Abs mediate enhancement of infection.

(A-B) Timeline of blood sampling, plasmablasts and/or antigen-specific memory B cells (MBC) sorting, and Ab isolation from convalescent (A) SARS-CoV-2 and (B) SARS-CoV donors.

(C) Summary of number and specificity of Abs isolated from each donor.

(D-E) *In vitro* neutralization curves for NTD infection-enhancing Abs against (D) pseudotyped SARS-CoV-2 D614G in 293T-hACE2 cells, and (E) replication-competent nano-luciferase (nLuc) SARS-CoV-2 in Vero cells.

(F-J) FcγR-dependent pseudotyped SARS-CoV-2 infection-enhancement when RBD Abs or mock medium control was added to (F) parental TZM-bl cells, and TZM-bl cells stably expressing human FcγR receptors (G) FcγRI, (H) FcγRIIa, (I) FcγRIIb or (J) FcγRIII.

(**K-L**) The effect of RBD Ab fragment antigen-binding regions (Fabs) on pseudotyped SARS-CoV-2 D614G infection was tested in (K) FcγRI-expressing TZM-bl cells and (L) FcγRIIb-expressing TZM-bl cells. Data are represented as mean±SEM. Three or four independent experiments were performed and representative data are shown.

Figure 2. Structural and phenotypic characterization of infection-enhancing and non-infection-enhancing RBD and NTD Abs.

(A) Summary of Ab epitope, binding, and neutralizing or infection-enhancing activity in ACE2-positive/FcγR-negative cells or ACE2-negative/FcγR-positive cells. Ab functions are color-coded based on the key shown at the right. MN titer, micro-neutralization titer; ND, not determined.

(B-E) 3D reconstruction of negative stain electron microscopy images of stabilized SARS-CoV-2 S ectodomain trimers (S-2P; gray) bound to the Fabs (various colors) of (B,D) infection-enhancing or (C,E) non-infection-enhancing RBD or NTD antibodies.

Figure 3. Simultaneous binding of infection-enhancing and non-infection enhancing Abs to individual S trimers.

(A) Cross-blocking activity of RBD and NTD neutralizing Abs tested by surface plasmon resonance (SPR). S-2P was captured by one Ab (Y-axis) followed by binding by the second Ab (X-axis).

(B) 3D reconstruction of simultaneous recognition of SARS-CoV-2 S-2P by two RBD Abs DH1041+DH1047, or DH1043+DH1047.

(C) Cross-blocking activity of neutralizing Abs and infection-enhancing NTD Abs tested by SPR and shown as in (A).

(D-F) 3D reconstruction of SARS-CoV-2 S-2P simultaneously bound (D) NTD Abs DH1053 and DH1050.1, (E) RBD infection-enhancing Ab and a NTD non-infection-enhancing Ab, or (F) triple-Ab combinations of RBD Ab DH1043, RBD Ab DH1047, and either NTD Ab DH1051 (left) or DH1050.1 (right).

(G-H) RBD Ab neutralization of SARS-CoV-2 D614G pseudovirus infection of 293T/ACE2 cells in the presence of 1:132 or 1:1,325 ratios of excess infection-enhancing NTD Ab DH1052.

Figure 4. Cryo-electron microscopy of neutralizing and non-neutralizing Abs in complex with SARS-CoV-2 Spike ectodomain. Structures of SARS-CoV-2 S protein in complex with RBD Abs (**A)** DH1041 (red), (**B)** DH1043 (pink), (**C)** DH1047 (magenta), (**D)** neutralizing NTD Ab DH1050.1 (blue), and (**E)** infection-enhancing NTD Ab DH1052 (green). Each Ab is bound to S-2P shown in gray with its RBM colored purple blue. (Right) Zoomed-in views of the Ab interactions with S-2P trimers. The Ab complementarity determining (CDR) loops are colored: HCDR1 yellow, HCDR2 limon, HCDR3 cyan, LCDR1 orange, LCDR2 wheat and LCDR3 light blue. See also Supplemental Data 1.

Figure 5. NTD Ab DH1052 does not always enhance SARS-CoV-2 replication or disease *in vivo*.

(A-F) DH1052 passive immunization and murine SARS-CoV-2 challenge (**A**) study design, (**B**) body weight, (**C**) survival, (**D**) Hemorrhagic scores, (**E**) lung viral titers, and (**F**) SARS-CoV-2 envelope (E) and nucleocapsid (N) gene subgenomic RNA (sgRNA).

(G-Q) Reduction of SARS-CoV-2 replication and disease in cynomolgus macaques by prophylactic administration of an NTD neutralizing Ab DH1050.1 or an NTD *in vitro* infection-enhancing Ab DH1052.

(G) DH1050.1 and DH1052 prophylaxis cynomolgus macaque (n=5 per group) study design. CH65 was used as a negative control Ab.

(H-I) Serum human IgG concentrations at (**H**) Day -5 and (**I**) Day 2.

(J-K) Day 2 serum neutralization titers shown as the reciprocal serum dilution that inhibits 50% (ID_{50}) of (**J**) pseudotyped SARS-CoV-2 replication in 293T/ACE2 cells or (**K**) SARS-CoV-2 replication in Vero cells.

(L-M) Lung histopathology four days post infection. Lung sections were scored for (**L**) inflammation by hematoxylin and eosin (H&E) staining, and for (**M**) the presence of SARS-CoV-2 nucleocapsid by immunohistochemistry (IHC) staining.

(N-Q) Viral load quantified as SARS-CoV-2 E gene sgRNA and N gene sgRNA in (N-O) bronchoalveolar lavage (BAL) or (P-Q) nasal swab fluid on Day 2 and Day 4 post challenge. LOD, limit of detection. Statistical significance in all the panels were determined using Wilcoxon rank sum exact test. Horizontal bars are the group mean. Asterisks show the statistical significance between indicated group and CH65 control group: ns, not significant, *P<0.05, **P<0.01, ***P<0.001.

Figure 6. RBD Abs that mediate FcγR-dependent infection-enhancement *in vitro*, protect mice from SARS-CoV-2 or bat WIV1-CoV challenge.

(A-B) Protection of BALB/c mice (n=5 per group) from mouse-adapted SARS-CoV-2 (SARS-CoV-2 2AA MA) by (**A**) prophylactic or (**B**) therapeutic RBD and/or NTD Ab administration. Ab CH65 served as a negative control. Titers of infectious virus in the lung were examined 48h post-infection.

(C) Maximum likelihood tree of Spike amino acid sequences for SARS-related group 2B and group 2C coronaviruses.

(D) Monoclonal RBD, NTD and S2 Ab ELISA binding titer for soluble S protein ectodomains from human and animal coronaviruses. Titers are log area-under-the-curve (AUC).

(E) SARS-CoV and bat WIV1-CoV cross-neutralization titers for cross-reactive RBD and S2 Abs.

(F-G) Protection of HFH4-hACE2-transgenic mice (n=5 per group) from SARS-related bat WIV1-CoV challenge by (**A**) prophylactic or (**B**) therapeutic RBD Ab administration. Lung viral titers were examined at 48 post-infection. Statistical significance in all the panels were determined using Wilcoxon rank sum exact test. Horizontal bars are the group mean. Asterisks show the statistical significance between indicated group and CH65 control group: ns, not significant, *P<0.05, **P<0.01.

Figure 7. RBD Abs that mediate FcγR-dependent infection enhancement *in vitro*, protect non-human primates from SARS-CoV-2 challenge.

(A) Cynomolgus macaques (n=5 per group) RBD Ab SARS-CoV-2 challenge study design. DH1041, DH1043, DH1046, DH1047 or an irrelevant CH65 were infused into macaques.

(B-C) Serum human IgG concentrations at Day -5 (**B**) and Day 2 (**C**).

(D-E) Day 2 serum neutralization titers shown as the reciprocal serum dilution that inhibits 50% (ID_{50}) of (**D**) pseudotyped SARS-CoV-2 replication in 293T/ACE2 cells or (**E**) SARS-CoV-2 replication in Vero cells.

(F-G) Lung histopathology for (**F**) inflammation by H&E staining and (**G**) the presence of SARS-CoV-2 nucleocapsid by IHC staining 4 days post-challenge.

(H-K) Viral load quantified as SARS-CoV-2 E gene sgRNA and N gene sgRNA in (H-I) bronchoalveolar lavage (BAL) or (J-K) nasal swab fluid on Day 2 and Day 4 post challenge.

Statistical significance in all the panels were determined using Wilcoxon rank sum exact test. Horizontal bars are the group mean. Asterisks show the statistical significance between indicated group and CH65 control group: ns, not significant, *P<0.05, **P<0.01.

STAR METHODS

KEY RESOURCES TABLE

REAGENT or RESOURCE	SOURCE	IDENTIFIER
Antibodies		
PE-Cy5 Mouse Anti-Human CD3, Clone# HIT3a	BD Biosciences	Cat#555341; RRID: AB_10698936
BV605 Mouse Anti-Human CD14, Clone# M5E2	Biolegend	Cat#301834, RRID: AB_2563798
BV570 Mouse Anti-Human CD16, Clone# 3G8	Biolegend	Cat# 302035, RRID: AB_2632790
APC-Cy7 Mouse Anti-Human CD19, Clone# SJ25C1	BD Biosciences	Cat# 557791, RRID: AB_396873
FITC Mouse Anti-Human IgD, Clone# IA6-2	BD Biosciences	Cat# 555778, RRID: AB_396113
PerCp-Cy5.5 Mouse Anti-Human IgM, Clone# G20-127	BD Biosciences	Cat# 561285, RRID:AB_10611998
PE-CF594, Mouse Anti-Human CD10, Clone# HI10A	BD Biosciences	Cat# 562396, RRID: AB_11154416
PE-Cy5 Mouse Anti-Human CD235a, Clone# GA-R2	BD Biosciences	Cat# 559944, RRID: AB_397387
PE-Cy7 Mouse Anti-Human CD27, Clone# O323	eBioscience	Cat# 25-0279, RRID: AB_1724039
APC-AF700 Mouse Anti-Human CD38, Clone# LS198-4-2	Beckman Coulter	Cat# B23489, RRID: NA
SARS-CoV/SARS-CoV-2 Spike Ab, Clone# D001	Sino Biological	Cat #40150-D001
Anti-influenza virus hemagglutinin human IgG CH65	(Whittle et al., 2011)	NA
Rabbit polyclonal SARS-CoV-2 nucleocapsid Ab	GeneTex	Cat #GTX135357, RRID:AB_2868464
Rat anti-human CD3, Clone# CD3-12	Bio-Rad	Cat #MCA1477, RRID:AB_321245
Rabbit anti-human Iba1 polyclonal Ab	Wako	Cat# 019-19741, RRID: AB_839504

Rabbit anti-human CD68 polyclonal Ab	Sigma-Millipore	Cat# HPA048982, RRID: AB_2680587
Rabbit anti-human CD163, Clone# EPR19518	Abcam	Cat# ab182422, RRID: AB_2753196
Mouse anti-human HLA-DP/DQ/DR, Clone# CR3/43	Dako	Cat# M0775, RRID: AB_2313661
Rabbit anti-human CD11b, Clone# EP1345Y	Abcam	Cat# ab52478, RRID: AB_868788
HRP goat anti-human IgG	SouthernBiotech	Cat #2040-05, RRID:AB_2795644
HRP goat anti-rabbit IgG	Abcam	Cat #ab97080, RRID:AB_10679808
Biotin mouse anti-human IgG Fc, Clone# H2	Southern Biotech	Cat# 9042-08, RRID:AB_2796608
Bacterial and Virus Strains		
SARS-CoV-2 D614G pseudotyped virus	(Korber et al., 2020)	NA
SARS-CoV-2 virus, Isolate USA-WA1/2020	BEI Resources	Cat #NR-52281
SARS-CoV-2 nanoLuc virus	(Hou et al., 2020)	NA
SARS-CoV nanoLuc virus	(Sheahan et al., 2017)	NA
WIV1-CoV nanoLuc virus	(Menachery et al., 2016)	NA
SARS-CoV-2 moues-adapted virus 2AA MA	(Dinnon et al., 2020)	NA
SARS-CoV-2 moues-adapted virus MA10	(Leist et al., 2020a)	NA
Biological Samples		
Plasma, PBMCs, nasal swabs and bronchoalveolar lavage (BAL) from macaques	This paper	NA
Chemicals, Peptides, and Recombinant Proteins		
LIVE/DEAD Fixable Red Dead Cell Stain Kit	Thermo Fisher Scientific	Cat#L34972
SuperScript III Reverse Transcriptase	Invitrogen	Cat #18080085
dNTP Set, PCR Grade	New England Biolabs	Cat # N0447L
UltraPure DNase/RNase-Free Distilled Water	Invitrogen	Cat #10977
GeneLink Random Hexamer Primers	GeneLink	Cat #26-4000-03
AmpliTaq Gold 360 Mastermix	Thermo Fisher Scientific	Cat #4398881
Expi293 media	Invitrogen	Cat #A1435102
Expifectamine	Life Technologies	Cat #A14524
Protein A beads	Pierce	Cat #PI-20334
MfeI-HF	New England Biolabs	R3589L
MluI-HF	New England Biolabs	R3198L
SureBlue Reserve tetramethylbenzidine substrate	KPL	Cat #5120-0081
TaqMan Fast Virus 1-Step Master Mix	ThermoFisher	4444434
QIAsymphony DSP Virus/Pathogen Midi Kit	Qiagen	937055
NucleoSpin Gel and PCR Clean-Up	Takara	740609.5
MEGAscript T7 Transcription Kit	ThermoFisher	AM1334
MEGAclear Transcription Clean-Up Kit	ThermoFisher	AM1908
Luciferase Cell Culture Lysis 5x Reagent	Promega	Cat# E1531
Background Reducing Ab Diluent	**Agilent**	Cat# S3022
PowerVision Poly-HRP anti-Rabbit IgG IHC Detection	Leica	Cat# PV6121

Systems		
Human ACE2 soluble protein	(Edwards et al., 2021)	NA
SARS-CoV-2 Spike S1+S2 ectodomain (ECD)	Sino Biological	Cat #40589-V08B1
SARS-CoV-2 Spike S2 ECD	Sino Biological	Cat #40590-V08B
SARS-CoV-2 Spike RBD from insect cell sf9	Sino Biological	Cat #40592-V08B
SARS-CoV-2 Spike RBD from mammalian cell 293	Sino Biological	Cat #40592-V08H
SARS-CoV Spike Protein DeltaTM	BEI Resources	Cat #NR-722
SARS-CoV WH20 Spike RBD	Sino Biological	Cat #40150-V08B2
SARS-CoV WH20 Spike S1	Sino Biological	Cat #40150-V08B1
MERS-CoV Spike S1+S2	Sino Biological	Cat #40069-V08B
MERS-CoV Spike S1	Sino Biological	Cat #40069-V08B1
MERS-CoV Spike S2	Sino Biological	Cat #40070-V08B
MERS-CoV Spike RBD	Sino Biological	Cat #40071-V08B1
SARS-CoV CL Protease protein	BEI Resources	Cat #30105
SARS-CoV Membrane (M) protein	BEI Resources	Cat #110705
SARS-CoV-2 Spike NTD	(Zhou et al., 2020b)	NA
SARS-CoV Spike RBD	(Hauser et al., 2020)	NA
MERS-CoV Spike RBD	(Hauser et al., 2020)	NA
SARS-CoV-2 Spike-2P	(Edwards et al., 2021)	NA
SARS-CoV-2 Spike-HexaPro	(Edwards et al., 2021)	NA
Critical Commercial Assays		
MILLIPLEX MAP Non-Human Primate Cytokine/Chemokine Panel, 25-analyte multiplex bead array	Millipore	Cat #PRCYT2MAG40K
Bright-Glo Luciferase Assay System	Promega	Cat #2650
Britelite Luminescence Reporter Gene Assay System	PerkinElmer Life Sciences	Cat #6066761
Nano-Glo Luciferase Assay System	Promega	Cat #N1150
Deposited Data		
Structure of SARS-CoV-2 S protein in complex with Receptor Binding Domain Ab DH1041	This paper	PDB 7LAA, EMD-23246
Structure of SARS-CoV-2 S protein in complex with Receptor Binding Domain Ab DH1047	This paper	PDB 7LD1, EMD-23279
Structure of SARS-CoV-2 S protein in complex with N-terminal domain Ab DH1050.1	This paper	PDB 7LCN, EMD-23277
Structure of SARS-CoV-2 S protein in complex with N-terminal domain Ab DH1052	This paper	PDB 7LAB, EMD-23248
SARS-CoV-2 Spike Protein Trimer bound to DH1043 fab	This paper	PDB 7LJR, EMD-23400
Negative stain EM structure of Ab DH1041 Fab in complex with SARS-CoV-2 Hexapro spike	This paper	EMD-22920
Negative stain EM structure of Ab DH1042 Fab in complex with SARS-CoV-2 2P spike	This paper	EMD-22921
Negative stain EM structure of Ab DH1043 Fab in complex with SARS-CoV-2 Hexapro spike	This paper	EMD-22923
Negative stain EM structure of Ab DH1044 Fab in complex with SARS-CoV-2 2P spike	This paper	EMD-22929
Negative stain EM structure of Ab DH1045 Fab in complex with SARS-CoV-2 Hexapro spike	This paper	EMD-22930
Negative stain EM structure of Ab DH1047 Fab in	This paper	EMD-22933

complex with SARS-CoV-2 Hexapro spike		
Negative stain EM structure of Ab DH1048 Fab in complex with SARS-CoV-2 Hexapro spike	This paper	EMD-22936
Negative stain EM structure of Ab DH1049 Fab in complex with SARS-CoV-2 2P spike	This paper	EMD-22942
Negative stain EM structure of Ab DH1050.1 Fab in complex with SARS-CoV-2 Hexapro spike	This paper	EMD-22944
Negative stain EM structure of Ab DH1050.2 Fab in complex with SARS-CoV-2 2P spike	This paper	EMD-22945
Negative stain EM structure of Ab DH1051 Fab in complex with SARS-CoV-2 Hexapro spike	This paper	EMD-22946
Negative stain EM structure of Ab DH1053 Fab in complex with SARS-CoV-2 2P spike in the 1-RBD-up state	This paper	EMD-22947
Negative stain EM structure of Ab DH1053 Fab in complex with SARS-CoV-2 2P spike in the 3-RBD-down state	This paper	EMD-22948
Negative stain EM structure of Ab DH1054 Fab in complex with SARS-CoV-2 2P spike	This paper	EMD-22951
Negative stain EM structure of Ab DH1055 Fab in complex with SARS-CoV-2 2P spike	This paper	EMD-22952
Negative stain EM structure of Ab DH1056 Fab in complex with SARS-CoV-2 2P spike	This paper	EMD-22953
Negative stain EM structure of Ab Fabs DH1043 and DH1051 in complex with SARS-CoV-2 2P spike	This paper	EMD-22955
Negative stain EM structure of Ab Fabs DH1041 and DH1051 in complex with SARS-CoV-2 2P spike	This paper	EMD-22956
Negative stain EM structure of Ab Fabs DH1043 and DH1047 in complex with SARS-CoV-2 2P spike	This paper	EMD-22957
Negative stain EM structure of Ab Fabs DH1047 and DH1051 in complex with SARS-CoV-2 2P spike	This paper	EMD-22958
Negative stain EM structure of Ab Fabs DH1045 and DH1050.1 in complex with SARS-CoV-2 2P spike	This paper	EMD-22969
Negative stain EM structure of Ab Fabs DH1043 and DH1050.1 in complex with SARS-CoV-2 2P spike	This paper	EMD-22970
Negative stain EM structure of Ab Fabs DH1041 and DH1047 in complex with SARS-CoV-2 2P spike	This paper	EMD-22971
Negative stain EM structure of Ab Fabs DH1050.1 and DH1053 in complex with SARS-CoV-2 2P spike	This paper	EMD-22984
Negative stain EM structure of Ab Fabs DH1043, DH1047 and DH1050.1 in complex with SARS-CoV-2 2P spike	This paper	EMD-22985
Negative stain EM structure of Ab Fabs DH1043, DH1047 and DH1051 in complex with SARS-CoV-2 2P spike	This paper	EMD-22986
Experimental Models: Cell Lines		
TZM-bl	NIH, ARRRP	Cat #8129
TZM-bl expressing FcγRI	(Perez et al., 2009)	NA
TZM-bl expressing FcγRIIa	(Perez et al., 2009)	NA
TZM-bl expressing FcγRIIb	(Perez et al., 2009)	NA
TZM-bl expressing FcγRIII	(Perez et al., 2009)	NA
Expi 293i	Invitrogen	Cat #14527
293T/ACE2	(Korber et al., 2020)	NA

Vero E6	ATCC	Cat# CRL-1586
Experimental Models: Organisms/Strains		
BALB/c mouse	Envigo	NA
HFH4-hACE2 transgenic mice	(Menachery et al., 2016)	NA
Cynomolgus macaques	BioQUAL	NA
Oligonucleotides		
VH1 Leader-A 5'- ATGGACTGGACCTGGAGGAT -3' (PCRa primer)	Thermo Fisher Scientific	NA
VH1 Leader-A 5'- ATGGACTGGACCTGGAGCAT -3' (PCRa primer)	Thermo Fisher Scientific	NA
VH1 Leader-A 5'- ATGGACTGGACCTGGAGAAT -3' (PCRa primer)	Thermo Fisher Scientific	NA
VH1 Leader-A 5'- GGTTCCTCTTTGTGGTGGC -3' (PCRa primer)	Thermo Fisher Scientific	NA
VH1 Leader-A 5'- ATGGACTGGACCTGGAGGGT -3' (PCRa primer)	Thermo Fisher Scientific	NA
VH1 Leader-A 5'- ATGGACTGGATTTGGAGGAT -3' (PCRa primer)	Thermo Fisher Scientific	NA
VH1 Leader-A 5'- AGGTTCCTCTTTGTGGTGGCAG -3' (PCRa primer)	Thermo Fisher Scientific	NA
VH1 Leader-A 5'- ATGGACATACTTTGTTCCACGCTC -3' (PCRa primer)	Thermo Fisher Scientific	NA
VH1 Leader-A 5'- ATGGACACACTTTGCTCCACGCT -3' (PCRa primer)	Thermo Fisher Scientific	NA
VH1 Leader-A 5'- ATGGACACACTTTGCTACACACTC -3' (PCRa primer)	Thermo Fisher Scientific	NA
VH1 Leader-A 5'- CCGACGGGGAATTCTCACAG -3' (PCRa primer)	Thermo Fisher Scientific	NA
VH1 Leader-A 5'- CTGTTATCCTTTGGGTGTCTGCAC -3' (PCRa primer)	Thermo Fisher Scientific	NA
VH1 Leader-A 5'- GGTGGCATTGGAGGGAATGTT -3' (PCRa primer)	Thermo Fisher Scientific	NA
VH1 Leader-A 5'- CGAYGACCACGTTCCCATCT -3' (PCRa primer)	Thermo Fisher Scientific	NA
VH1 Leader-A 5'- TAGTCCTTGACCAGGCAGC -3' (PCRa primer)	Thermo Fisher Scientific	NA
VH1 Leader-A 5'- TAAAAGGTGTCCAGTGT -3' (PCRa primer)	Thermo Fisher Scientific	NA
VH1 Leader-A 5'- TAAGAGGTGTCCAGTGT -3' (PCRa primer)	Thermo Fisher Scientific	NA
VH1 Leader-A 5'- TAGAAGGTGTCCAGTGT -3' (PCRa primer)	Thermo Fisher Scientific	NA
VH1 Leader-A 5'- TACAAGGTGTCCAGTGT -3' (PCRa primer)	Thermo Fisher Scientific	NA
VH1 Leader-A 5'- TTAAAGCTGTCCAGTGT -3' (PCRa primer)	Thermo Fisher Scientific	NA
VH1 Leader-A 5'- ATGAAACATCTGTGGTTCTT -3' (PCRa primer)	Thermo Fisher Scientific	NA

VH1 Leader-A 5'- TTCTCCAAGGAGTCTGT -3' (PCRa primer)	Thermo Fisher Scientific	NA
VH1 Leader-A 5'- GCTATTTTTAAAGGTGTCCAGTGT -3' (PCRa primer)	Thermo Fisher Scientific	NA
VH1 Leader-A 5'- ATGAAACACCTGTGGTTCTTCC -3' (PCRa primer)	Thermo Fisher Scientific	NA
VH1 Leader-A 5'- ATGAAACACCTGTGGTTCTT -3' (PCRa primer)	Thermo Fisher Scientific	NA
VH1 Leader-A 5'- ATGAAGCACCTGTGGTTCTT -3' (PCRa primer)	Thermo Fisher Scientific	NA
VH1 Leader-A 5'- CCTCCACAGTGAGAGTCTG -3' (PCRa primer)	Thermo Fisher Scientific	NA
VH1 Leader-A 5'- ATGTCTGTCTCCTTCCTCATC -3' (PCRa primer)	Thermo Fisher Scientific	NA
VH1 Leader-A 5'- GGCAGCAGCAACAGGTGCCCA -3' (PCRa primer)	Thermo Fisher Scientific	NA
VH1 Leader-A 5'- GCTCAGCTCCTGGGGCT -3' (PCRa primer)	Thermo Fisher Scientific	NA
VH1 Leader-A 5'- GGAARCCCCAGCDCAGC -3' (PCRa primer)	Thermo Fisher Scientific	NA
VH1 Leader-A 5'- CTSTTSCTYTGGATCTCTG -3' (PCRa primer)	Thermo Fisher Scientific	NA
VH1 Leader-A 5'- CTSCTGCTCTGGGYTCC -3' (PCRa primer)	Thermo Fisher Scientific	NA
VH1 Leader-A 5'- GAGGCAGTTCCAGATTTCAA -3' (PCRa primer)	Thermo Fisher Scientific	NA
VH1 Leader-A 5'- CCTGGGCCCAGTCTGTG -3' (PCRa primer)	Thermo Fisher Scientific	NA
VH1 Leader-A 5'- CTCCTCASYCTCCTCACT -3' (PCRa primer)	Thermo Fisher Scientific	NA
VH1 Leader-A 5'- GGCCTCCTATGWGCTGAC -3' (PCRa primer)	Thermo Fisher Scientific	NA
VH1 Leader-A 5'- GTTCTGTGGTTTCTTCTGAGCTG -3' (PCRa primer)	Thermo Fisher Scientific	NA
VH1 Leader-A 5'- ACAGGGTCTCTCTCCCAG -3' (PCRa primer)	Thermo Fisher Scientific	NA
VH1 Leader-A 5'- ACAGGTCTCTGTGCTCTGC -3' (PCRa primer)	Thermo Fisher Scientific	NA
VH1 Leader-A 5'- CCCTCTCSCAGSCTGTG -3' (PCRa primer)	Thermo Fisher Scientific	NA
VH1 Leader-A 5'- TCTTGGGCCAATTTTATGC -3' (PCRa primer)	Thermo Fisher Scientific	NA
VH1 Leader-A 5'- ATTCYCAGRCTGTGGTGAC -3' (PCRa primer)	Thermo Fisher Scientific	NA
VH1 Leader-A 5'- CAGTGGTCCAGGCAGGG -3' (PCRa primer)	Thermo Fisher Scientific	NA
VH1 Leader-A 5'- AGGCCACTGTCACAGCT -3' (PCRa primer)	Thermo Fisher Scientific	NA
VH1-Int tag 5'- CTGGGTTCCAGGTTCCACTGGTGACCAGGTGCAGCTGGTRCAGTCTGGG -3' (PCRb primer)	Thermo Fisher Scientific	NA
VH2-Int tag 5'- CTGGGTTCCAGGTTCCACTGGTGACCAGRGCAC	Thermo Fisher Scientific	NA

CTTGARGGAGTCTGGTCC -3' (PCRb primer)		
VH3-Int tag 5'-CTGGGTTCCAGGTTCCACTGGTGACGAGGTKCAGCTGGTGGAGTCTGGG -3' (PCRb primer)	Thermo Fisher Scientific	NA
VH4-Int tag 5'-CTGGGTTCCAGGTTCCACTGGTGACCAGGTGCAGCTGCAGGAGTCGG -3' (PCRb primer)	Thermo Fisher Scientific	NA
VH5-Int tag 5'-CTGGGTTCCAGGTTCCACTGGTGACGARGTGCAGCTGGTGCAGTCTGGAG -3' (PCRb primer)	Thermo Fisher Scientific	NA
VH6-Int tag 5'-CTGGGTTCCAGGTTCCACTGGTGACCAGGTACAGCTGCAGCAGTCAGGTCC -3' (PCRb primer)	Thermo Fisher Scientific	NA
IgG-int 5'-GGGCCGCTGTGCCCCCAGAGGTGCTCYTGGA -3' (PCRb primer)	Thermo Fisher Scientific	NA
IgM-int 5'-GGGCCGCTGTGCCCCCAGAGGTGGAATTCTCACAGGAGACGAGG -3' (PCRb primer)	Thermo Fisher Scientific	NA
IgD-int 5'-GGGCCGCTGTGCCCCCAGAGGTGTGTCTGCACCCTGATATGATGG -3' (PCRb primer)	Thermo Fisher Scientific	NA
IgA1-int 5'-GGGCCGCTGTGCCCCCAGAGGTGCTGGTGCTGCAGAGGCTCAG -3' (PCRb primer)	Thermo Fisher Scientific	NA
IgA2-int 5'-GGGCCGCTGTGCCCCCAGAGGTGCTGGTGCTGTCGAGGCTCAG -3' (PCRb primer)	Thermo Fisher Scientific	NA
VK1-Int tag 5'-CTGGGTTCCAGGTTCCACTGGTGACGACATCCAGWTGACCCAGTCTC -3' (PCRb primer)	Thermo Fisher Scientific	NA
VK2-Int tag 5'-CTGGGTTCCAGGTTCCACTGGTGACGATATTGTGATGACCCAGWCTCCAC -3' (PCRb primer)	Thermo Fisher Scientific	NA
VK3-Int tag 5'-CTGGGTTCCAGGTTCCACTGGTGACGAAATTGTGTTGACRCAGTCTCCA -3' (PCRb primer)	Thermo Fisher Scientific	NA
VK4-Int tag 5'-CTGGGTTCCAGGTTCCACTGGTGACGACATCGTGATGACCCAGTCTC -3' (PCRb primer)	Thermo Fisher Scientific	NA
VK5-Int tag 5'-CTGGGTTCCAGGTTCCACTGGTGACGAAACGACACTCACGCAGTCTC -3' (PCRb primer)	Thermo Fisher Scientific	NA
VK6-Int tag 5'-CTGGGTTCCAGGTTCCACTGGTGACGAAATTGTGCTGACWCAGTCTCCA -3' (PCRb primer)	Thermo Fisher Scientific	NA
VK7-Int tag 5'-CTGGGTTCCAGGTTCCACTGGTGACGACATTGTGCTGACCCAGTCT -3' (PCRb primer)	Thermo Fisher Scientific	NA
CK-int 5'- GGGAAGATGAAGACAGATGGT -3' (PCRb primer)	Thermo Fisher Scientific	NA
VL1-Int tag 5'-CTGGGTTCCAGGTTCCACTGGTGACCAGTCTGTGYTGACKCAGCC -3' (PCRb primer)	Thermo Fisher Scientific	NA

VL2-Int tag 5'-CTGGGTTCCAGGTTCCACTGGTGACCAGTCTGCCCTGACTCAGCC -3' (PCRb primer)	Thermo Fisher Scientific	NA
VL3-Int tag 5'-CTGGGTTCCAGGTTCCACTGGTGACTCYTATGAGCTGACWCAGCCAC -3' (PCRb primer)	Thermo Fisher Scientific	NA
VL3l-Int tag 5'-CTGGGTTCCAGGTTCCACTGGTGACTCTTCTGAGCTGACTCAGGACCC -3' (PCRb primer)	Thermo Fisher Scientific	NA
VL4ab-Int tag 5'-CTGGGTTCCAGGTTCCACTGGTGACCAGCYTGTGCTGACTCAATC -3' (PCRb primer)	Thermo Fisher Scientific	NA
VL4c-Int tag 5'-CTGGGTTCCAGGTTCCACTGGTGACCTGCCTGTGCTGACTCAGC -3' (PCRb primer)	Thermo Fisher Scientific	NA
VL5,9-Int tag 5'-CTGGGTTCCAGGTTCCACTGGTGACCAGSCTGTGCTGACTCAGCC -3' (PCRb primer)	Thermo Fisher Scientific	NA
VL6-Int tag 5'-CTGGGTTCCAGGTTCCACTGGTGACAATTTTATGCTGACTCAGCCCCACT -3' (PCRb primer)	Thermo Fisher Scientific	NA
VL7,8-Int tag 5'-CTGGGTTCCAGGTTCCACTGGTGACCAGRCTGTGGTGACYCAGGAG -3' (PCRb primer)	Thermo Fisher Scientific	NA
VL10-Int tag 5'-CTGGGTTCCAGGTTCCACTGGTGACCAGGCAGGGCWGACTCAG -3' (PCRb primer)	Thermo Fisher Scientific	NA
CL-int 5'- GGGYGGGAACAGAGTGACC -3' (PCRb primer)	Thermo Fisher Scientific	NA
VH_Tag fwd seq 5'-CTGGGTTCCAGGTTCCACTGGTGAC -3' (Sequencing primer)	Thermo Fisher Scientific	NA
CK_int 5'- GGGAAGATGAAGACAGATGGT -3' (Sequencing primer)	Thermo Fisher Scientific	NA
CL_int 5'- GGGYGGGAACAGAGTGACC -3' (Sequencing primer)	Thermo Fisher Scientific	NA
HV13221H_R474 5'- GCTGTGCCCCCAGAGGTG -3' (Sequencing primer)	Thermo Fisher Scientific	NA
VH1 Leader-A 5'- ATGGACTGGACCTGGAGGAT -3' (PCRa primer)	Thermo Fisher Scientific	NA
VH1 Leader-A 5'- ATGGACTGGACCTGGAGCAT -3' (PCRa primer)	Thermo Fisher Scientific	NA
VH1 Leader-A 5'- ATGGACTGGACCTGGAGAAT -3' (PCRa primer)	Thermo Fisher Scientific	NA
VH1 Leader-A 5'- GGTTCCTCTTTGTGGTGGC -3' (PCRa primer)	Thermo Fisher Scientific	NA
VH1 Leader-A 5'- ATGGACTGGACCTGGAGGGT -3' (PCRa primer)	Thermo Fisher Scientific	NA
VH1 Leader-A 5'- ATGGACTGGATTTGGAGGAT -3' (PCRa primer)	Thermo Fisher Scientific	NA
VH1 Leader-A 5'- AGGTTCCTCTTTGTGGTGGCAG -3' (PCRa primer)	Thermo Fisher Scientific	NA
VH1 Leader-A 5'-ATGGACATACTTTGTTCCACGCTC -3' (PCRa	Thermo Fisher Scientific	NA

primer)		
VH1 Leader-A 5'-ATGGACACACTTTGCTCCACGCT -3' (PCRa primer)	Thermo Fisher Scientific	NA
VH1 Leader-A 5'-ATGGACACACTTTGCTACACACTC -3' (PCRa primer)	Thermo Fisher Scientific	NA
VH1 Leader-A 5'- CCGACGGGGAATTCTCACAG -3' (PCRa primer)	Thermo Fisher Scientific	NA
VH1 Leader-A 5'-CTGTTATCCTTTGGGTGTCTGCAC -3' (PCRa primer)	Thermo Fisher Scientific	NA
VH1 Leader-A 5'- GGTGGCATTGGAGGGAATGTT -3' (PCRa primer)	Thermo Fisher Scientific	NA
VH1 Leader-A 5'- CGAYGACCACGTTCCCATCT -3' (PCRa primer)	Thermo Fisher Scientific	NA
VH1 Leader-A 5'- TAGTCCTTGACCAGGCAGC -3' (PCRa primer)	Thermo Fisher Scientific	NA
VH1 Leader-A 5'- TAAAAGGTGTCCAGTGT -3' (PCRa primer)	Thermo Fisher Scientific	NA
VH1 Leader-A 5'- TAAGAGGTGTCCAGTGT -3' (PCRa primer)	Thermo Fisher Scientific	NA
VH1 Leader-A 5'- TAGAAGGTGTCCAGTGT -3' (PCRa primer)	Thermo Fisher Scientific	NA
VH1 Leader-A 5'- TACAAGGTGTCCAGTGT -3' (PCRa primer)	Thermo Fisher Scientific	NA
VH1 Leader-A 5'- TTAAAGCTGTCCAGTGT -3' (PCRa primer)	Thermo Fisher Scientific	NA
VH1 Leader-A 5'- ATGAAACATCTGTGGTTCTT -3' (PCRa primer)	Thermo Fisher Scientific	NA
VH1 Leader-A 5'- TTCTCCAAGGAGTCTGT -3' (PCRa primer)	Thermo Fisher Scientific	NA
VH1 Leader-A 5'-GCTATTTTTAAAGGTGTCCAGTGT -3' (PCRa primer)	Thermo Fisher Scientific	NA
VH1 Leader-A 5'- ATGAAACACCTGTGGTTCTTCC -3' (PCRa primer)	Thermo Fisher Scientific	NA
VH1 Leader-A 5'- ATGAAACACCTGTGGTTCTT -3' (PCRa primer)	Thermo Fisher Scientific	NA
VH1 Leader-A 5'- ATGAAGCACCTGTGGTTCTT -3' (PCRa primer)	Thermo Fisher Scientific	NA
VH1 Leader-A 5'- CCTCCACAGTGAGAGTCTG -3' (PCRa primer)	Thermo Fisher Scientific	NA
VH1 Leader-A 5'- ATGTCTGTCTCCTTCCTCATC -3' (PCRa primer)	Thermo Fisher Scientific	NA
VH1 Leader-A 5'- GGCAGCAGCAACAGGTGCCCA -3' (PCRa primer)	Thermo Fisher Scientific	NA
VH1 Leader-A 5'- GCTCAGCTCCTGGGGCT -3' (PCRa primer)	Thermo Fisher Scientific	NA
VH1 Leader-A 5'- GGAARCCCCAGCDCAGC -3' (PCRa primer)	Thermo Fisher Scientific	NA
VH1 Leader-A 5'- CTSTTSCTYTGGATCTCTG -3' (PCRa primer)	Thermo Fisher Scientific	NA
VH1 Leader-A 5'- CTSCTGCTCTGGGYTCC -3'	Thermo Fisher	NA

(PCRa primer)	Scientific	
VH1 Leader-A 5'- GAGGCAGTTCCAGATTTCAA -3' (PCRa primer)	Thermo Fisher Scientific	NA
VH1 Leader-A 5'- CCTGGGCCCAGTCTGTG -3' (PCRa primer)	Thermo Fisher Scientific	NA
VH1 Leader-A 5'- CTCCTCASYCTCCTCACT -3' (PCRa primer)	Thermo Fisher Scientific	NA
VH1 Leader-A 5'- GGCCTCCTATGWGCTGAC -3' (PCRa primer)	Thermo Fisher Scientific	NA
VH1 Leader-A 5'- GTTCTGTGGTTTCTTCTGAGCTG -3' (PCRa primer)	Thermo Fisher Scientific	NA
VH1 Leader-A 5'- ACAGGGTCTCTCTCCCAG -3' (PCRa primer)	Thermo Fisher Scientific	NA
VH1 Leader-A 5'- ACAGGTCTCTGTGCTCTGC -3' (PCRa primer)	Thermo Fisher Scientific	NA
VH1 Leader-A 5'- CCCTCTCSCAGSCTGTG -3' (PCRa primer)	Thermo Fisher Scientific	NA
VH1 Leader-A 5'- TCTTGGGCCAATTTTATGC -3' (PCRa primer)	Thermo Fisher Scientific	NA
VH1 Leader-A 5'- ATTCYCAGRCTGTGGTGAC -3' (PCRa primer)	Thermo Fisher Scientific	NA
VH1 Leader-A 5'- CAGTGGTCCAGGCAGGG -3' (PCRa primer)	Thermo Fisher Scientific	NA
VH1 Leader-A 5'- AGGCCACTGTCACAGCT -3' (PCRa primer)	Thermo Fisher Scientific	NA
VH1-Int tag 5'- CTGGGTTCCAGGTTCCACTGGTGACCAGGTGCA GCTGGTRCAGTCTGGG -3' (PCRb primer)	Thermo Fisher Scientific	NA
VH2-Int tag 5'- CTGGGTTCCAGGTTCCACTGGTGACCAGRGCAC CTTGARGGAGTCTGGTCC -3' (PCRb primer)	Thermo Fisher Scientific	NA
VH3-Int tag 5'- CTGGGTTCCAGGTTCCACTGGTGACGAGGTKCA GCTGGTGGAGTCTGGG -3' (PCRb primer)	Thermo Fisher Scientific	NA
VH4-Int tag 5'- CTGGGTTCCAGGTTCCACTGGTGACCAGGTGCA GCTGCAGGAGTCGG -3' (PCRb primer)	Thermo Fisher Scientific	NA
VH5-Int tag 5'- CTGGGTTCCAGGTTCCACTGGTGACGARGTGCA GCTGGTGCAGTCTGGAG -3' (PCRb primer)	Thermo Fisher Scientific	NA
VH6-Int tag 5'- CTGGGTTCCAGGTTCCACTGGTGACCAGGTACA GCTGCAGCAGTCAGGTCC -3' (PCRb primer)	Thermo Fisher Scientific	NA
IgG-int 5'- GGGCCGCTGTGCCCCCAGAGGTGCTCYTGGA -3' (PCRb primer)	Thermo Fisher Scientific	NA
IgM-int 5'- GGGCCGCTGTGCCCCCAGAGGTGGAATTCTCAC AGGAGACGAGG -3' (PCRb primer)	Thermo Fisher Scientific	NA
IgD-int 5'- GGGCCGCTGTGCCCCCAGAGGTGTGTCTGCACC CTGATATGATGG -3' (PCRb primer)	Thermo Fisher Scientific	NA
IgA1-int 5'- GGGCCGCTGTGCCCCCAGAGGTGCTGGTGCTGC	Thermo Fisher Scientific	NA

AGAGGCTCAG -3' (PCRb primer)		
IgA2-int 5'-GGGCCGCTGTGCCCCCAGAGGTGCTGGTGCTGTCGAGGCTCAG -3' (PCRb primer)	Thermo Fisher Scientific	NA
VK1-Int tag 5'-CTGGGTTCCAGGTTCCACTGGTGACGACATCCAGWTGACCCAGTCTC -3' (PCRb primer)	Thermo Fisher Scientific	NA
VK2-Int tag 5'-CTGGGTTCCAGGTTCCACTGGTGACGATATTGTGATGACCCAGWCTCCAC -3' (PCRb primer)	Thermo Fisher Scientific	NA
VK3-Int tag 5'-CTGGGTTCCAGGTTCCACTGGTGACGAAATTGTGTTGACRCAGTCTCCA -3' (PCRb primer)	Thermo Fisher Scientific	NA
VK4-Int tag 5'-CTGGGTTCCAGGTTCCACTGGTGACGACATCGTGATGACCCAGTCTC -3' (PCRb primer)	Thermo Fisher Scientific	NA
VK5-Int tag 5'-CTGGGTTCCAGGTTCCACTGGTGACGAAACGACACTCACGCAGTCTC -3' (PCRb primer)	Thermo Fisher Scientific	NA
VK6-Int tag 5'-CTGGGTTCCAGGTTCCACTGGTGACGAAATTGTGCTGACWCAGTCTCCA -3' (PCRb primer)	Thermo Fisher Scientific	NA
VK7-Int tag 5'-CTGGGTTCCAGGTTCCACTGGTGACGACATTGTGCTGACCCAGTCT -3' (PCRb primer)	Thermo Fisher Scientific	NA
CK-int 5'- GGGAAGATGAAGACAGATGGT -3' (PCRb primer)	Thermo Fisher Scientific	NA
VL1-Int tag 5'-CTGGGTTCCAGGTTCCACTGGTGACCAGTCTGTGYTGACKCAGCC -3' (PCRb primer)	Thermo Fisher Scientific	NA
VL2-Int tag 5'-CTGGGTTCCAGGTTCCACTGGTGACCAGTCTGCCCTGACTCAGCC -3' (PCRb primer)	Thermo Fisher Scientific	NA
VL3-Int tag 5'-CTGGGTTCCAGGTTCCACTGGTGACTCYTATGAGCTGACWCAGCCAC -3' (PCRb primer)	Thermo Fisher Scientific	NA
VL3l-Int tag 5'-CTGGGTTCCAGGTTCCACTGGTGACTCTTCTGAGCTGACTCAGGACCC -3' (PCRb primer)	Thermo Fisher Scientific	NA
VL4ab-Int tag 5'-CTGGGTTCCAGGTTCCACTGGTGACCAGCYTGTGCTGACTCAATC -3' (PCRb primer)	Thermo Fisher Scientific	NA
VL4c-Int tag 5'-CTGGGTTCCAGGTTCCACTGGTGACCTGCCTGTGCTGACTCAGC -3' (PCRb primer)	Thermo Fisher Scientific	NA
VL5,9-Int tag 5'-CTGGGTTCCAGGTTCCACTGGTGACCAGSCTGTGCTGACTCAGCC -3' (PCRb primer)	Thermo Fisher Scientific	NA
VL6-Int tag 5'-CTGGGTTCCAGGTTCCACTGGTGACAATTTTATGCTGACTCAGCCCCACT -3' (PCRb primer)	Thermo Fisher Scientific	NA
VL7,8-Int tag 5'-CTGGGTTCCAGGTTCCACTGGTGACCAGRCTGTGGTGACYCAGGAG -3' (PCRb primer)	Thermo Fisher Scientific	NA

VL10-Int tag 5'-CTGGGTTCCAGGTTCCACTGGTGACCAGGCAGGGCWGACTCAG -3' (PCRb primer)	Thermo Fisher Scientific	NA
CL-int 5'- GGGYGGGAACAGAGTGACC -3' (PCRb primer)	Thermo Fisher Scientific	NA
VH_Tag fwd seq 5'-CTGGGTTCCAGGTTCCACTGGTGAC -3' (Sequencing primer)	Thermo Fisher Scientific	NA
CK_int 5'- GGGAAGATGAAGACAGATGGT -3' (Sequencing primer)	Thermo Fisher Scientific	NA
CL_int 5'- GGGYGGGAACAGAGTGACC -3' (Sequencing primer)	Thermo Fisher Scientific	NA
HV13221H_R474 5'- GCTGTGCCCCCAGAGGTG -3' (Sequencing primer)	Thermo Fisher Scientific	NA
SARS-CoV-2 or WIV1-CoV E gene subgenomic RNA primer/probe: forward primer: 5'-CGATCTCTTGTAGATCTGTTCTC-3'; reverse primer: 5'-ATATTGCAGCAGTACGCACACA-3'; Probe: 5'-FAM-ACACTAGCCATCCTTACTGCGCTTCG-BHQ1-3'.	Taqman	NA
SARS-CoV-2 N gene subgenomic RNA primer/probe: forward primer: 5'-CGATCTCTTGTAGATCTGTTCTC-3'; reverse primer: 5'-GGTGAACCAAGACGCAGTAT-3'; Probe: 5'-FAM-TAACCAGAATGGAGAACGCAGTGGG-BHQ1-3'.	Taqman	NA
WIV1-CoV N gene subgenomic RNA primer/probe: forward primer: 5'-CGATCTCTTGTAGATCTGTTCTC-3'; reverse primer: 5'-TGTGAACCAAGACGCAGTATTAT-3'; Probe: 5'-FAM-TAACCAGAATGGAGGACGCAATGGG-BHQ1-3';	Taqman	NA
SARS-CoV-2 total viral RNA E gene primer/probe: forward primer: 5'-ACAGGTACGTTAATAGTTAATAGCGT-3', reverse primer: 5'-ATATTGCAGCAGTACGCACACA-3'; probe: 5'-6FAM/ACACTAGCCATCCTTACTGCGCTTCG/IABkFQ-3'.	Taqman	NA
Recombinant DNA		
HV1301409_4A (human IgG1_4A heavy chain backbone)	Genscript	NA
pH510049_VRC_LS.v2 (human IgG1_LS heavy chain backbone)	Genscript	NA
HV1301410 (human kappa chain backbone)	Genscript	NA
HV1301414.v2 (human lambda chain backbone)	Genscript	NA
pcDNA3.1-SARS-CoV-2_SgE (for making subgenomic RNA standard RNA)	Genscript	NA
pcDNA3.1-SARS-CoV-2_SgN (for making subgenomic RNA standard RNA)	Genscript	NA

pcDNA3.1-WIV1-CoV_SgN (for making subgenomic RNA standard RNA)	Genscript	NA
Software and Algorithms		
Diva	BD Biosciences	http://www.bdbiosciences.com/us/instruments/clinical/software/flow-cytometry-acquisition/bd-facsdiva-software/m/333333/overview
FlowJo v9.9.4	FlowJo, LLC	https://www.flowjo.com
GraphPad Prism v8.3.1	GraphPad Software Inc	https://www.graphpad.com/scientific-software/prism/
SAS v9.4	SAS Institute	NA
Cloanalyst Program	(Kepler et al., 2014)	NA
Biacore S200 Evaluation software	Cytiva	NA
Coot	(Emsley et al., 2010)	Version 0.8.9.2
Relion	(Scheres, 2012; Scheres, 2016)	Version 3.1
Phenix	(Afonine et al., 2018; Liebschner et al., 2019)	Version 1.17
UCSF Chimera	(Pettersen et al., 2004)	http://www.cgl.ucsf.edu/chimera/
ISOLDE	(Croll, 2018)	Version 1.1
Chimera X	(Goddard et al., 2018)	https://www.rbvi.ucsf.edu/chimerax/
PyMol	The PyMOL Molecular Graphics System (Schrödinger, 2015).	https://www.pymol.org/2/
Leginon system	(Suloway et al., 2005).	NA
cryoSPARC	(Punjani et al., 2017)	https://cryosparc.com
Bio-Plex Manager Software	Bio-Rad	NA
Adobe Illustrator 2020	Adobe	NA
Adobe Photoshop CC 2019	Adobe	NA
Other		

RESOURCE AVAILABILITY

Lead contact

Further information and requests for reagents should be directed and will be fulfilled by the Lead Contact Kevin O. Saunders (kevin.saunders@duke.edu).

Materials availability

Abs and other reagents generated in this study are available from the Lead Contact with a completed Materials Transfer Agreement.

Data and code availability

The data that support the findings of this study are available from the corresponding authors on request. Additional Supplemental Items are available from Mendeley Data at http://dx.doi.org/10.17632/9y6p7shshy.1.

EXPERIMENTAL MODEL AND SUBJECT DETAILS

Human Subjects

Nasopharyngeal swabs and peripheral blood samples were collected from a convalescent COVID-19 donor (MESSI ID #450905) on designated days after reported onset of COVID symptoms. The SARS-CoV donor PBMC were provided by NIH/VRC. Human subject specimens were collected and used with the informed consent of study participants and in compliance with the Duke University Medical Center Institutional Review Board (DUHS IRB Pro00100241).

Symptom data collections

Participant self-reported symptoms were recorded at each time-point for 39 symptom categories (nasal discharge, nasal congestion, sneezing, coughing, shortness of breath, malaise, throat discomfort, fever, headache, shaking chills, loss of smell, loss of taste, excessive sweating, dizziness, pain behind the eyes, itchy/watery eyes, visual blurring, hearing problems, ear pain, confusion, stiff neck, swollen glands, palpitations, chest pain, pain in joints, muscle soreness, fatigue, loss of appetite, abdominal pain, nausea/vomiting, diarrhea, swelling, itchy skin, rash, skin lesions, unusual bleeding, red fingers or toes, red eyes, other: specify). Each symptom was scored on a scale of 0–4, with 0 indicating not present, 1 mild, 2 moderate, 3 severe, and 4 very severe symptoms. Daily symptom count (number of non-zero symptom categories) and symptom severity (sum of all symptom scores) were determined for each survey timepoint. At enrollment, date of symptom onset was determined, and an initial

"historical" symptom survey recorded maximum score for each symptom category between symptom onset and study enrollment.

Non-human primate model

In total, 62 outbred adult male and female cynomolgus macaques (Macaca fascicularis), 2-4 kg body weight, were randomly allocated to groups. The study protocol and all veterinarian procedures were approved by the Bioqual IACUC per a memorandum of understanding with the Duke IACUC, and were performed based on standard operating procedures. Macaques studied were housed and maintained in an Association for Assessment and Accreditation of Laboratory Animal Care-accredited institution in accordance with the principles of the National Institute of Health. All studies were carried out in strict accordance with the recommendations in the Guide for the Care and Use of Laboratory Animals of the National Institutes of Health in BIOQUAL (Rockville, MD). BIOQUAL is fully accredited by AAALAC and through OLAW, Assurance Number A-3086. All physical procedures associated with this work were done under anesthesia to minimize pain and distress in accordance with the recommendations of the Weatherall report, "The use of non-human primates in research." Teklad 5038 Primate Diet was provided once daily by animal size and weight. The diet was supplemented with fresh fruit and vegetables. Fresh water was given ad libitum. All monkeys were maintained in accordance with the Guide for the Care and Use of Laboratory Animals.

Mouse models

Eleven to twelve-month old female immunocompetent BALB/c mice purchased from Envigo (BALB/c AnNHsd, stock# 047) were used for SARS-CoV-2 *in vivo* protection experiments as described previously (Dinnon et al., 2020; Leist et al., 2020a). Ten-week-old *HFH4-hACE2* transgenic mice were bred and maintained at the University of North Carolina at Chapel Hill and used for WIV-1 *in vivo* protection experiments. Mice were housed in groups of five animals per cage and fed standard chow diet. The study was carried out in accordance with the recommendations for care and use of animals by the Office of Laboratory Animal Welfare (OLAW), National Institutes of Health and the Institutional Animal Care. All mouse studies were performed at the University of North Carolina (Animal Welfare Assurance #A3410-01) using protocols (19-168) approved by the UNC Institutional Animal Care and Use Committee (IACUC) and all mouse studies were performed in a BSL3 facility at UNC.

METHOD DETAILS

Expression of Recombinant Viral Proteins

The SARS-CoV-2 ectodomain constructs were produce and purified as describe previously (Wrapp, D.et al. 2020). Plasmids encoding Spike-2P and HexaPro (Hsieh et al., 2020) were transiently transfected in FreeStyle 293 cells (Thermo Fisher) using Turbo293 (SpeedBiosystems). The cultures were collected on Day 6 post transfection. The cells were separated from the medium by centrifugation. Protein were purified from filtered cell supernatants by StrepTactin resin (IBA) and additionally by size exclusive chromatography using Superose 6 10/300 increase column (GE Healthcare) in 2mM Tris pH 8, 200mMnNaCl, 0.02% NaN_3. SARS-CoV-2 NTD was produced as previously described (Zhou et al., 2020b). SARS-CoV RBD and MERS-CoV Spike RBD were cloned into pVRC vector for mammalian expression (FreeStyle 293F or Expi293F suspension cells). The construct contains an HRV 3C-cleavable C-terminal SBP-8xHis tag. Supernatants were harvested 5 days post-transfection and passaged directly over Cobalt-TALON resin (Takara) followed by size exclusion chromatography on Superdex 200 Increase (GE Healthcare) in 1x PBS. Typical yields from FreeStyle 293F cells are approximately 50 mg/liter culture. Affinity tags can be removed using HRV 3C protease (ThermoScientific) and the protein repurified using Cobalt-TALON resin to remove the protease, tag and non-cleaved protein.

Antigen-Specific Single B Cell Sorting

Plasmablasts were sorted by flow cytometry from the SARS-CoV-2 donor on Day 11 and Day 15 post symptom onset. PBMCs were stained with optimal concentrations of the following fluorochrome-Ab conjugates: IgD PE (Clone# IA6-2, BD Biosciences, Catalog# 555779), CD3 PE-Cy5 (Clone# HIT3a, BD Biosciences, Catalog# 555341), CD10 PE-CF594 (Clone# HI10A, BD Biosciences, Catalog# 562396), CD27 PE-Cy7 (Clone# O323, eBioscience, Catalog# 25-0279), CD38 APC-Alexa Fluor (AF) 700 (Clone# LS198-4-2, Beckman Coulter, Catalog# B23489), CD19 APC-Cy7 (Clone# LJ25C1, BD Biosciences, Catalog# 561743), CD16 BV570 (Clone# 3G8, Biolegend, Catalog# 302035), CD14 BV605 (Clone# M5E2, Biolegend, Catalog# 301834), and CD20 BV650 (Clone# 2H7, BD, Catalog# 563780). The cells were then labeled with Fixable Aqua Live/Dead Cell Stain Kit (Invitrogen, Catalog# L34957). On a BD FACSAria II flow cytometer (BD Biosciences), plasmablasts were identified as viable $CD14^-/CD16^-/CD19^+/CD20^{low}/IgD^-/CD27^{high}/CD38^{high}$ cells and sorted as single cells into 96-

well plates containing lysis buffer. Sorted plates were frozen at -80°C in the DHVI Flow Facility under BSL3 precautions in the Duke Regional Biocontainment Laboratory (Durham, NC) until processing.

Antigen-specific memory B cells (MBCs) were isolated by flow cytometric sorting from the SARS-CoV-2 donor on Day 36 post symptom onset, and a donor with SARS-CoV history. PBMCs were stained with IgD FITC (Clone# IA6-2, BD Biosciences, Catalog# 555778), IgM PerCp-Cy5.5 (Clone# G20-127, BD Biosciences, Catalog# 561285), CD10 PE-CF594 (Clone# HI10A, BD Biosciences, Catalog# 562396), CD3 PE-Cy5 (Clone# HIT3a, BD Biosciences, Catalog# 555341), CD235a PE-Cy5 (Clone# GA-R2, BD Biosciences, Catalog# 559944), CD27 PE-Cy7 (Clone# O323, eBioscience, Catalog# 25-0279), CD38 APC-AF700 (Clone# LS198-4-2, Beckman Coulter, Catalog# B23489), CD19 APC-Cy7 (Clone# LJ25C1, BD Biosciences, Catalog# 561743), CD14 BV605 (Clone# M5E2, Biolegend, Catalog# 301834), CD16 BV570 (Clone# 3G8, Biolegend, Catalog# 302035), and fluorescent-labeled SARS-CoV-2 Spike probes (AF647-conjugated Spike-2P, PE-conjugated Spike-2P, AF647-conjugated NTD, AF647-conjugated RBD, VioBright 515-conjugated RBD). The cells were then labeled with Fixable Aqua Live/Dead Cell Stain Kit (Invitrogen, Catalog# L34957). On a BD FACSAria II flow cytometer (BD Biosciences), antigen-specific MBCs were identified as viable $CD3^-/CD14^-/CD16^-/CD235a^-/CD19^+/IgD^-/probe^+$ cells and were sorted as single cells into 96-well plates containing lysis buffer. Collection plates were immediately frozen in a dry ice/ethanol bath, and stored at -80 °C in the DHVI Flow Facility under BSL3 precautions in the Duke Regional Biocontainment Laboratory until processing. Flow cytometric data were analyzed using FlowJo version 10.

PCR Amplification of Human Ab Genes

Ab genes were amplified by RT-PCR from flow cytometry-sorted single B cells using the methods as described previously (Liao et al., 2009; Wrammert et al., 2008) with modification. The PCR-amplified genes were then purified and sequenced with 10 μM forward and reverse primers. Sequences were analyzed by using the human library in Cloanalyst for the VDJ arrangements of the immunoglobulin IGHV, IGKV, and IGLV sequences and mutation frequencies (Kepler et al., 2014). Clonal relatedness of $V_HD_HJ_H$ and V_LJ_L sequences was determined as previously described (Liao et al., 2013).

Expression of Ab Viable Region Genes as Full-Length IgG Recombinant mAbs

Transient transfection of recombinant Abs was performed as previously described (Liao et al., 2009). Briefly, purified PCR products were used for overlapping PCR to generate linear human IgG expression cassettes. The expression cassettes were transfected into 293i cells using ExpiFectamine (Thermo Fisher Scientific, Catalog# A14525). The supernatant samples containing recombinant IgGs were used for IgG quantification and preliminary ELISA binding screening.

The down-selected human Ab genes were then synthesized and cloned (GenScript) in a human IgG1 backbone (HV1301409_4A) with 4A mutations to enhance Ab-dependent cell-mediated cytotoxicity (ADCC) or a human IgG1 backbone (pH510049_VRC_LS.v2) with a LS mutation to extent Ab half-life (Saunders, 2019). Recombinant IgG Abs were then produced in HEK293i suspension cells by transfection with ExpiFectamine and purified using Protein A resin. The purified IgG Abs were run in SDS-PAGE for Coomassie blue staining and western blot for quality control and then used for the downstream experiments.

Ab Binding ELISA

For ELISA binding assays of Coronavirus Spike Abs, the antigen panel included SARS-CoV-2 Spike S1+S2 ectodomain (ECD) (SINO, Catalog # 40589-V08B1), SARS-CoV-2 Spike-2P (Wrapp et al., 2020b), SARS-CoV-2 Spike S2 ECD (SINO, Catalog # 40590-V08B), SARS-CoV-2 Spike RBD from insect cell sf9 (SINO, Catalog # 40592-V08B), SARS-CoV-2 Spike RBD from mammalian cell 293 (SINO, Catalog # 40592- V08H), SARS-CoV-2 Spike NTD-Biotin, SARS-CoV Spike Protein DeltaTM (BEI, Catalog # NR-722), SARS-CoV WH20 Spike RBD (SINO, Catalog # 40150-V08B2), SARS-CoV WH20 Spike S1 (SINO, Catalog #40150-V08B1), SARS-CoV RBD, MERS-CoV Spike S1+S2 (SINO, Catalog # 40069-V08B), MERS-CoV Spike S1 (SINO, Catalog #40069-V08B1), MERS-CoV Spike S2 (SINO, Catalog #40070-V08B), MERS-CoV Spike RBD (SINO, Catalog #40071-V08B1), MERS-CoV Spike RBD. In preliminary ELISA screening of the transient transfection supernatants, we also screened the Abs against SARS-CoV CL Protease protein (BEI, Catalog # 30105) and SARS-CoV Membrane (M) protein (BEI, Catalog # 110705).

For binding ELISA, 384-well ELISA plates were coated with 2 μg/mL of antigens in 0.1 M sodium bicarbonate overnight at 4°C. Plates were washed with PBS + 0.05% Tween 20 and blocked with blocked with assay diluent (PBS containing 4% (w/v) whey protein, 15% Normal Goat Serum, 0.5% Tween-20, and 0.05% Sodium Azide) at room temperature for 1 hour. Purified mAb samples in 3-fold serial dilutions in assay diluent

starting at 100 μg/mL, or un-diluted transfection supernatant were added and incubated for 1 hour, followed by washing with PBS-0.1% Tween 20. HRP-conjugated goat anti-human IgG secondary Ab (SouthernBiotech, catalog# 2040-05) was diluted to 1:10,000 and incubated at room temperature for 1 hour. These plates were washed four times and developed with tetramethylbenzidine substrate (SureBlue Reserve- KPL). The reaction was stopped with 1 M HCl, and optical density at 450 nm (OD_{450}) was determined.

Affinity Measurements

SPR measurements of SARS-CoV-2 Ab Fab binding to Spike-2P or Spike-HexaPro proteins were performed using a Biacore S200 instrument (Cytiva, formerly GE Healthcare, DHVI BIA Core Facility, Durham, NC) in HBS-EP+ 1x running buffer. The Spike proteins were first captured onto a Series S Streptavidin chip to a level of 300-400 RU for Spike-2P and 350-450 resonance units (RU) for Spike-HexaPro. The Ab Fabs were injected at 0.5 to 500 nM over the captured S proteins using the single cycle kinetics injection mode at a flow rate of 50uL/min. Association phase was maintained with either 120 or 240 second injections of each Fab at increasing concentrations followed by a dissociation of 600 seconds after the final injection. After dissociation, the S proteins were regenerated from the streptavidin surface using a 30 second pulse of Glycine pH1.5. Results were analyzed using the Biacore S200 Evaluation software (Cytiva). A blank streptavidin surface along with blank buffer binding were used for double reference subtraction to account for non-specific protein binding and signal drift. Subsequent curve fitting analyses were performed using a 1:1 Langmuir model with a local Rmax for the Fabs with the exception of DH1050.1 Fab which was fit using the heterogeneous ligand model with local Rmax. The reported binding curves are representative of two data sets.

Surface Plasmon Resonance Ab Blocking Assay

RBD and NTD Abs binding to S protein was measured by surface plasmon resonance (BIAcore 3000; Cytiva, formerly GE Healthcare, DHVI BIA Core Facility, Durham, NC) analysis. Ab binding competition and blocking were measured by SPR following immobilization by amine coupling of monoclonal Abs to CM5 sensor chips (BIAcore/Cytiva). Ab competition experiments were performed by mixing S protein and mAb (30 minutes incubation) followed by injection for 5 minutes at 50 μL/min. In separate assays and from analysis of binding to an identical epitope binding ligand, it was determined that S protein at 20 μm and Ab at 200 μm bind to complete

saturation. Ab blocking assays were performed by co-injecting S protein (20 μM) over mAb immobilized surfaces for 3 minutes at 30 μL/min and a test Ab (200 μM) for 3 minutes at 30 μL/min. The dissociation of the Ab sandwich complex with the spike protein was monitored for 10 minutes with buffer flow and then a 24 second injection of Glycine pH2.0 for regeneration. Blank buffer binding was used for subtraction to account for signal drift. Data analyses were performed with BIA-evaluation 4.1 software (BIAcore/Cytiva).

ACE2-blocking assay

For ACE-2 blocking assays, plates were coated as stated above with 2 ug/mL recombinant ACE-2 protein, then washed and blocked with 3% BSA in 1X PBS. While assay plates blocked, purified Abs were diluted as stated above, only in 1% BSA with 0.05% Tween-20. In a separate dilution plate Spike-2P protein was mixed with the Abs at a final concentration equal to the EC50 at which spike binds to ACE-2 protein. The mixture was allowed to incubate at room temperature for 1 hour. Blocked assay plates were then washed and the Ab-spike mixture was added to the assay plates for a period of 1 hour at room temperature. Plates were washed and a polyclonal rabbit serum against the same Spike-2P protein was added for 1 hour, washed and detected with goat anti rabbit-HRP (Abcam cat# ab97080) followed by TMB substrate. The extent to which Abs were able to block the binding spike protein to ACE-2 was determined by comparing the OD of Ab samples at 450 nm to the OD of samples containing spike protein only with no Ab. The following formula was used to calculate percent blocking: blocking% = (100 - (OD sample/OD of spike only)*100).

Negative-stain electron microscopy

For each Fab-spike complex, an aliquot of spike protein at ~1-5 mg/ml concentration that had been flash frozen and stored at -80 °C was thawed in an aluminum block at 37 °C for 5 minutes; then 1-4 μl of spike was mixed with sufficient Fab to give a 9:1 molar ratio of Fab to spike and incubated for 1 hour at 37 °C. The complex was then cross-linked by diluting to a final spike concentration of 0.1 mg/ml into room-temperature buffer containing 150 mM NaCl, 20 mM HEPES pH 7.4, 5% glycerol, and 7.5 mM glutaraldehyde. After 5 minutes cross-linking, excess glutaraldehyde was quenched by adding sufficient 1 M Tris pH 7.4 stock to give a final concentration of 75 mM Tris and incubated for 5 minutes. For negative stain, carbon-coated grids (EMS, CF300-cu-UL) were glow-discharged for 20s at 15 mA, after which a 5-μl drop of quenched sample was incubated on the

grid for 10-15 s, blotted, and then stained with 2% uranyl formate. After air drying grids were imaged with a Philips EM420 electron microscope operated at 120 kV, at 82,000x magnification and images captured with a 2k x 2k CCD camera at a pixel size of 4.02 Å.

Image processing of negative stain images

The RELION 3.0 program was used for all negative stain image processing. Images were imported, CTF-corrected with CTFFIND, and particles were picked using a spike template from previous 2D class averages of spike alone. Extracted particle stacks were subjected to 2-3 rounds of 2D class averaging and selection to discard junk particles and background picks. Cleaned particle stacks were then subjected to 3D classification using a starting model created from a bare spike model, PDB 6vsb, low-pass filtered to 30 Å. Classes that showed clearly-defined Fabs were selected for final refinements followed by automatic filtering and B-factor sharpening with the default Relion post-processing parameters.

Cryo-EM sample preparation, data collection and processing

To prepare Ab-bound complexes of the SARS-CoV-2 2P spike, the spike at a final concentration of 1–2 mg/mL, in a buffer containing 2 mM Tris pH 8.0, 200 mM NaCl and 0.02% NaN3, was incubated with 5-6 fold molar excess of the Ab Fab fragments for 30–60 min. 0.5% final concentration of glycerol was added to the sample right before freezing. 2.5 µL of protein was deposited on a Quantifoil-1.2/1.3 holey carbon grid that had been glow discharged in a PELCO easiGlow™ Glow Discharge Cleaning System for 15s at 15 mA. After a 30 s incubation in >95% humidity and 22 ºC, excess protein was blotted away for 2.5 seconds using a Whatman #1 filter paper before being plunge frozen into liquid ethane using a Leica EM GP2 plunge freezer (Leica Microsystems). Cryo-EM data were collected on a Titan Krios (Thermo Fisher) equipped with a K3 detector (Gatan). Data were acquired using the Leginon system (Suloway et al., 2005). All the datasets were energy filtered through a either a 20eV or 30eV slit. The dose was fractionated over 50 raw frames and collected at 50ms framerate. Individual frames were aligned and dose-weighted (Zheng et al., 2017). CTF estimation, particle picking and all downstream data processing steps were carried out in cryoSparc (Punjani et al., 2017). After two rounds of 2D classifications during which junk particles were discarded, heterogeneous refinement was performed using low pass filtered maps of unliganded spike as inputs. The output maps showed densities of the bound Fabs, which were further classified by

heterogeneous refinement, followed by non-uniform refinement to obtain the final reconstructions that were used for model fitting.

Cryo-EM structure fitting and analysis

Previously published SARS-CoV-2 ectodomain structures of the all 'down' state (PDB ID 6VXX) and single RBD 'up' state (PDB ID 6VYB), and models of 2-RBD-up and 3-RBD-up states derived from these, were used to fit the cryo-EM maps in Chimera (Pettersen et al., 2004). Models of Fabs were generated in SWIS-MODEL and docked into the cryo-EM reconstructions using Chimera. Mutations were made in Coot (Emsley and Cowtan, 2004). Coordinates were fit to the maps using ISOLDE (Croll, 2018) followed by iterative refinement using Phenix (Afonine et al., 2018) real space refinement and subsequent manual coordinate fitting in Coot as needed. Structure and map analysis were performed using PyMol (Schrodinger, 2015), Chimera (Pettersen et al., 2004) and ChimeraX (Goddard et al., 2018).

Live SARS-CoV-2 neutralization assays

The SARS-CoV-2 virus (Isolate USA-WA1/2020, NR-52281) was deposited by the Centers for Disease Control and Prevention and obtained through BEI Resources, NIAID, NIH. SARS-CoV-2 Micro-neutralization (MN) assays were adapted from a previous study (Berry et al., 2004). In short, sera or purified Abs are diluted two-fold and incubated with 100 TCID50 virus for 1 hour. These dilutions are used as the input material for a TCID50. Each batch of MN includes a known neutralizing control Ab (Clone D001; SINO, CAT# 40150-D001). Data are reported as the last concentration at which a test sample protects Vero E6 cells.

SARS-CoV-2 Plaque Reduction Neutralization Test (PRNT) were performed in the Duke Regional Biocontainment Laboratory BSL3 (Durham, NC) as previously described with virus-specific modifications (Berry et al., 2004). Briefly, two-fold dilutions of a test sample (e.g. serum, plasma, purified Ab) were incubated with 50 PFU SARS-CoV-2 virus (Isolate USA-WA1/2020, NR-52281) for 1 hour. The Ab/virus mixture is used to inoculate Vero E6 cells in a standard plaque assay (Coleman and Frieman, 2015; Kint et al., 2015). Briefly, infected cultures are incubated at 37°C, 5% CO2 for 1 hour. At the end of the incubation, 1 mL of a viscous overlay (1:1 2X DMEM and 1.2% methylcellulose) is added to each well. Plates are incubated for 4 days. After fixation, staining and washing, plates are dried and plaques from each dilution of each sample are counted. Data are

reported as the concentration at which 50% of input virus is neutralized. A known neutralizing control Ab is included in each batch run (Clone D001; SINO, CAT# 40150-D001). GraphPad Prism was used to determine IC/EC_{50} values.

SARS-CoV-2 nano-luciferase (nanoLuc), SARS-CoV nanoLuc and WIV1-CoV nanoLuc replication-competent virus neutralization assay were described previously (Hou et al., 2020; Menachery et al., 2016; Sheahan et al., 2017).

Pseudo-typed SARS-CoV-2 neutralization assay and infection-enhancing assays

Neutralization of SARS-CoV-2 Spike-pseudotyped virus was performed by adopting an infection assay described previously (Korber et al., 2020) with lentiviral vectors and infection in either 293T/ACE2.MF (the cell line was kindly provided by Drs. Mike Farzan and Huihui Mu at Scripps). Cells were maintained in DMEM containing 10% FBS and 50 µg/ml gentamicin. An expression plasmid encoding codon-optimized full-length spike of the Wuhan-1 strain (VRC7480), was provided by Drs. Barney Graham and Kizzmekia Corbett at the Vaccine Research Center, National Institutes of Health (USA). The D614G mutation was introduced into VRC7480 by site-directed mutagenesis using the QuikChange Lightning Site-Directed Mutagenesis Kit from Agilent Technologies (Catalog # 210518). The mutation was confirmed by full-length spike gene sequencing. Pseudovirions were produced in HEK 293T/17 cells (ATCC cat. no. CRL-11268) by transfection using Fugene 6 (Promega, Catalog #E2692). Pseudovirions for 293T/ACE2 infection were produced by co-transfection with a lentiviral backbone (pCMV ΔR8.2) and firefly luciferase reporter gene (pHR' CMV Luc) (Naldini et al., 1996). Culture supernatants from transfections were clarified of cells by low-speed centrifugation and filtration (0.45 µm filter) and stored in 1 ml aliquots at -80 °C.

For 293T/ACE2 neutralization assays, a pre-titrated dose of virus was incubated with 8 serial 3-fold or 5-fold dilutions of mAbs in duplicate in a total volume of 150 µl for 1 hr at 37 °C in 96-well flat-bottom poly-L-lysine-coated culture plates (Corning Biocoat). Cells were suspended using TrypLE express enzyme solution (Thermo Fisher Scientific) and immediately added to all wells (10,000 cells in 100 µL of growth medium per well). One set of 8 control wells received cells + virus (virus control) and another set of 8 wells received cells only (background control). After 66-72 hr of incubation, medium was removed by gentle aspiration and 30 µL of Promega 1x lysis

buffer was added to all wells. After a 10-minute incubation at room temperature, 100 µl of Bright-Glo luciferase reagent was added to all wells. After 1-2 minutes, 110 µl of the cell lysate was transferred to a black/white plate (Perkin-Elmer). Luminescence was measured using a PerkinElmer Life Sciences, Model Victor2 luminometer. Neutralization titers are the mAb concentration (IC50/IC80) at which relative luminescence units (RLU) were reduced by 50% and 80% compared to virus control wells after subtraction of background RLUs. Negative neutralization values are indicative of infection-enhancement. Maximum percent inhibition (MPI) is the reduction in RLU at the highest mAb concentration tested.

For the TZM-bl neutralization assays, a pre-titrated dose of virus was incubated with serial 3-fold dilutions of test sample in duplicate in a total volume of 150 ul for 1 hr at 37 °C in 96-well flat-bottom culture plates. Freshly trypsinized cells (10,000 cells in 100 µl of growth medium containing 75 µg/ml DEAE dextran) were added to each well. One set of control wells received cells + virus (virus control) and another set received cells only (background control). After 68-72 hours of incubation, 150 µl of cultured medium was removed from each well, and 100ul of Britelite Luminescence Reporter Gene Assay System (PerkinElmer Life Sciences) were added and plates incubated for 2 min at room temperature. After this period 150 µl of the lysate was transferred to black solid plates (Costar) for measurements of luminescence in a Perking Elmer instrument. Neutralization titers are the serum dilution at which relative luminescence units (RLU) were reduced by 50% and 80% compared to virus control wells after subtraction of background RLUs. MPI is the reduction in RLU at the highest mAb concentration tested. Infection-enhancing assays were performed with the same format but using TZM-bl cell lines stably expressing each of the four human FcγR receptors (Perez et al., 2009). In this assay an increase in RLUs over the virus control signal represents FcR-mediated entry.

Non-human primate protection study

Groups of five cynomolgus macaques (2-4 kg) were given intravenous infusion with Abs at 10 mg/kg body weight on Day -3, relative to infectious virus challenge. For each animal, 10^5 PFU (~10^6 TCID50) SARS-CoV-2 virus (Isolate USA-WA1/2020) were diluted in 4 mL, and were given by 1 mL intranasally and 3 mL intratracheally on Day 0. Plasma and serum samples were collected on Day -5, 0, 2, and 4. Nasal swabs, nasal washes, and bronchoalveolar lavage (BAL) were collected on Day -5, 2, and 4.

Histopathology and Immunohistochemistry (IHC)

Lung specimen from nonhuman primates were fixed in 10% neutral buffered formalin, processed, and blocked in paraffin for histological analysis. All samples were sectioned at 5 µm and stained with hematoxylin-eosin (H&E) for routine histopathology. Sections were examined under light microscopy using an Olympus BX51 microscope and photographs were taken using an Olympus DP73 camera.

Staining for SARS-CoV-2 antigen was achieved on the Bond RX automated system with the Polymer Define Detection System (Leica) used per manufacturer's protocol. Tissue sections were dewaxed with Bond Dewaxing Solution (Leica) at 72□ for 30 min then subsequently rehydrated with graded alcohol washes and 1x Immuno Wash (StatLab). Heat-induced epitope retrieval (HIER) was performed using Epitope Retrieval Solution 1 (Leica), heated to 100oC for 20 minutes. A peroxide block (Leica) was applied for 5 min to quench endogenous peroxidase activity prior to applying the SARS-CoV-2 Ab (1:2000, GeneTex, GTX135357). Abs were diluted in Background Reducing Ab Diluent (Agilent). The tissue was subsequently incubated with an anti-rabbit HRP polymer (Leica) and colorized with 3,3'-Diaminobenzidine (DAB) chromogen for 10 min. Slides were counterstained with hematoxylin. For macrophage staining, Abs for the following markers were used: CD3 (T cell marker; Bio Rad, Catalog # MCA1477; 1:600 dilution), Iba1 (macrophage marker; Wako, Catalog # 019-19741; 1:800 dilution), CD68 (M1 macrophage marker, Sigma-Millipore, Catalog # HPA048982; 1:1000 dilution), CD163 (M2 macrophage marker; Abcam, Catalog # ab182422; 1:500 dilution), HLA-DP/DQ/DR (Catalog # M1 macrophage marker; Dako, Catalog # M0775; 1:100 dilution), CD11b (monocyte/granulocyte marker; Abcam, Catalog # ab52478; 1:1000 dilution).

Samples were evaluated by a board-certified veterinary pathologist in a blinded manner. Sections of the left caudal (Lc), right middle (Rm), and right caudal (Rc) lung were evaluated and scored for the presence of inflammation by H&E staining, and for the presence of SARS-CoV-2 nucleocapsid by IHC staining. The sums of Lc, Rm, and Rc scores in each animal shown in figures.

Luminex assay

For cytokine profiling, 7-fold concentrated cynomolgus macaques BAL samples were measured using a 25-analyte multiplex bead array (Millipore, catalog # PRCYT2MAG40K) including sCD137, Eotaxin, sFasL, FGF-2, Fractalkine, Granzyme A, Granzyme B, IL-1α, IL-2, IL-4, IL-6, IL-16, IL-17A, IL-17E/IL-25, IL-21, IL-22, IL-23, IL-28A, IL-31, IL-33, IP-10, MIP-3α, Perforin, RANTES, TNFβ. Samples were prepared according to the manufacturer's recommended protocol and read using a Flexmap 3D suspension array reader (Luminex Corp.). Data were analyzed using Bio-Plex manager software v6.2 (Bio-Rad).

For human Ab quantification, SARS-CoV-2 Spike-2P protein, A/Solomon Islands/3/2006 hemagglutinin (HA) protein or bovine serum albumen (Sigma) was carbodiimide coupled to MagPlex-C beads (Luminex Corp) according to the bead manufacturer's protocol. Briefly, beads were washed in H_2O then activated by incubation with 5 mg/mL sulfo-N-hydroxysulfosuccinimide and 5 mg/mL 1-ethyl-3-(3-dimethylaminopropyl) carbodiimide hydrochloride (ThermoFisher) for 20 minutes. Activated beads were washed twice in PBS (ThermoFisher) and then vortexed at 1,500 RPM for two hours at room temperature with 25 µg protein per 5.0 x 10^6 beads. Labelled beads were washed in PBS (ThermoFisher), 1% BSA, 0.02% Tween-20, 0.05% Sodium Azide (all Sigma), counted using a hemacytometer and stored at -80°C. NHP sera were diluted 1:200 in assay buffer (PBS, 1% BSA, pH 7.4, Gibco), then 50 µL of diluted sera or monoclonal Ab 3-fold serially diluted in assay buffer (1000-0.45ng/mL) was added to a 96-well plate and mixed with 50 µL assay buffer containing 2500 BSA-conjugated beads (negative control) plus 2500 HA or Spike-conjugated beads. The plate was shaken at 800RPM for 60 minutes at room temperature, washed twice in assay buffer and then 100 µL 4 µg/mL biotin-conjugated mouse anti-human IgG Fc clone H2 (Southern Biotech) in assay buffer was added to every well. The plate was shaken at 800 RPM for 30 minutes at room temperature, washed two times in assay buffer and then 50 µL 4 µg/mL streptavidin-r-phycoerythrin (Invitrogen) in assay buffer was added to every well. The plate was shaken at 800 RPM for 30 minutes at room temperature and washed twice in assay buffer. Beads were resuspended in 150 µL/well assay buffer, shaken at 800 RPM for 15 minutes at room temperature and then analyzed on a BioPlex 200 bead reader (Bio-Rad). Sera antigen-specific Ab concentrations were calculated using Bio-Plex Manager software (Bio-Rad) by extrapolating from the results of the serially-diluted monoclonal Ab. Sera with Abs above the upper limit of quantitation were re-assayed at 1:1000 or 1:5000. The limit of detection (LOD) for this assay is 0.278 µg/mL.

Mouse protection study

Eleven to twelve-month old female immunocompetent BALB/c mice purchased from Envigo (BALB/c AnNHsd, stock# 047) were used for SARS-CoV-2 *in vivo* protection experiments as described previously (Dinnon et al., 2020). Ten-week-old *HFH4-hACE2* transgenic mice were bred and maintained at the University of North Carolina at Chapel Hill and used for WIV-1 *in vivo* protection experiments. Mice were housed in groups of five animals per cage and fed standard chow diet. Virus inoculations were performed under anesthesia (Ketamine and Xylazine) and effort was taken to minimize animal suffering. For evaluating the prophylactic efficacy of mAbs, mice were intraperitoneally treated with 300 μg of each mAb or 150 μg of each mAb in combination 12 hours prior to infection. Mice were infected intranasally with $1X10^5$ PFU of mouse-adapted SARS-CoV-2 2AA MA (Dinnon et al., 2020) or WIV-1. For evaluating the therapeutic efficacy of mAbs, mice were intraperitoneally treated with 300 μg of each mAb or 150 μg of each mAb in combination 12 hours following infection. Forty-eight hours post infection, mice were sacrificed, and lungs were harvested for viral titer as measured by plaque assays and RNA analysis. In another study, fifty-two weeks old female BALB/c mice were i.p. injected with DH1052 (200ug/mice, n=10) or CH65 control Ab (200ug/mice, n=9). After 12 hours, mice were challenged with 1X10^4 PFU of mouse-adapted SARS-CoV-2 MA10 virus (Leist et al., 2020a). Mice were sacrificed at day 4 post infection, and lungs were harvested for viral titer as measured by plaque assays and RNA analysis. The study was carried out in accordance with the recommendations for care and use of animals by the Office of Laboratory Animal Welfare (OLAW), National Institutes of Health and the Institutional Animal Care. All mouse studies were performed at the University of North Carolina (Animal Welfare Assurance #A3410-01) using protocols (19-168) approved by the UNC Institutional Animal Care and Use Committee (IACUC) and all mouse studies were performed in a BSL3 facility at UNC.

Viral RNA Extraction and Quantification

The assay for SARS-CoV-2 quantitative Polymerase Chain Reaction (qPCR) detects total RNA using the WHO primer/probe set E_Sarbeco (Charité/Berlin). A QIAsymphony SP (Qiagen, Hilden, Germany) automated sample preparation platform along with a virus/pathogen DSP midi kit and the *complex800* protocol were used to extract viral RNA from 800 µL of pooled samples. A reverse primer specific to the envelope gene of SARS-CoV-2 (5'-ATA TTG CAG CAG TAC GCA CAC A-3') was annealed to the extracted RNA and then reverse transcribed

into cDNA using SuperScript™ III Reverse Transcriptase (Thermo Fisher Scientific, Waltham, MA) along with RNAse Out (Thermo Fisher Scientific, Waltham, MA). The resulting cDNA was treated with RNase H (Thermo Fisher Scientific, Waltham, MA) and then added to a custom 4x TaqMan™ Gene Expression Master Mix (Thermo Fisher Scientific, Waltham, MA) containing primers and a fluorescently labeled hydrolysis probe specific for the envelope gene of SARS-CoV-2 (forward primer 5'-ACA GGT ACG TTA ATA GTT AAT AGC GT-3', reverse primer 5'-ATA TTG CAG CAG TAC GCA CAC A-3', probe 5'-6FAM/AC ACT AGC C/ZENA TCC TTA CTG CGC TTC G/IABkFQ-3'). The qPCR was carried out on a QuantStudio 3 Real-Time PCR System (Thermo Fisher Scientific, Waltham, MA) using the following thermal cycler parameters: heat to 50°C, hold for 2 min, heat to 95°C, hold for 10 min, then the following parameters are repeated for 50 cycles: heat to 95°C, hold for 15 seconds, cool to 60°C and hold for 1 minute. SARS-CoV-2 RNA copies per reaction were interpolated using quantification cycle data and a serial dilution of a highly characterized custom DNA plasmid containing the SARS-CoV-2 envelope gene sequence. Mean RNA copies per milliliter were then calculated by applying the assay dilution factor (DF=11.7). The limit of detection (LOD) for this assay is approximately 62 RNA copies per milliliter of sample.

Subgenomic mRNA assay

SARS-CoV-2 E gene and N gene subgenomic mRNA (sgRNA) was measured by a one-step RT-qPCR adapted from previously described methods (Wolfel et al., 2020; Yu et al., 2020). To generate standard curves, a SARS-CoV-2 E gene sgRNA sequence, including the 5'UTR leader sequence, transcriptional regulatory sequence (TRS), and the first 228 bp of E gene, was cloned into a pcDNA3.1 plasmid. For generating SARS-CoV-2 N gene sgRNA, the E gene was replaced with the first 227 bp of N gene. The respectively pcDNA3.1 plasmids were linearized, transcribed using MEGAscript T7 Transcription Kit (ThermoFisher, Catalog # AM1334), and purified with MEGAclear Transcription Clean-Up Kit (ThermoFisher, Catalog # AM1908). The purified RNA products were quantified on Nanodrop, serial diluted, and aliquoted as E sgRNA or N sgRNA standards.

RNA extracted from animal samples or standards were then measured in Taqman custom gene expression assays (ThermoFisher Scientific). For these assays we used TaqMan Fast Virus 1-Step Master Mix (ThermoFisher, catalog # 4444432) and custom primers/probes targeting the E gene sgRNA (forward primer: 5' CGATCTCTTGTAGATCTGTTCTCE 3'; reverse primer: 5' ATATTGCAGCAGT ACGCACACA 3'; probe: 5' FAM-ACACTAGCCATCCTTACTGCGCTTCG-BHQ1 3') or the N gene sgRNA (forward primer: 5'

CGATCTCTTGTAGATCTGTTCTC 3'; reverse primer: 5' GGTGAA CCAAGACGCAGTAT 3'; probe: 5' FAM-TAACCAGAATGGAGAACGCAGTG GG-BHQ1 3'). RT-qPCR reactions were carried out on a QuantStudio 3 Real-Time PCR System (Applied Biosystems) or a StepOnePlus Real-Time PCR System (Applied Biosystems) using a program below: reverse transcription at 50°C for 5 minutes, initial denaturation at 95°C for 20 seconds, then 40 cycles of denaturation-annealing-extension at 95°C for 15 seconds and 60°C for 30 seconds. Standard curves were used to calculate E or N sgRNA in copies per ml; the limit of detections (LOD) for both E and N sgRNA assays were 12.5 copies per reaction or 150 copies per mL of BAL/nasal swab/nasal wash.

QUANTIFICATION AND STATISTICAL ANALYSIS

Data were plotted using Prism GraphPad 8.0. Wilcoxon rank sum exact test was performed to compare differences between groups with p-value < 0.05 considered significant using SAS 9.4 (SAS Institute, Cary, NC). No adjustments were made to the p-values for multiple comparisons.

REFERENCES

Afonine, P.V., Poon, B.K., Read, R.J., Sobolev, O.V., Terwilliger, T.C., Urzhumtsev, A., and Adams, P.D. (2018). Real-space refinement in PHENIX for cryo-EM and crystallography. Acta Crystallogr D Struct Biol *74*, 531-544.

Arvin, A.M., Fink, K., Schmid, M.A., Cathcart, A., Spreafico, R., Havenar-Daughton, C., Lanzavecchia, A., Corti, D., and Virgin, H.W. (2020). A perspective on potential antibody-dependent enhancement of SARS-CoV-2. Nature *584*, 353-363.

Baden, L.R., El Sahly, H.M., Essink, B., Kotloff, K., Frey, S., Novak, R., Diemert, D., Spector, S.A., Rouphael, N., Creech, C.B., *et al.* (2021). Efficacy and Safety of the mRNA-1273 SARS-CoV-2 Vaccine. N Engl J Med *384*, 403-416.

Bastard, P., Rosen, L.B., Zhang, Q., Michailidis, E., Hoffmann, H.H., Zhang, Y., Dorgham, K., Philippot, Q., Rosain, J., Beziat, V., *et al.* (2020). Autoantibodies against type I IFNs in patients with life-threatening COVID-19. Science *370*.

951 Baum, A., Ajithdoss, D., Copin, R., Zhou, A., Lanza, K., Negron, N., Ni, M., Wei, Y., Mohammadi, K.,
952 Musser, B., *et al.* (2020a). REGN-COV2 antibodies prevent and treat SARS-CoV-2 infection in rhesus
953 macaques and hamsters. Science *370*, 1110-1115.
954 Baum, A., Fulton, B.O., Wloga, E., Copin, R., Pascal, K.E., Russo, V., Giordano, S., Lanza, K., Negron,
955 N., Ni, M., *et al.* (2020b). Antibody cocktail to SARS-CoV-2 spike protein prevents rapid mutational
956 escape seen with individual antibodies. Science *369*, 1014-1018.
957 Berry, J.D., Jones, S., Drebot, M.A., Andonov, A., Sabara, M., Yuan, X.Y., Weingartl, H., Fernando, L.,
958 Marszal, P., Gren, J., *et al.* (2004). Development and characterisation of neutralising monoclonal
959 antibody to the SARS-coronavirus. J Virol Methods *120*, 87-96.
960 Bournazos, S., Gupta, A., and Ravetch, J.V. (2020). The role of IgG Fc receptors in antibody-dependent
961 enhancement. Nat Rev Immunol *20*, 633-643.
962 Brouwer, P.J.M., Caniels, T.G., van der Straten, K., Snitselaar, J.L., Aldon, Y., Bangaru, S., Torres, J.L.,
963 Okba, N.M.A., Claireaux, M., Kerster, G., *et al.* (2020). Potent neutralizing antibodies from COVID-19
964 patients define multiple targets of vulnerability. Science *369*, 643-650.
965 Cao, Y., Su, B., Guo, X., Sun, W., Deng, Y., Bao, L., Zhu, Q., Zhang, X., Zheng, Y., Geng, C., *et al.*
966 (2020). Potent Neutralizing Antibodies against SARS-CoV-2 Identified by High-Throughput Single-Cell
967 Sequencing of Convalescent Patients' B Cells. Cell *182*, 73-84 e16.
968 Chi, X., Yan, R., Zhang, J., Zhang, G., Zhang, Y., Hao, M., Zhang, Z., Fan, P., Dong, Y., Yang, Y., *et al.*
969 (2020). A potent neutralizing human antibody reveals the N-terminal domain of the Spike protein of
970 SARS-CoV-2 as a site of vulnerability.
971 Coleman, C.M., and Frieman, M.B. (2015). Growth and Quantification of MERS-CoV Infection. Curr
972 Protoc Microbiol *37*, 15E 12 11-19.
973 Croll, T.I. (2018). ISOLDE: a physically realistic environment for model building into low-resolution
974 electron-density maps. Acta Crystallogr D Struct Biol *74*, 519-530.

Dekkers, G., Bentlage, A.E.H., Stegmann, T.C., Howie, H.L., Lissenberg-Thunnissen, S., Zimring, J., Rispens, T., and Vidarsson, G. (2017). Affinity of human IgG subclasses to mouse Fc gamma receptors. MAbs *9*, 767-773.

Dinnon, K.H., 3rd, Leist, S.R., Schafer, A., Edwards, C.E., Martinez, D.R., Montgomery, S.A., West, A., Yount, B.L., Jr., Hou, Y.J., Adams, L.E., *et al.* (2020). A mouse-adapted model of SARS-CoV-2 to test COVID-19 countermeasures. Nature *586*, 560-566.

Edwards, R.J., Mansouri, K., Stalls, V., Manne, K., Watts, B., Parks, R., Janowska, K., Gobeil, S.M.C., Kopp, M., Li, D., *et al.* (2021). Cold sensitivity of the SARS-CoV-2 spike ectodomain. Nat Struct Mol Biol *28*, 128-131.

Emsley, P., and Cowtan, K. (2004). Coot: model-building tools for molecular graphics. Acta Crystallogr D Biol Crystallogr *60*, 2126-2132.

Emsley, P., Lohkamp, B., Scott, W.G., and Cowtan, K. (2010). Features and development of Coot. Acta Crystallogr D Biol Crystallogr *66*, 486-501.

Garcia-Beltran, W.F., Lam, E.C., Astudillo, M.G., Yang, D., Miller, T.E., Feldman, J., Hauser, B.M., Caradonna, T.M., Clayton, K.L., Nitido, A.D., *et al.* (2020). COVID-19 neutralizing antibodies predict disease severity and survival. medRxiv.

Goddard, T.D., Huang, C.C., Meng, E.C., Pettersen, E.F., Couch, G.S., Morris, J.H., and Ferrin, T.E. (2018). UCSF ChimeraX: Meeting modern challenges in visualization and analysis. Protein Sci *27*, 14-25.

Graham, B.S. (2020). Rapid COVID-19 vaccine development. Science *368*, 945-946.

Grant, R.A., Morales-Nebreda, L., Markov, N.S., Swaminathan, S., Querrey, M., Guzman, E.R., Abbott, D.A., Donnelly, H.K., Donayre, A., Goldberg, I.A., *et al.* (2021). Circuits between infected macrophages and T cells in SARS-CoV-2 pneumonia. Nature *590*, 635-641.

Hansen, J., Baum, A., Pascal, K.E., Russo, V., Giordano, S., Wloga, E., Fulton, B.O., Yan, Y., Koon, K., Patel, K., *et al.* (2020). Studies in humanized mice and convalescent humans yield a SARS-CoV-2 antibody cocktail. Science *369*, 1010-1014.

1000 Hassan, A.O., Case, J.B., Winkler, E.S., Thackray, L.B., Kafai, N.M., Bailey, A.L., McCune, B.T., Fox,
1001 J.M., Chen, R.E., Alsoussi, W.B., *et al.* (2020). A SARS-CoV-2 Infection Model in Mice Demonstrates
1002 Protection by Neutralizing Antibodies. Cell *182*, 744-753 e744.
1003 Hauser, B.M., Sangesland, M., Lam, E.C., Feldman, J., Yousif, A.S., Caradonna, T.M., Balazs, A.B.,
1004 Lingwood, D., and Schmidt, A.G. (2020). Engineered receptor binding domain immunogens elicit pan-
1005 coronavirus neutralizing antibodies. bioRxiv, 2020.2012.2007.415216.
1006 Haynes, B.F., Corey, L., Fernandes, P., Gilbert, P.B., Hotez, P.J., Rao, S., Santos, M.R., Schuitemaker, H.,
1007 Watson, M., and Arvin, A. (2020). Prospects for a safe COVID-19 vaccine. Sci Transl Med *12*.
1008 Henderson, R., Edwards, R.J., Mansouri, K., Janowska, K., Stalls, V., Gobeil, S.M.C., Kopp, M., Li, D.,
1009 Parks, R., Hsu, A.L., *et al.* (2020). Controlling the SARS-CoV-2 spike glycoprotein conformation. Nat
1010 Struct Mol Biol *27*, 925-933.
1011 Hou, Y.J., Okuda, K., Edwards, C.E., Martinez, D.R., Asakura, T., Dinnon, K.H., 3rd, Kato, T., Lee, R.E.,
1012 Yount, B.L., Mascenik, T.M., *et al.* (2020). SARS-CoV-2 Reverse Genetics Reveals a Variable Infection
1013 Gradient in the Respiratory Tract. Cell *182*, 429-446 e414.
1014 Hsieh, C.L., Goldsmith, J.A., Schaub, J.M., DiVenere, A.M., Kuo, H.C., Javanmardi, K., Le, K.C.,
1015 Wrapp, D., Lee, A.G., Liu, Y., *et al.* (2020). Structure-based design of prefusion-stabilized SARS-CoV-2
1016 spikes. Science *369*, 1501-1505.
1017 Hui, K.P.Y., Cheung, M.C., Perera, R., Ng, K.C., Bui, C.H.T., Ho, J.C.W., Ng, M.M.T., Kuok, D.I.T.,
1018 Shih, K.C., Tsao, S.W., *et al.* (2020). Tropism, replication competence, and innate immune responses of
1019 the coronavirus SARS-CoV-2 in human respiratory tract and conjunctiva: an analysis in ex-vivo and in-
1020 vitro cultures. Lancet Respir Med *8*, 687-695.
1021 Huo, J., Le Bas, A., Ruza, R.R., Duyvesteyn, H.M.E., Mikolajek, H., Malinauskas, T., Tan, T.K., Rijal, P.,
1022 Dumoux, M., Ward, P.N., *et al.* (2020). Neutralizing nanobodies bind SARS-CoV-2 spike RBD and
1023 block interaction with ACE2. Nat Struct Mol Biol *27*, 846-854.

Iwasaki, A., and Yang, Y. (2020). The potential danger of suboptimal antibody responses in COVID-19. Nat Rev Immunol *20*, 339-341.

Jackson, L.A., Anderson, E.J., Rouphael, N.G., Roberts, P.C., Makhene, M., Coler, R.N., McCullough, M.P., Chappell, J.D., Denison, M.R., Stevens, L.J., *et al.* (2020). An mRNA Vaccine against SARS-CoV-2 - Preliminary Report. N Engl J Med *383*, 1920-1931.

Jaume, M., Yip, M.S., Cheung, C.Y., Leung, H.L., Li, P.H., Kien, F., Dutry, I., Callendret, B., Escriou, N., Altmeyer, R., *et al.* (2011). Anti-severe acute respiratory syndrome coronavirus spike antibodies trigger infection of human immune cells via a pH- and cysteine protease-independent FcgammaR pathway. J Virol *85*, 10582-10597.

Jones, B.E., Brown-Augsburger, P.L., Corbett, K.S., Westendorf, K., Davies, J., Cujec, T.P., Wiethoff, C.M., Blackbourne, J.L., Heinz, B.A., Foster, D., *et al.* (2020). LY-CoV555, a rapidly isolated potent neutralizing antibody, provides protection in a non-human primate model of SARS-CoV-2 infection. bioRxiv.

Joyner, M.J., Senefeld, J.W., Klassen, S.A., Mills, J.R., Johnson, P.W., Theel, E.S., Wiggins, C.C., Bruno, K.A., Klompas, A.M., Lesser, E.R., *et al.* (2020). Effect of Convalescent Plasma on Mortality among Hospitalized Patients with COVID-19: Initial Three-Month Experience. medRxiv, 2020.2008.2012.20169359.

Ju, B., Zhang, Q., Ge, J., Wang, R., Sun, J., Ge, X., Yu, J., Shan, S., Zhou, B., Song, S., *et al.* (2020). Human neutralizing antibodies elicited by SARS-CoV-2 infection. Nature *584*, 115-119.

Kam, Y.W., Kien, F., Roberts, A., Cheung, Y.C., Lamirande, E.W., Vogel, L., Chu, S.L., Tse, J., Guarner, J., Zaki, S.R., *et al.* (2007). Antibodies against trimeric S glycoprotein protect hamsters against SARS-CoV challenge despite their capacity to mediate FcgammaRII-dependent entry into B cells in vitro. Vaccine *25*, 729-740.

1047 Kepler, T.B., Munshaw, S., Wiehe, K., Zhang, R., Yu, J.S., Woods, C.W., Denny, T.N., Tomaras, G.D.,
1048 Alam, S.M., Moody, M.A., *et al.* (2014). Reconstructing a B-Cell Clonal Lineage. II. Mutation, Selection,
1049 and Affinity Maturation. Front Immunol *5*, 170.
1050 Kint, J., Maier, H.J., and Jagt, E. (2015). Quantification of infectious bronchitis coronavirus by titration in
1051 vitro and in ovo. Methods Mol Biol *1282*, 89-98.
1052 Korber, B., Fischer, W.M., Gnanakaran, S., Yoon, H., Theiler, J., Abfalterer, W., Hengartner, N., Giorgi,
1053 E.E., Bhattacharya, T., Foley, B., *et al.* (2020). Tracking Changes in SARS-CoV-2 Spike: Evidence that
1054 D614G Increases Infectivity of the COVID-19 Virus. Cell *182*, 812-827 e819.
1055 Lee, W.S., Wheatley, A.K., Kent, S.J., and DeKosky, B.J. (2020). Antibody-dependent enhancement and
1056 SARS-CoV-2 vaccines and therapies. Nat Microbiol *5*, 1185-1191.
1057 Leist, S.R., Dinnon, K.H., 3rd, Schafer, A., Tse, L.V., Okuda, K., Hou, Y.J., West, A., Edwards, C.E.,
1058 Sanders, W., Fritch, E.J., *et al.* (2020a). A Mouse-Adapted SARS-CoV-2 Induces Acute Lung Injury and
1059 Mortality in Standard Laboratory Mice. Cell *183*, 1070-1085 e1012.
1060 Leist, S.R., Schafer, A., and Martinez, D.R. (2020b). Cell and animal models of SARS-CoV-2
1061 pathogenesis and immunity. Dis Model Mech *13*.
1062 Liao, H.X., Levesque, M.C., Nagel, A., Dixon, A., Zhang, R., Walter, E., Parks, R., Whitesides, J.,
1063 Marshall, D.J., Hwang, K.K., *et al.* (2009). High-throughput isolation of immunoglobulin genes from
1064 single human B cells and expression as monoclonal antibodies. J Virol Methods *158*, 171-179.
1065 Liao, H.X., Lynch, R., Zhou, T., Gao, F., Alam, S.M., Boyd, S.D., Fire, A.Z., Roskin, K.M., Schramm,
1066 C.A., Zhang, Z., *et al.* (2013). Co-evolution of a broadly neutralizing HIV-1 antibody and founder virus.
1067 Nature *496*, 469-476.
1068 Liebschner, D., Afonine, P.V., Baker, M.L., Bunkoczi, G., Chen, V.B., Croll, T.I., Hintze, B., Hung,
1069 L.W., Jain, S., McCoy, A.J., *et al.* (2019). Macromolecular structure determination using X-rays, neutrons
1070 and electrons: recent developments in Phenix. Acta Crystallogr D Struct Biol *75*, 861-877.

Liu, L., Wang, P., Nair, M.S., Yu, J., Rapp, M., Wang, Q., Luo, Y., Chan, J.F., Sahi, V., Figueroa, A., *et al.* (2020a). Potent neutralizing antibodies against multiple epitopes on SARS-CoV-2 spike. Nature *584*, 450-456.

Liu, Y., Soh, W.T., Tada, A., Arakawa, A., Matsuoka, S., Nakayama, E.E., Li, S., Ono, C., Torii, S., Kishida, K., *et al.* (2020b). An infectivity-enhancing site on the SARS-CoV-2 spike protein is targeted by COVID-19 patient antibodies. bioRxiv, 2020.2012.2018.423358.

Menachery, V.D., Yount, B.L., Jr., Sims, A.C., Debbink, K., Agnihothram, S.S., Gralinski, L.E., Graham, R.L., Scobey, T., Plante, J.A., Royal, S.R., *et al.* (2016). SARS-like WIV1-CoV poised for human emergence. Proc Natl Acad Sci U S A *113*, 3048-3053.

Nagashima, H., Ootsubo, M., Fukazawa, M., Motoi, S., Konakahara, S., and Masuho, Y. (2011). Enhanced antibody-dependent cellular phagocytosis by chimeric monoclonal antibodies with tandemly repeated Fc domains. J Biosci Bioeng *111*, 391-396.

Nagashima, H., Tezuka, T., Tsuchida, W., Maeda, H., Kohroki, J., and Masuho, Y. (2008). Tandemly repeated Fc domain augments binding avidities of antibodies for Fcgamma receptors, resulting in enhanced antibody-dependent cellular cytotoxicity. Mol Immunol *45*, 2752-2763.

Naldini, L., Blomer, U., Gage, F.H., Trono, D., and Verma, I.M. (1996). Efficient transfer, integration, and sustained long-term expression of the transgene in adult rat brains injected with a lentiviral vector. Proc Natl Acad Sci U S A *93*, 11382-11388.

Pak, J.E., Sharon, C., Satkunarajah, M., Auperin, T.C., Cameron, C.M., Kelvin, D.J., Seetharaman, J., Cochrane, A., Plummer, F.A., Berry, J.D., *et al.* (2009). Structural insights into immune recognition of the severe acute respiratory syndrome coronavirus S protein receptor binding domain. J Mol Biol *388*, 815-823.

Perez, L.G., Costa, M.R., Todd, C.A., Haynes, B.F., and Montefiori, D.C. (2009). Utilization of immunoglobulin G Fc receptors by human immunodeficiency virus type 1: a specific role for antibodies against the membrane-proximal external region of gp41. J Virol *83*, 7397-7410.

Pettersen, E.F., Goddard, T.D., Huang, C.C., Couch, G.S., Greenblatt, D.M., Meng, E.C., and Ferrin, T.E. (2004). UCSF Chimera--a visualization system for exploratory research and analysis. J Comput Chem *25*, 1605-1612.

Pinto, D., Park, Y.J., Beltramello, M., Walls, A.C., Tortorici, M.A., Bianchi, S., Jaconi, S., Culap, K., Zatta, F., De Marco, A., *et al.* (2020). Cross-neutralization of SARS-CoV-2 by a human monoclonal SARS-CoV antibody. Nature *583*, 290-295.

Polack, F.P., Thomas, S.J., Kitchin, N., Absalon, J., Gurtman, A., Lockhart, S., Perez, J.L., Perez Marc, G., Moreira, E.D., Zerbini, C., *et al.* (2020). Safety and Efficacy of the BNT162b2 mRNA Covid-19 Vaccine. N Engl J Med *383*, 2603-2615.

Punjani, A., Rubinstein, J.L., Fleet, D.J., and Brubaker, M.A. (2017). cryoSPARC: algorithms for rapid unsupervised cryo-EM structure determination. Nat Methods *14*, 290-296.

Robbiani, D.F., Gaebler, C., Muecksch, F., Lorenzi, J.C.C., Wang, Z., Cho, A., Agudelo, M., Barnes, C.O., Gazumyan, A., Finkin, S., *et al.* (2020). Convergent antibody responses to SARS-CoV-2 in convalescent individuals. Nature *584*, 437-442.

Rockx, B., Kuiken, T., Herfst, S., Bestebroer, T., Lamers, M.M., Oude Munnink, B.B., de Meulder, D., van Amerongen, G., van den Brand, J., Okba, N.M.A., *et al.* (2020). Comparative pathogenesis of COVID-19, MERS, and SARS in a nonhuman primate model. Science *368*, 1012-1015.

Rogers, T.F., Zhao, F., Huang, D., Beutler, N., Burns, A., He, W.T., Limbo, O., Smith, C., Song, G., Woehl, J., *et al.* (2020). Isolation of potent SARS-CoV-2 neutralizing antibodies and protection from disease in a small animal model. Science *369*, 956-963.

Saunders, K.O. (2019). Conceptual Approaches to Modulating Antibody Effector Functions and Circulation Half-Life. Front Immunol *10*, 1296.

Schafer, A., Muecksch, F., Lorenzi, J.C.C., Leist, S.R., Cipolla, M., Bournazos, S., Schmidt, F., Maison, R.M., Gazumyan, A., Martinez, D.R., *et al.* (2021). Antibody potency, effector function, and combinations in protection and therapy for SARS-CoV-2 infection in vivo. J Exp Med *218*.

1121 Scheres, S.H. (2012). A Bayesian view on cryo-EM structure determination. J Mol Biol *415*, 406-418.
1122 Scheres, S.H.W. (2016). Processing of Structurally Heterogeneous Cryo-EM Data in RELION. In The
1123 Resolution Revolution: Recent Advances In cryoEM, pp. 125-157.
1124 Schrodinger, L. (2015). The PyMOL Molecular Graphics System.
1125 Sempowski, G.D., Saunders, K.O., Acharya, P., Wiehe, K.J., and Haynes, B.F. (2020). Pandemic
1126 Preparedness: Developing Vaccines and Therapeutic Antibodies For COVID-19. Cell *181*, 1458-1463.
1127 Sheahan, T.P., Sims, A.C., Graham, R.L., Menachery, V.D., Gralinski, L.E., Case, J.B., Leist, S.R., Pyrc,
1128 K., Feng, J.Y., Trantcheva, I., *et al.* (2017). Broad-spectrum antiviral GS-5734 inhibits both epidemic and
1129 zoonotic coronaviruses. Sci Transl Med *9*.
1130 Shi, R., Shan, C., Duan, X., Chen, Z., Liu, P., Song, J., Song, T., Bi, X., Han, C., Wu, L., *et al.* (2020). A
1131 human neutralizing antibody targets the receptor-binding site of SARS-CoV-2. Nature *584*, 120-124.
1132 Suloway, C., Pulokas, J., Fellmann, D., Cheng, A., Guerra, F., Quispe, J., Stagg, S., Potter, C.S., and
1133 Carragher, B. (2005). Automated molecular microscopy: the new Leginon system. J Struct Biol *151*, 41-
1134 60.
1135 Takada, A., Ebihara, H., Feldmann, H., Geisbert, T.W., and Kawaoka, Y. (2007). Epitopes required for
1136 antibody-dependent enhancement of Ebola virus infection. J Infect Dis *196 Suppl 2*, S347-356.
1137 Ubol, S., and Halstead, S.B. (2010). How innate immune mechanisms contribute to antibody-enhanced
1138 viral infections. Clin Vaccine Immunol *17*, 1829-1835.
1139 Walls, A.C., Park, Y.J., Tortorici, M.A., Wall, A., McGuire, A.T., and Veesler, D. (2020). Structure,
1140 Function, and Antigenicity of the SARS-CoV-2 Spike Glycoprotein. Cell *181*, 281-292 e286.
1141 Wan, Y., Shang, J., Sun, S., Tai, W., Chen, J., Geng, Q., He, L., Chen, Y., Wu, J., Shi, Z., *et al.* (2020).
1142 Molecular Mechanism for Antibody-Dependent Enhancement of Coronavirus Entry. J Virol *94*.
1143 Wang, Q., Chen, Y., Pelletier, M., Cvitkovic, R., Bonnell, J., Chang, C.Y., Koksal, A.C., O'Connor, E.,
1144 Gao, X., Yu, X.Q., *et al.* (2017). Enhancement of antibody functions through Fc multiplications. MAbs *9*,
1145 393-403.

Wang, Q., Zhang, L., Kuwahara, K., Li, L., Liu, Z., Li, T., Zhu, H., Liu, J., Xu, Y., Xie, J., *et al.* (2016). Immunodominant SARS Coronavirus Epitopes in Humans Elicited both Enhancing and Neutralizing Effects on Infection in Non-human Primates. ACS Infect Dis *2*, 361-376.

Wang, S.F., Tseng, S.P., Yen, C.H., Yang, J.Y., Tsao, C.H., Shen, C.W., Chen, K.H., Liu, F.T., Liu, W.T., Chen, Y.M., *et al.* (2014). Antibody-dependent SARS coronavirus infection is mediated by antibodies against spike proteins. Biochem Biophys Res Commun *451*, 208-214.

Wec, A.Z., Wrapp, D., Herbert, A.S., Maurer, D.P., Haslwanter, D., Sakharkar, M., Jangra, R.K., Dieterle, M.E., Lilov, A., Huang, D., *et al.* (2020). Broad neutralization of SARS-related viruses by human monoclonal antibodies. Science *369*, 731-736.

Whittle, J.R., Zhang, R., Khurana, S., King, L.R., Manischewitz, J., Golding, H., Dormitzer, P.R., Haynes, B.F., Walter, E.B., Moody, M.A., *et al.* (2011). Broadly neutralizing human antibody that recognizes the receptor-binding pocket of influenza virus hemagglutinin. Proc Natl Acad Sci U S A *108*, 14216-14221.

Wolfel, R., Corman, V.M., Guggemos, W., Seilmaier, M., Zange, S., Muller, M.A., Niemeyer, D., Jones, T.C., Vollmar, P., Rothe, C., *et al.* (2020). Virological assessment of hospitalized patients with COVID-2019. Nature *581*, 465-469.

Wrammert, J., Smith, K., Miller, J., Langley, W.A., Kokko, K., Larsen, C., Zheng, N.Y., Mays, I., Garman, L., Helms, C., *et al.* (2008). Rapid cloning of high-affinity human monoclonal antibodies against influenza virus. Nature *453*, 667-671.

Wrapp, D., De Vlieger, D., Corbett, K.S., Torres, G.M., Wang, N., Van Breedam, W., Roose, K., van Schie, L., Team, V.-C.C.-R., Hoffmann, M., *et al.* (2020a). Structural Basis for Potent Neutralization of Betacoronaviruses by Single-Domain Camelid Antibodies. Cell *181*, 1004-1015 e1015.

Wrapp, D., Wang, N., Corbett, K.S., Goldsmith, J.A., Hsieh, C.L., Abiona, O., Graham, B.S., and McLellan, J.S. (2020b). Cryo-EM structure of the 2019-nCoV spike in the prefusion conformation. Science *367*, 1260-1263.

Wu, Y., Wang, F., Shen, C., Peng, W., Li, D., Zhao, C., Li, Z., Li, S., Bi, Y., Yang, Y., *et al.* (2020). A noncompeting pair of human neutralizing antibodies block COVID-19 virus binding to its receptor ACE2. Science *368*, 1274-1278.

Yilla, M., Harcourt, B.H., Hickman, C.J., McGrew, M., Tamin, A., Goldsmith, C.S., Bellini, W.J., and Anderson, L.J. (2005). SARS-coronavirus replication in human peripheral monocytes/macrophages. Virus Res *107*, 93-101.

Yip, M.S., Leung, H.L., Li, P.H., Cheung, C.Y., Dutry, I., Li, D., Daeron, M., Bruzzone, R., Peiris, J.S., and Jaume, M. (2016). Antibody-dependent enhancement of SARS coronavirus infection and its role in the pathogenesis of SARS. Hong Kong Med J *22*, 25-31.

Yip, M.S., Leung, N.H., Cheung, C.Y., Li, P.H., Lee, H.H., Daeron, M., Peiris, J.S., Bruzzone, R., and Jaume, M. (2014). Antibody-dependent infection of human macrophages by severe acute respiratory syndrome coronavirus. Virol J *11*, 82.

Yu, J., Tostanoski, L.H., Peter, L., Mercado, N.B., McMahan, K., Mahrokhian, S.H., Nkolola, J.P., Liu, J., Li, Z., Chandrashekar, A., *et al.* (2020). DNA vaccine protection against SARS-CoV-2 in rhesus macaques. Science *369*, 806-811.

Zhang, Q., Bastard, P., Liu, Z., Le Pen, J., Moncada-Velez, M., Chen, J., Ogishi, M., Sabli, I.K.D., Hodeib, S., Korol, C., *et al.* (2020). Inborn errors of type I IFN immunity in patients with life-threatening COVID-19. Science *370*.

Zheng, S.Q., Palovcak, E., Armache, J.P., Verba, K.A., Cheng, Y., and Agard, D.A. (2017). MotionCor2: anisotropic correction of beam-induced motion for improved cryo-electron microscopy. Nat Methods *14*, 331-332.

Zhou, D., Duyvesteyn, H.M.E., Chen, C.P., Huang, C.G., Chen, T.H., Shih, S.R., Lin, Y.C., Cheng, C.Y., Cheng, S.H., Huang, Y.C., *et al.* (2020a). Structural basis for the neutralization of SARS-CoV-2 by an antibody from a convalescent patient. Nat Struct Mol Biol *27*, 950-958.

1194 Zhou, J., Chu, H., Li, C., Wong, B.H., Cheng, Z.S., Poon, V.K., Sun, T., Lau, C.C., Wong, K.K., Chan,
1195 J.Y., *et al.* (2014). Active replication of Middle East respiratory syndrome coronavirus and aberrant
1196 induction of inflammatory cytokines and chemokines in human macrophages: implications for
1197 pathogenesis. J Infect Dis *209*, 1331-1342.
1198 Zhou, T., Teng, I.T., Olia, A.S., Cerutti, G., Gorman, J., Nazzari, A., Shi, W., Tsybovsky, Y., Wang, L.,
1199 Wang, S., *et al.* (2020b). Structure-Based Design with Tag-Based Purification and In-Process
1200 Biotinylation Enable Streamlined Development of SARS-CoV-2 Spike Molecular Probes. Cell Rep *33*,
1201 108322.
1202 Zost, S.J., Gilchuk, P., Case, J.B., Binshtein, E., Chen, R.E., Nkolola, J.P., Schafer, A., Reidy, J.X.,
1203 Trivette, A., Nargi, R.S., *et al.* (2020a). Potently neutralizing and protective human antibodies against
1204 SARS-CoV-2. Nature *584*, 443-449.
1205 Zost, S.J., Gilchuk, P., Chen, R.E., Case, J.B., Reidy, J.X., Trivette, A., Nargi, R.S., Sutton, R.E.,
1206 Suryadevara, N., Chen, E.C., *et al.* (2020b). Rapid isolation and profiling of a diverse panel of human
1207 monoclonal antibodies targeting the SARS-CoV-2 spike protein. Nat Med *26*, 1422-1427.
1208
1209

Supplementary Figure Legends

Figure S1. Isolation of SARS-CoV-2-reactive Abs from single cell-sorted plasmablasts and memory B cells of SARS-CoV-2 and SARS-CoV-1 convalescent donors. Related to Figure 1.

(A) Symptom severity scores of the COVID-19 convalescent donor. The method to determine severity score is in supplementary online material. Red arrows indicate the blood sampling time points that we used to isolate Abs.

(B) Viral load from nasopharyngeal (NP) swabs.

(C) Serum micro-neutralization titer. Micro-Neutralization titers were defined as the highest serum dilution that neutralize all the virus, or 99% inhibitory concentration (IC_{99}).

(D) Flow cytometry gating strategy for unbiased plasmablasts sorting or antigen specific-memory B cells sorting. At day 11 and day 15 post onset of COVID-19 symptom, plasmablasts ($CD14^-/CD16^-/CD3^-/CD235a^-/CD19^+/CD20^{low}/IgD^-/CD27^{high}/CD38^{high}$) from a SARS-CoV-2 donor. Antigen specific B cells from SARS-CoV-1 and SARS-CoV-2 donors were sorted with different combinations of the SARS-CoV-2 S-2P, RBD, NTD probes. Representative data for sorting Spike double positive, $Spike^+$ or NTD^+, as well as RBD^+ or NTD^+ subsets were shown.

(E-H) Neutralization activity of RBD Abs. (E) Proportion of SARS-CoV-2 RBD Abs (n=81) that exhibited detectable neutralization in the microneutralization assay. (F) Neutralization IC_{50} and IC_{80} of RBD neutralizing Abs (NAbs) against pseudotyped SARS-CoV-2. (G) Microneutralization titer, plaque reduction neutralization test (PRNT) IC_{50} and IC_{80} of RBD NAbs against replication-competent SARS-CoV-2. Microneutralization titer was defined as the lowest Ab concentration that neutralize all the virus, or 99% inhibitory concentration (IC_{99}). Abs with undetectable microneutralization titers are shown as gray symbols and nAbs are represented by blue symbols. (H) RBD NAbs blocking of ACE2 binding to SARS-CoV-2 Spike (S) protein. Blocking titer is shown as IC_{50}.

(I-J) Correlation analysis of RBD Abs between neutralization and ACE2 blocking activities. Spearman correlation analysis were performed for (I) ACE2 blocking IC50 vs. PV neutralization IC50, as well as (J) for ACE2 blocking IC50 vs. SARS-CoV-2 neutralization titers (indicated by the lowest concentration that shows no CPE). Purified RBD Abs in Table S1 and S2 that have pseudovirus neutralization data (n=59) or SARS-CoV-2 micro-neutralization assay data (n=80) were used in this analysis. P-value and r were indicated for each figures.

(K-M) Neutralization activity of NTD Abs. (K) Proportion of SARS-CoV-2 NTD Abs (n=41) that exhibited detectable neutralization in the microneutralization assay. (L) Neutralization IC_{50} and IC_{80} of NTD neutralizing Abs

against pseudotyped SARS-CoV-2. (M) Microneutralization titer, PRNT IC_{50} and IC_{80} of NTD neutralizing Abs against replication-competent SARS-CoV-2. Abs with undetectable microneutralization titers are shown as gray symbols and neutralizing Abs are represented by orange symbols. Horizontal bars represent the geometric means for each group of Abs.

Figure S2. Binding and neutralization activities of down-selected SARS-CoV-2 Abs. Related to Figure 2.

(A-D) ELISA binding curves of down-selected Abs. Different SARS-CoV-2 or other CoV viral antigens were coated on plates and detected with serial diluted (A) RBD infection-enhancing Abs, (B) RBD non-infection-enhancing Abs, (C) NTD infection-enhancing Abs, and (D) NTD non-infection-enhancing Abs.

(E-F) Neutralization curves for RBD Abs against pseudotyped (E) and replication-competent (F) SARS-CoV-2.

(G-H) Neutralization curves for NTD Abs against pseudotyped (G) and replication-competent (H) SARS-CoV-2.

(I-L) Neutralization curves for cross-neutralizing Abs against pseudotyped (I) and replication-competent (J) SARS-CoV-2, SARS-CoV-1 nanoluciferase (nLuc) virus (L), and Bat WIV1-CoV nLuc virus (L).

Figure S3. Comparison of RBD and NTD epitopes from NSEM. Related to Figure 2.

(A) A spike model (PDB 6ZGE) and corresponding Fab homology models were manually docked and rigidly fit into each negative stain density map.

(B) The RBD of each model is enlarged and shown as a white surface, with the putative epitope of each Ab colored. Black outline indicates the ACE2 binding footprint.

(C) Comparison to ACE2 footprint and epitopes of three published Abs with similar epitopes. See main text for references.

(D) A spike model (PDB 6ZGE) and corresponding Fab homology models were manually docked and rigidly fit into each negative stain density map.

(E) The NTD of each model is enlarged and shown as a white surface, with the epitope of each Ab colored. Orange outline indicates the epitope of Ab 4A8, shown at bottom right. Outlines illustrate that the neutralizing Abs DH1048-51 share the same epitope, whereas the infection-enhancing Abs DH1053-56 bind a distinct epitope.

(F) The model of spike complex with Fab 4A8 (orange ribbons, PDG 7C2L) is rigidly fit into each of the NSEM maps (transparent surfaces). The close fit of 4A8 into DH1049, DH1050.1 and DH1050.2 indicate theses have the same approach angle as 4A8, whereas DH1048 and DH1051 have slightly different approaches.

Figure S4. In vitro analysis of human Abs and SARS-CoV-2 infected serum samples. Related to Figure 3, Figure 5 and Figure 7.

(A-C) Effect of combining infection-enhancing RBD and NTD Abs on SARS-CoV-2 pseudovirus infection in ACE2-expressing cells. The infection-enhancing NTD Ab DH1052 was tested alone (A) or mixed with infection-enhancing RBD Abs DH1041 (B) or DH1043 (C) in 1:13 ratio or 1:13250 ratio, respectively. The NTD:RBD Ab mixtures (orange), as well as RBD Ab alone (blue), were five-fold serially diluted and tested for neutralization against SARS-CoV-2 D614G pseudovirus in 293T/ACE2 cells.

(D-F) Comparison of RBD and NTD directed serum Ab responses in SARS-CoV-2 infected humans.

(D) Serum IgG binding titers to RBD (blue) and NTD (salmon) as measured by ELISA as log area-under-curve (AUC). Each symbol represents an individual study participant, with the mean binding titer for the visit day shown as a black horizontal bar.

(E) Percent decrease in binding to NTD relative to RBD binding titer. Each symbol represents the change in binding titer for an individual study subject. Mean decrease is shown as a black horizontal bar.

(F) Serum blocking of RBD neutralizing Ab DH1041 (blue) or NTD neutralizing Ab DH1050.1 (salmon), or non-neutralizing Ab DH1052 (burgundy) binding to SARS-CoV-2 spike. Black symbols show individual study participants. Mean blocking percentage for the visit day is shown as a filled bar.

(G-H) Neutralization activities of neutralizing and enhancing Abs against mouse adapted SARS-CoV-2.

(G) NTD neutralizing Abs DH1050.1, RBD neutralizing and enhancing Abs DH1041 were tested for neutralization activities against wild-type (WT) virus, mouse adapted 2AA MA virus, and mouse adapted MA10 virus in live virus neutralization assay. CH65 Ab was used as a control. Mean value of neutralization (%) from duplicate wells were shown.

(H) NTD enhancing Ab DH1052 and control Ab CH65 were tested for neutralization activities against wild-type (WT) virus, mouse adapted 2AA MA virus, and mouse adapted MA10 virus in live virus neutralization assay. Mean value of neutralization (%) from duplicate wells were shown.

Figure S5. Lung histopathology of Ab-treated and SARS-CoV-2 challenged cynomolgus macaques. Related to Figure 5 and Figure 7.

(A) Representative images of hematoxylin and eosin (H&E) staining and SARS-CoV-2 antigen immunohistochemistry (IHC) staining from each group. All images were taken at 10x magnification. The images in this presentation are representative of the average severity of pathologic processes observed and recorded during microscopic evaluation. Red arrows indicate SARS-CoV-2 infection foci.

(B) Following microscopic evaluation of DH1052, 1 animal (BB536A) out of 5 animals in this group exhibited histologic features that was substantially more severe than the rest of the cohort and may suggest some degree of Ab-mediated disease enhancement. The features were characterized by prominent perivascular mononuclear inflammation (*) and a substantial amount of perivascular and alveolar edema (fluid; X). These findings suggest a vaso-centric process with some degree of altered vascular permeability. The remaining 4 animals in DH1052 group had inflammatory changes that ranged from minimal to moderate severity and more infiltrates were mixed and predominantly polymorphonuclear with lesser mononuclear cell involvement and present in the alveolar spaces.

(C-E) Expression of macrophage activation markers in macaque lung tissues. An animal from the CH65 control group (C), the DH1052-treated animal (BB536A) that exhibited substantially more severe lung inflammation (D), and an animal from the NTD NAb DH1050.1 group (E) were selected for Immunohistochemistry (IHC) staining. Immunohistochemical staining was performed using MHCII, CD68, IBA1 and CD163 to detect classically activated macrophages (M1) and/or alternatively activated macrophages (M2). CD11b is a macrophage/monocyte marker and CD3 is a T cell marker. All images are 10x magnification; scale bars= 100µm.

Figure S6. High dose NTD enhancing Ab DH1052 does not enhance SARS-CoV-2 replication or disease *in vivo*. Related to Figure 5.

(A) Diagram of the macaque study design showing cynomolgus macaques (n=5 per group) were infused with high dose (30 mg/kg body weight) DH1052 or an irrelevant control CH65 Ab 3 days before 10^5 PFU of SARS-CoV-2 challenge via intranasal and intratracheal routes. Viral load including viral RNA and subgenomic RNA (sgRNA) were measured at the indicated pre-challenge and post-challenge timepoints. Lungs were harvested on Day 4 post-challenge for histopathology analysis.

(B-D) SARS-CoV-2 (B) E gene sgRNA, (C) N gene sgRNA and (D) E gene total viral RNA in bronchoalveolar lavage (BAL) on Day 2 and Day 4 post challenge.

(E-G) SARS-CoV-2 (E) E gene sgRNA, (F) N gene sgRNA and (G) E gene total viral RNA in nasal swab on Day 2 and Day 4 post challenge.

(H-I) Lung inflammation. Sections of the left caudal (Lc), right middle (Rm), and right caudal (Rc) lung were evaluated and scored for the presence of inflammation by hematoxylin and eosin (H&E) staining. (H) Summary of inflammation scores. Symbols indicate the sums of Lc, Rm, and Rc scores in each animal. (I) Representative images of lung H&E staining.

(J-K) Immunohistochemistry (IHC) staining for the presence of SARS-CoV-2 nucleocapsid in lungs. (J) Summary of IHC scores. Symbols indicate the sums of Lc, Rm, and Rc scores in each animal. (K) Representative images of lung IHC staining. Red arrows indicate SARS-CoV-2 infection foci.

LOD, limit of detection. Statistical significance in all the panels were determined using Wilcoxon rank sum exact test. Asterisks show the statistical significance between indicated group and CH65 control group: ns, not significant, *P<0.05, **P<0.01, ***P<0.001.

Figure S7. Different doses of a cross-neutralizing Ab DH1047 treatments do not enhance SARS-CoV-2 replication *in vivo*. Related to Figure 7.

(A) Diagram of the macaque study design. Cynomolgus macaques (n=5 per group) were infused with DH1047 at the dose of 10 mg/kg, 5 mg/kg, 1 mg/kg, 0.1 mg/kg weight. Macaques treated with 10 mg/kg weight of DH65 Ab were set as the control group. Three days post-infusion, 10^5 PFU of SARS-CoV-2 challenge via intranasal and intratracheal routes. Viral load including viral RNA and subgenomic RNA (sgRNA) were measured at the indicated pre-challenge and post-challenge timepoints. Lungs were harvested on Day 4 post-challenge for histopathology analysis.

(B) Serum human IgG concentrations at Day 2.

(C) Day 2 serum neutralization titers shown as the reciprocal serum dilution that inhibits 50% (ID_{50}) of SARS-CoV-2 replication in Vero cells.

(D-E) SARS-CoV-2 (D) E gene sgRNA and (E) N gene sgRNA in bronchoalveolar lavage (BAL) on Day 2 and Day 4 post challenge.

(F-G) SARS-CoV-2 (F) E gene sgRNA and (G) N gene sgRNA in nasal swab on Day 2 and Day 4 post challenge. (H-I) Lung inflammation. Sections of the left caudal (Lc), right middle (Rm), and right caudal (Rc) lung were evaluated and scored for the presence of inflammation by hematoxylin and eosin (H&E) staining. (H) Summary of inflammation scores. Symbols indicate the sums of Lc, Rm, and Rc scores in each animal. (I) Representative images of lung H&E staining.

(J-K) Immunohistochemistry (IHC) staining for the presence of SARS-CoV-2 nucleocapsid in lungs. (J) Summary of IHC scores. Symbols indicate the sums of Lc, Rm, and Rc scores in each animal. (K) Representative images of lung IHC staining. Red arrows indicate SARS-CoV-2 infection foci.

LOD, limit of detection. Statistical significance in all the panels were determined using Wilcoxon rank sum exact test. Asterisks show the statistical significance between indicated group and CH65 control group: ns, not significant, *P<0.05, **P<0.01, ***P<0.001.

Supplementary Items (available online as excel sheet or PDF format)

Table S1. High-throughput ELISA binding screen of Abs recovered from SARS-CoV-2 and SARS-CoV-1 donors. Related to Figure 1.

Supplementary Table S2. Immunogenetic analysis of select neutralizing and non-neutralizing SARS-CoV-2 Abs. Related to Figure 2.

Table S3. RBD and NTD Fabs affinity for Spike proteins. Related to Figure 2.

Table S4. RBD and NTD Ab affinity for mouse CD16/FcγR3, CD16-2/FcγR4, CD32B/FcγR2b and CD64/FcγR1. Related to Figure 5 and Figure 6.

Table S5. Luminex cytokine profiling of BAL samples from cynomolgus macaques. Data set related to Figure 5 and 7, Figure S6 and Figure S7 were shown in different tabs. BAL samples collected on Day -5 (pre-

challenge), Day 2 and Day 4 post-challenge were concentrated (x10) and measured using a 25-analyte multiplex bead array by Luminex assay. The animal (BB536A) in DH1052 group that exhibited substantially more severe disease and cytokine expression was marked in red.

Supplementary Data 1. Cryo-EM information. Related to Figure 4.

Highlights:

- RBD or NTD antibodies exhibited infection enhancement *in vitro* but not *in vivo*
- Neutralizing or infection-enhancing NTD antibodies bound distinct epitopes
- *In vitro* infection-enhancing antibodies protected from SARS-CoV-2 *in vivo*
- Cross-reactive RBD neutralizing antibodies were protective--most potent, DH1047

eTOC Blurb:

Convalescent human-derived SARS-CoV-2 RBD and NTD antibodies mediated neutralization as well as infection-enhancement *in vitro*, yet infusion of these antibodies in mice or cynomolgus macaques resulted in protection from viral replication.

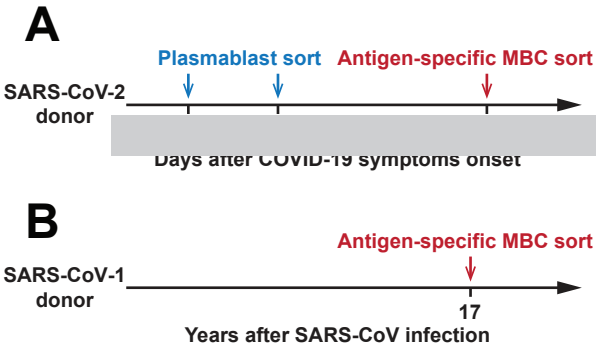

C

Donor	Cell Type	B cells sorted	SARS-CoV-2	RBD	NTD	S2	Spike only	NP
SARS-CoV-2 donor	Plasmablasts	773	101	11	4	42	1	43
SARS-CoV-2 donor	Memory B cells	594	307	121	58	99	29	NA
SARS-CoV-1 donor	Memory B cells	370	55	18	7	7	23	NA
Total		1737	463	150	69	148	53	43
Down-selected for production		NA	187	81	41	65	0	0

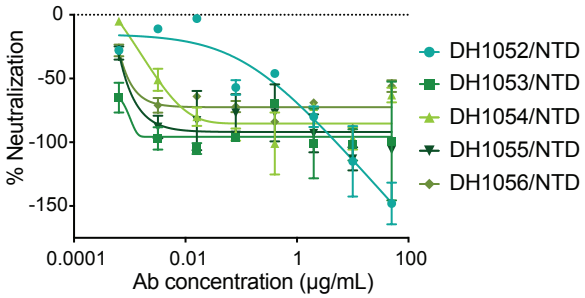

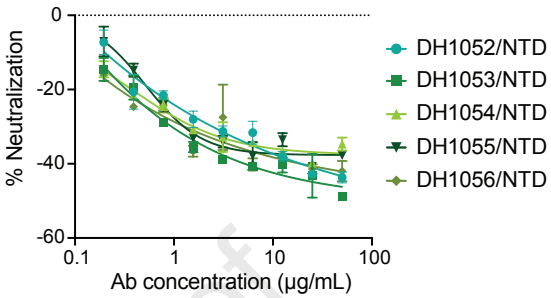

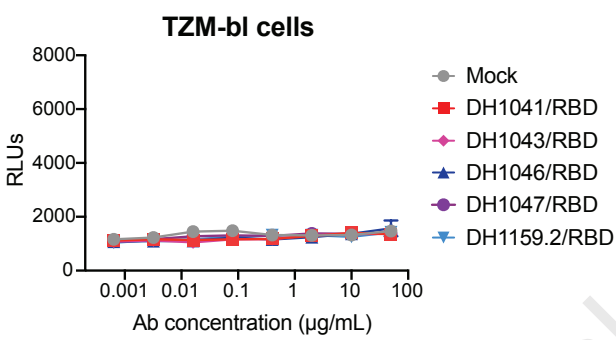

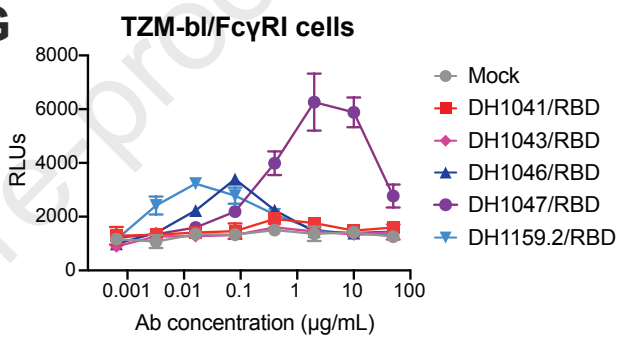

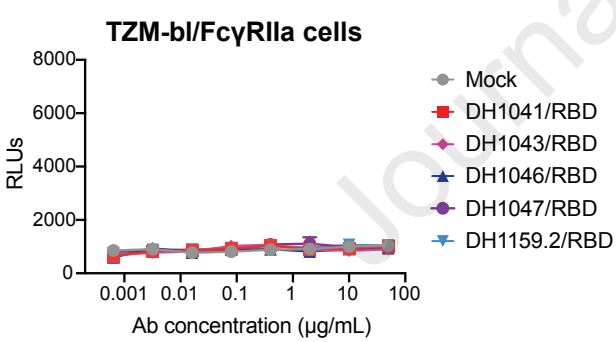

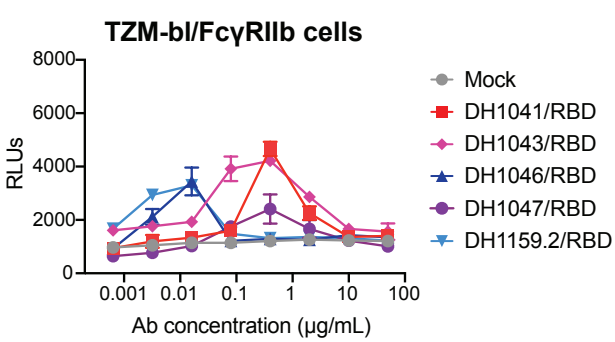

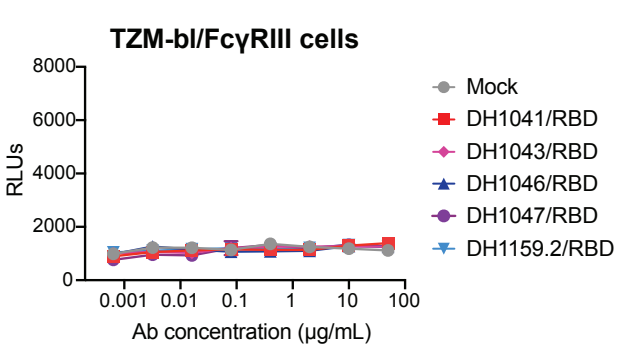

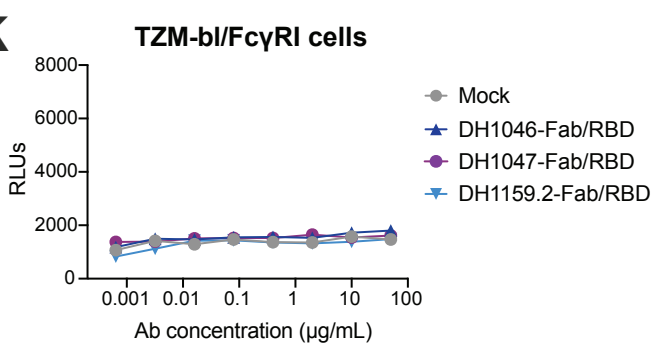

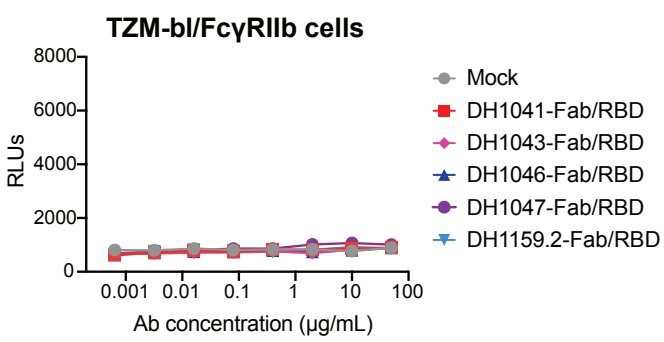

A

Antibody	Epitope	Effect on SARS-CoV-2 infection: ACE2^{pos} FcγR^{neg} cells	Effect on SARS-CoV-2 infection: ACE2^{neg} FcγR^{pos} cells	Cross-reactivity with SARS-CoV-1	ACE2 blocking: IC_{50}	ACE2 blocking: IC_{80}	SARS-CoV-2 pseudovirus: IC_{50}	SARS-CoV-2 pseudovirus: IC_{80}	SARS-CoV-2 pseudovirus: Maximal% inhibition	SARS-CoV-2 replication competent virus: MN titer	SARS-CoV-2 replication competent virus: IC_{50}	SARS-CoV-2 replication competent virus: IC_{80}
DH1041	RBD				0.036	0.497	0.017	0.049	>100	0.098	0.016	0.063
DH1043	RBD				0.043	0.280	0.0015	0.020	>100	0.098	0.034	0.099
DH1159.2	RBD				>50	>50	11.900	>50	77.0	>100	ND	ND
DH1046	RBD				0.201	6.512	0.396	2.030	>100	12.500	1.086	9.383
DH1047	RBD				0.078	0.567	0.090	0.360	>100	1.100	0.124	0.666
DH1042	RBD				0.059	0.371	0.011	0.053	>100	0.280	0.071	0.269
DH1044	RBD				>50	>50	0.021	0.080	98.0	0.550	0.076	0.273
DH1045	RBD				0.226	24.353	0.380	2.260	>100	6.250	1.437	4.827
DH1052	NTD				>50	>50	>50	>50	-148.0	>100	>100	>100
DH1053	NTD				>50	>50	>50	>50	-99.0	>100	>100	>100
DH1054	NTD				>50	>50	>50	>50	-63.0	>100	>100	>100
DH1055	NTD				>50	>50	>50	>50	-106.0	>100	>100	>100
DH1056	NTD				>50	>50	>50	>50	-56.0	>100	>100	>100
DH1048	NTD				>50	>50	0.520	>50	72.0	0.390	0.608	2.232
DH1049	NTD				>50	>50	>50	>50	49.0	0.390	0.385	3.539
DH1050.2	NTD				>50	>50	0.280	>50	67.0	0.780	0.087	1.187
DH1051	NTD				>50	>50	0.049	>50	68.0	0.780	0.134	0.737
DH1050.1	NTD				>50	>50	0.039	>50	62.0	0.780	0.161	0.614

Effect on SARS-CoV-2 infection
- No effect
- Infection-enhancing
- Neutralizing

Cross-reactivity
- Non-reactive
- Reactive

Neutralization titer or blocking titer (μg/mL)
- <0.01
- 0.01-0.1
- 0.1-1
- 1-10
- 10-50
- >50

B

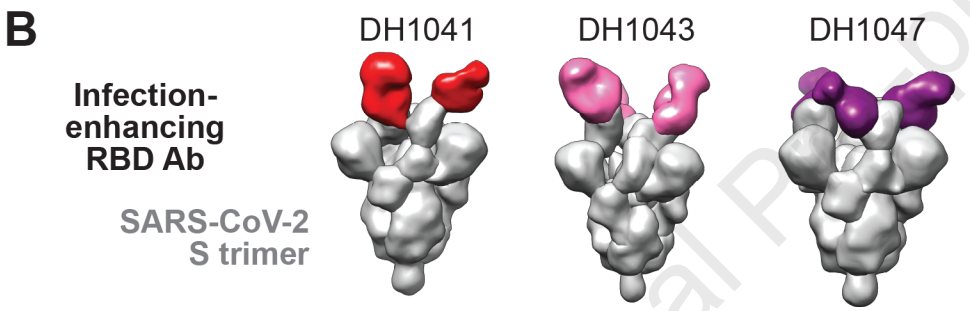

C

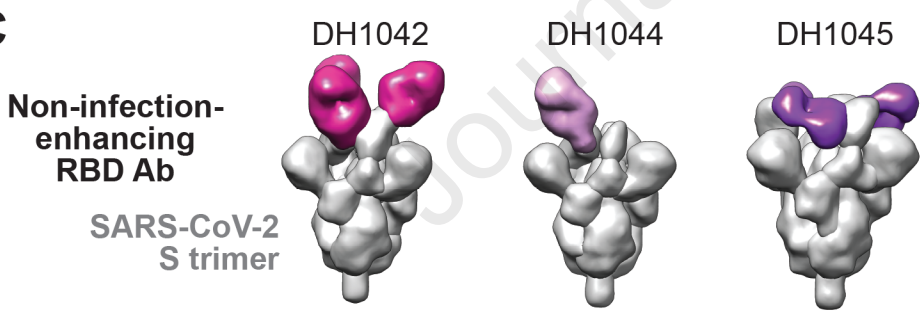

D

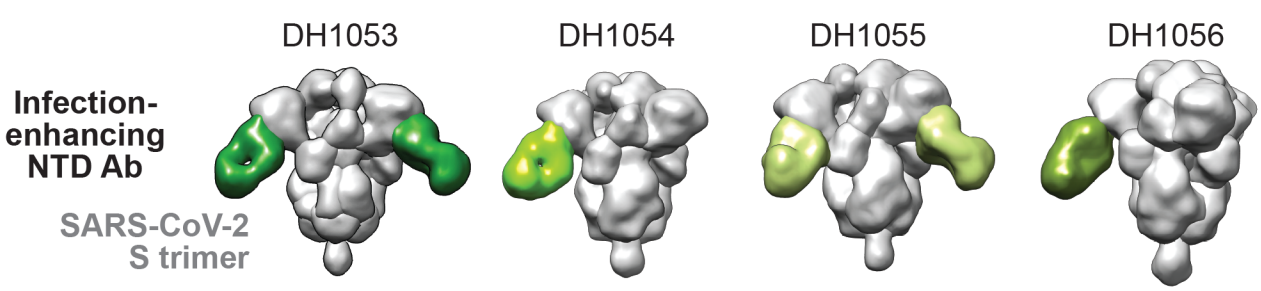

E

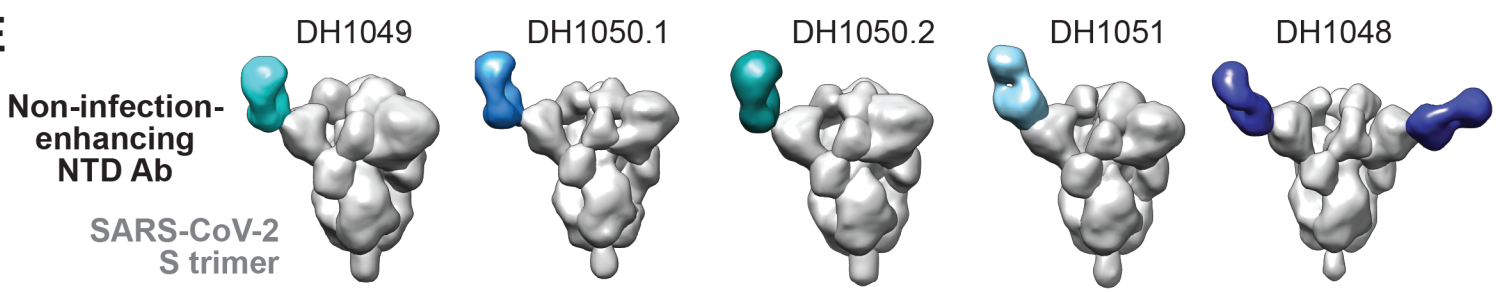

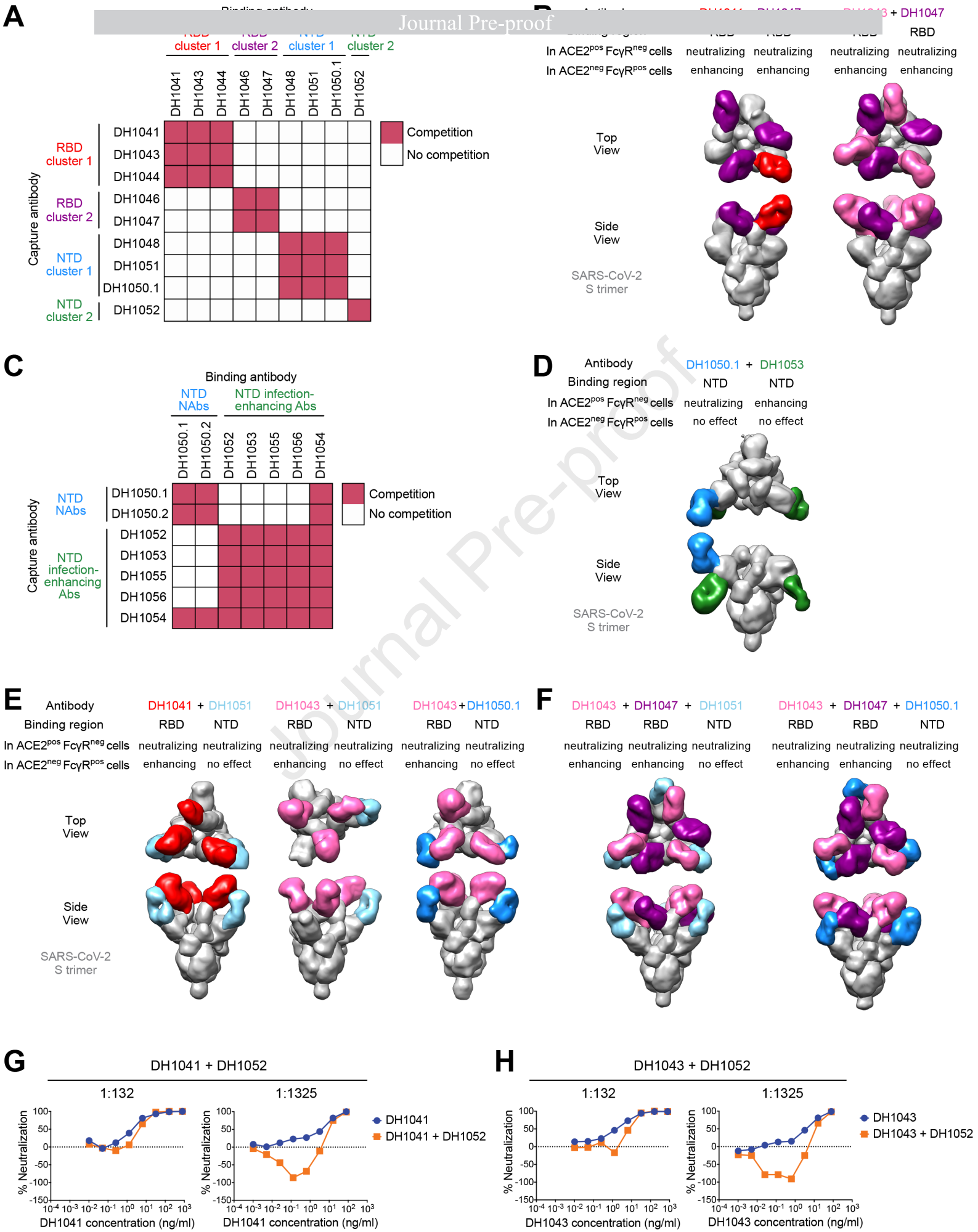

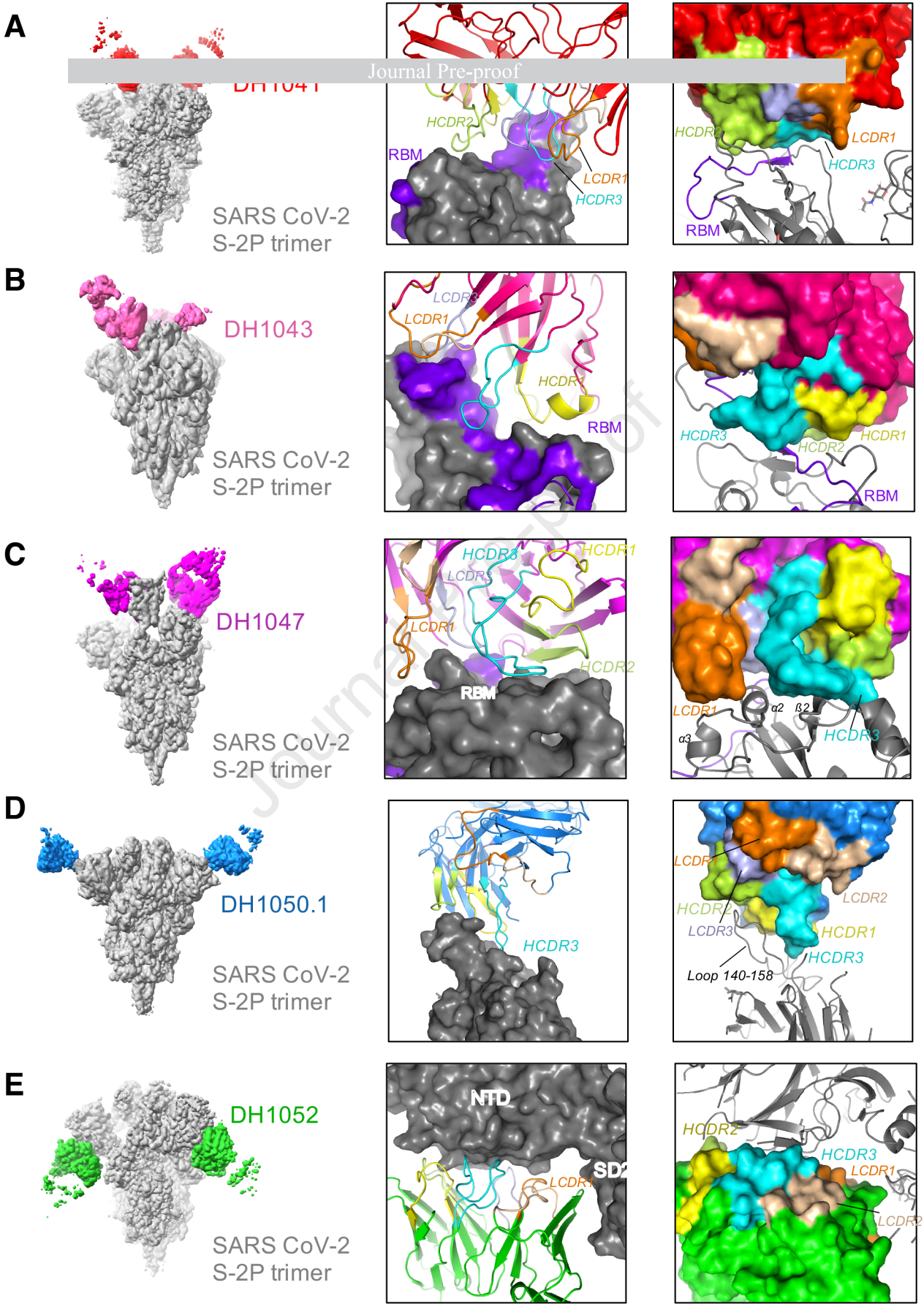

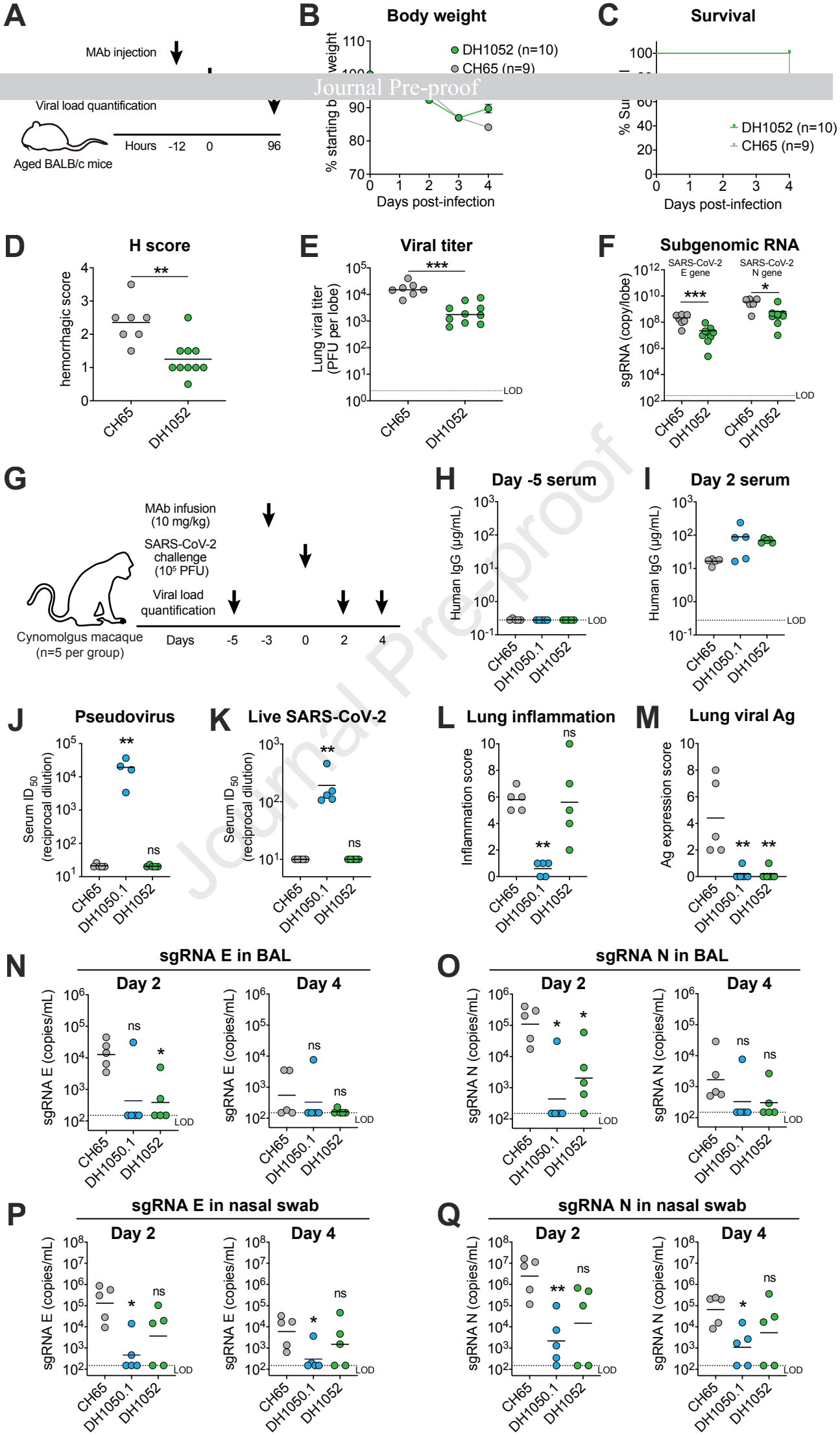

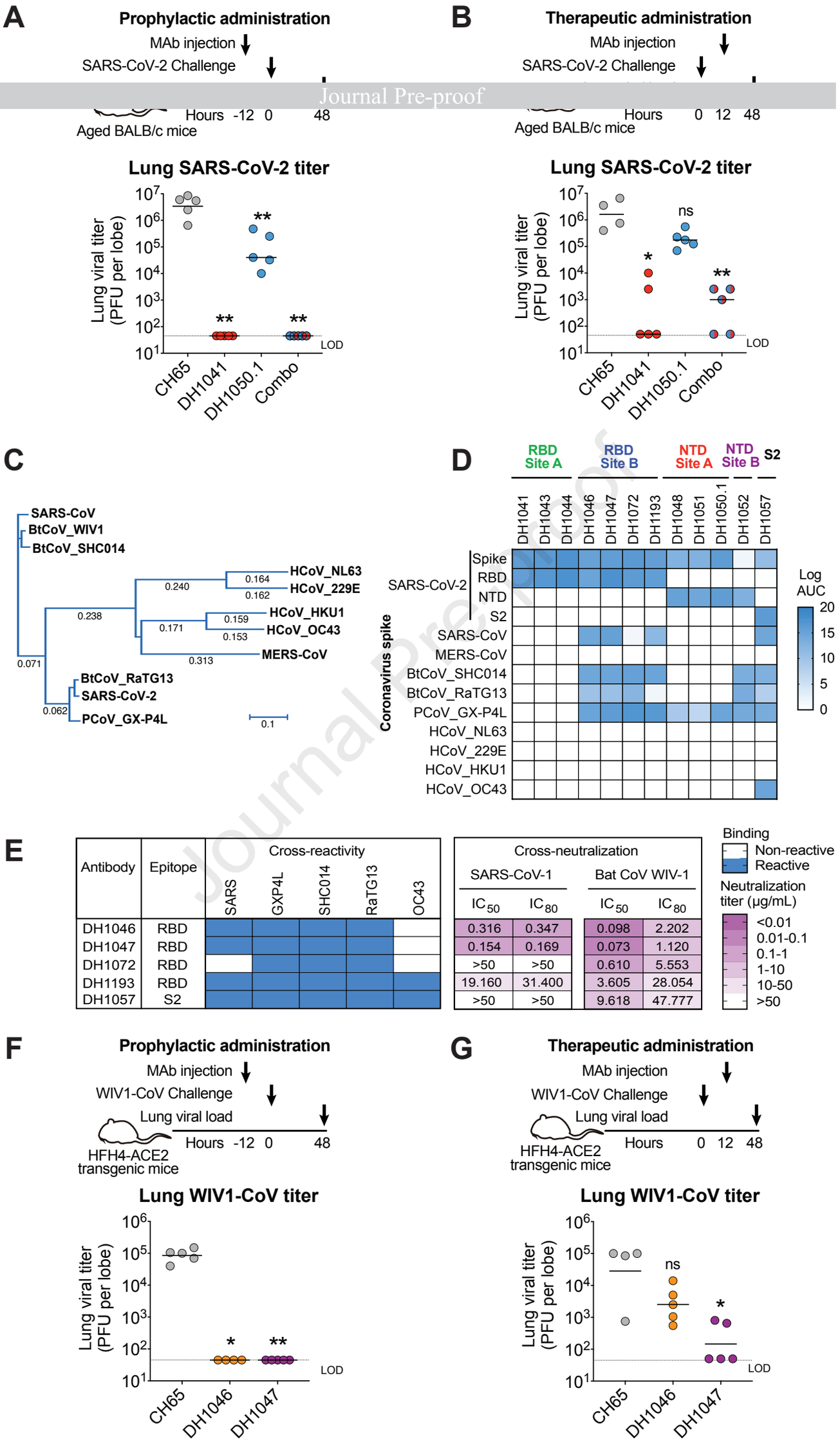

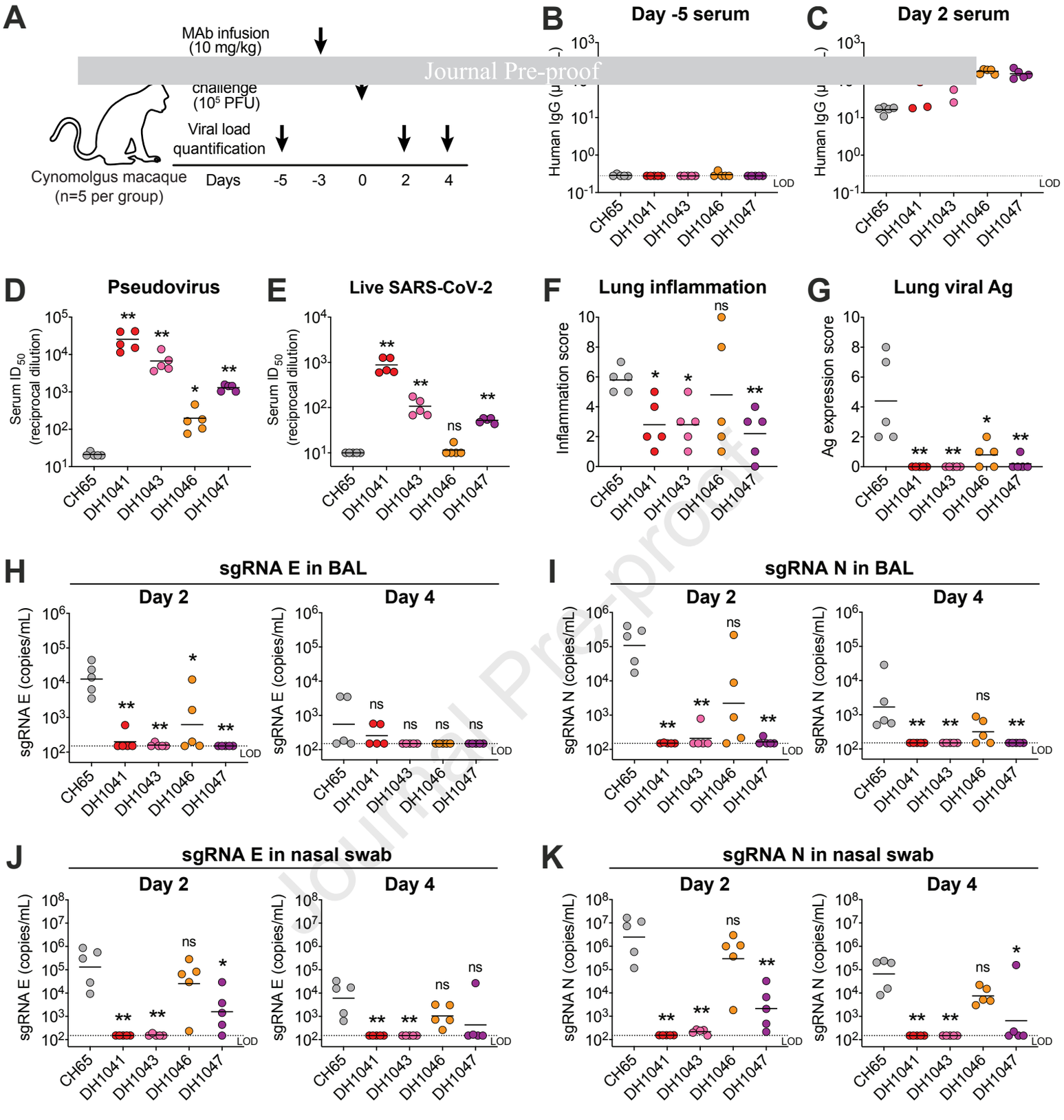

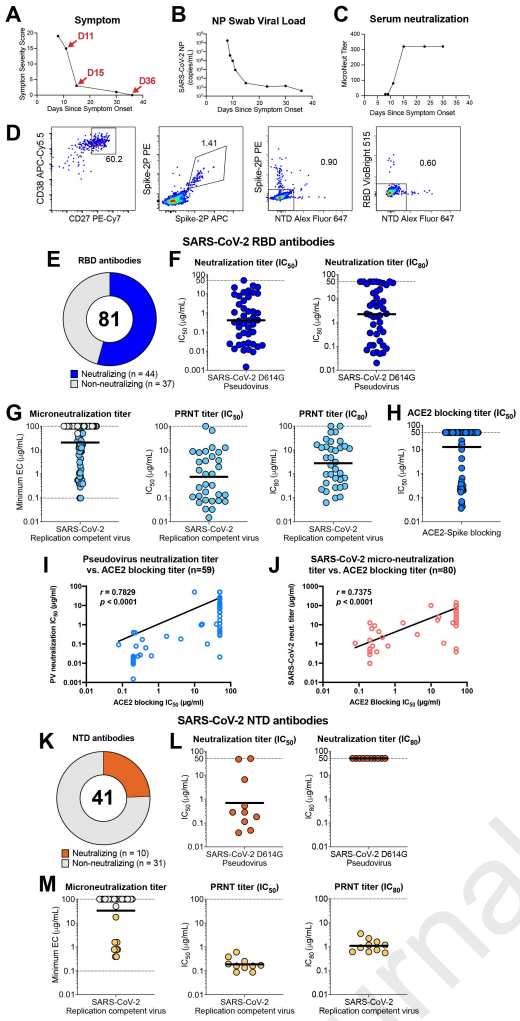

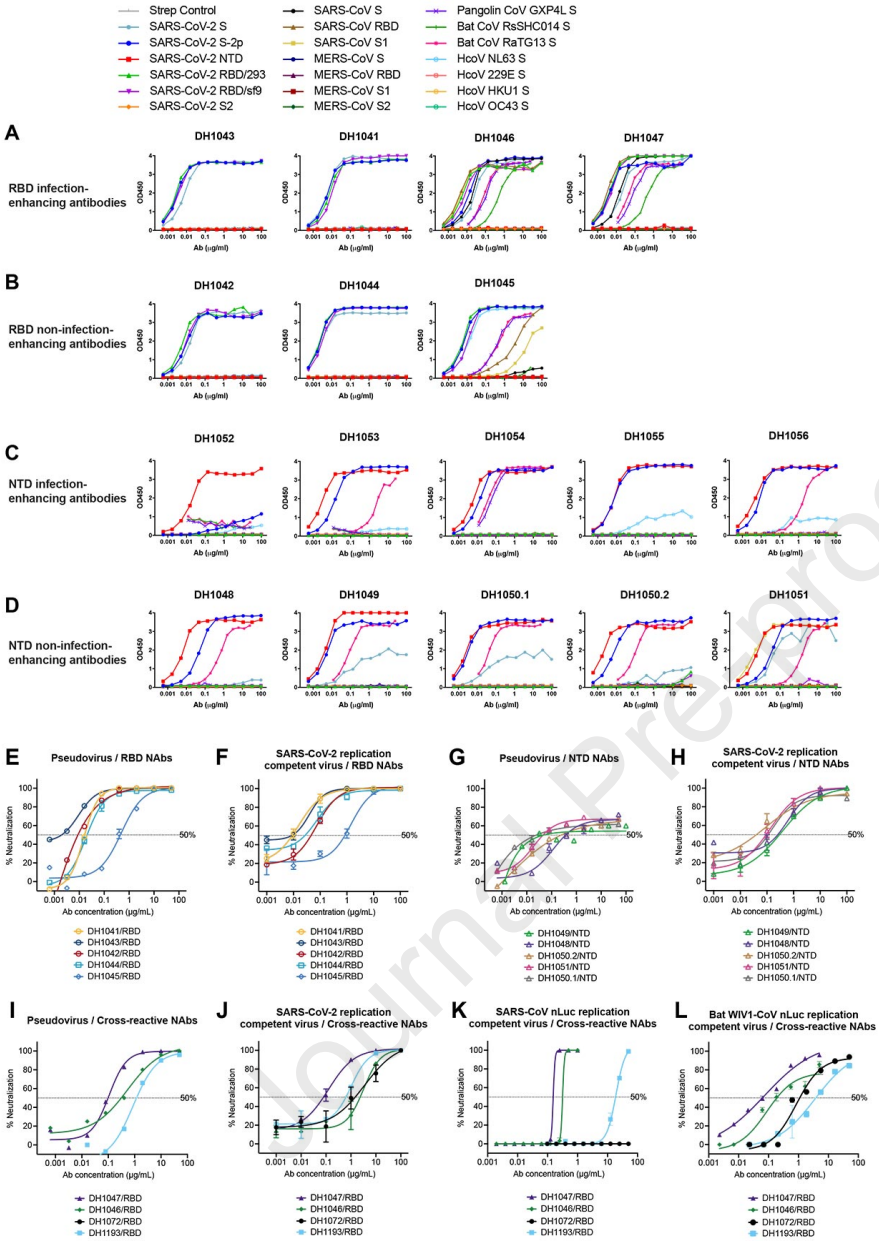

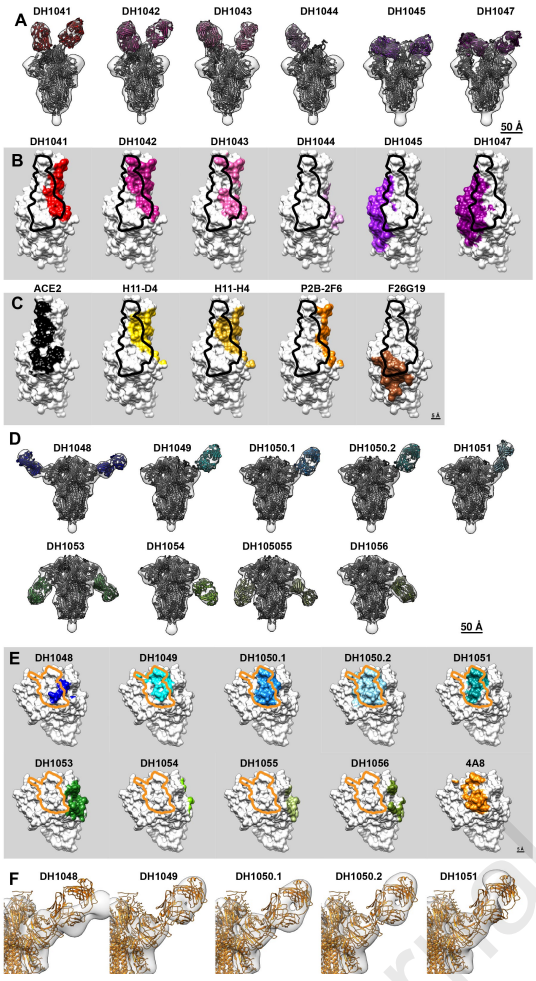

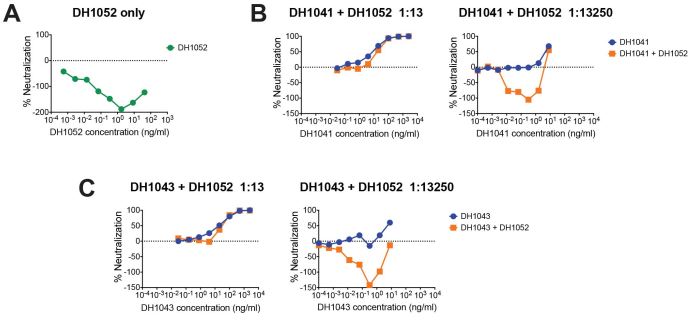

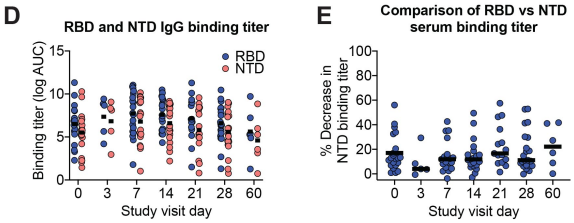

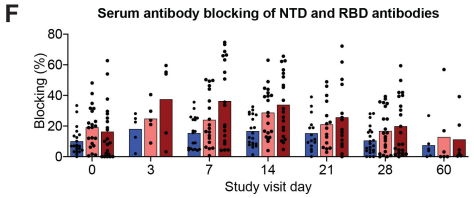

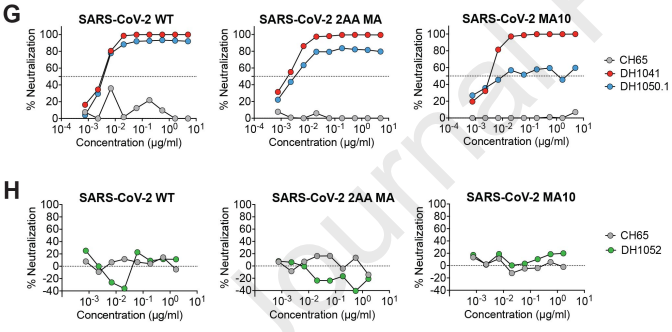

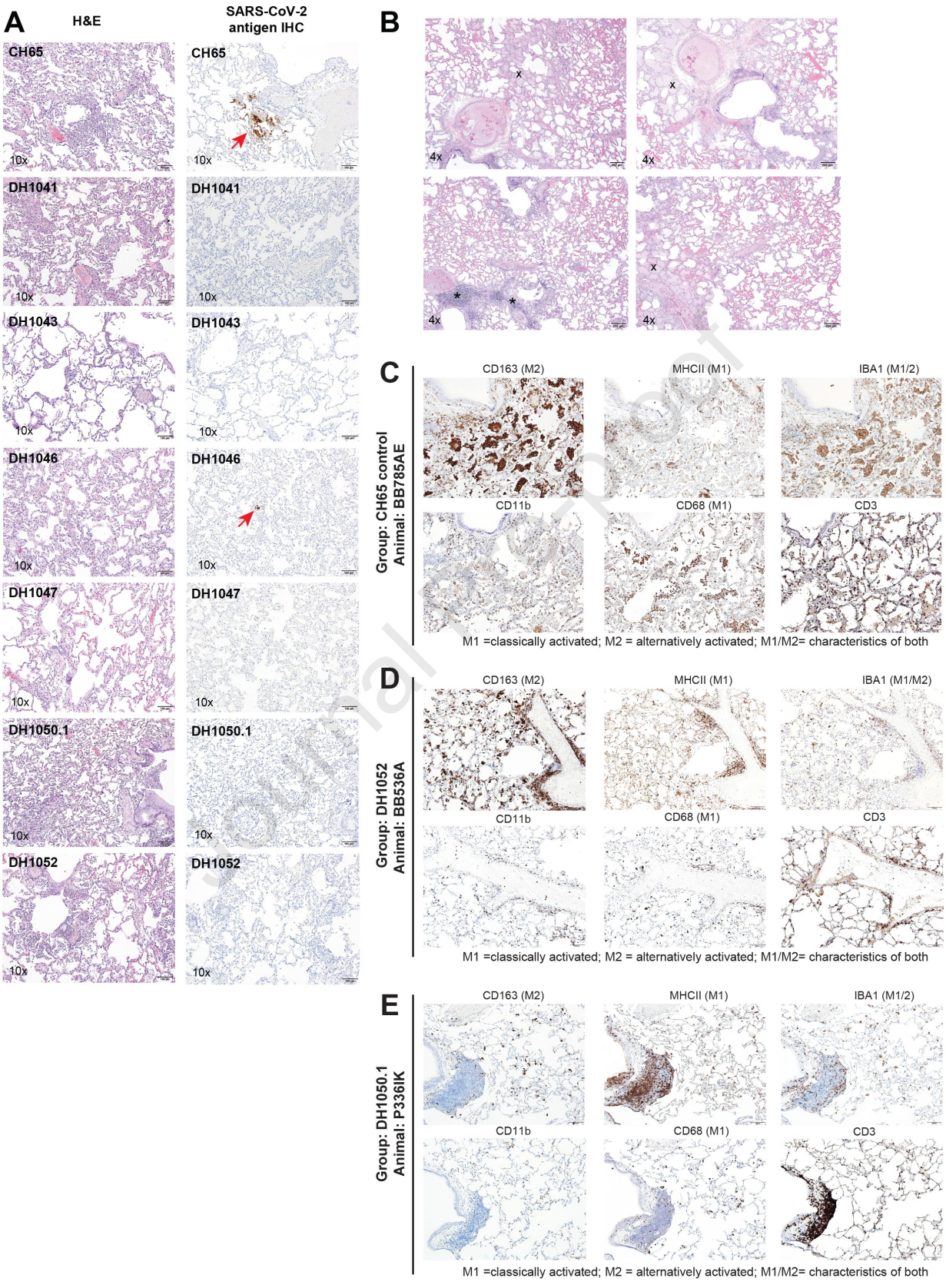
A
H&E
SARS-CoV-2 antigen IHC
CH65
DH1041
DH1043
DH1046
DH1047
DH1050.1
DH1052
10x
B
x
4x
*
C
Group: CH65 control Animal: BB785AE
CD163 (M2)
MHCII (M1)
IBA1 (M1/2)
CD11b
CD68 (M1)
CD3
M1 =classically activated; M2 = alternatively activated; M1/M2= characteristics of both
D
Group: DH1052 Animal: BB536A
E
Group: DH1050.1 Animal: P336IK

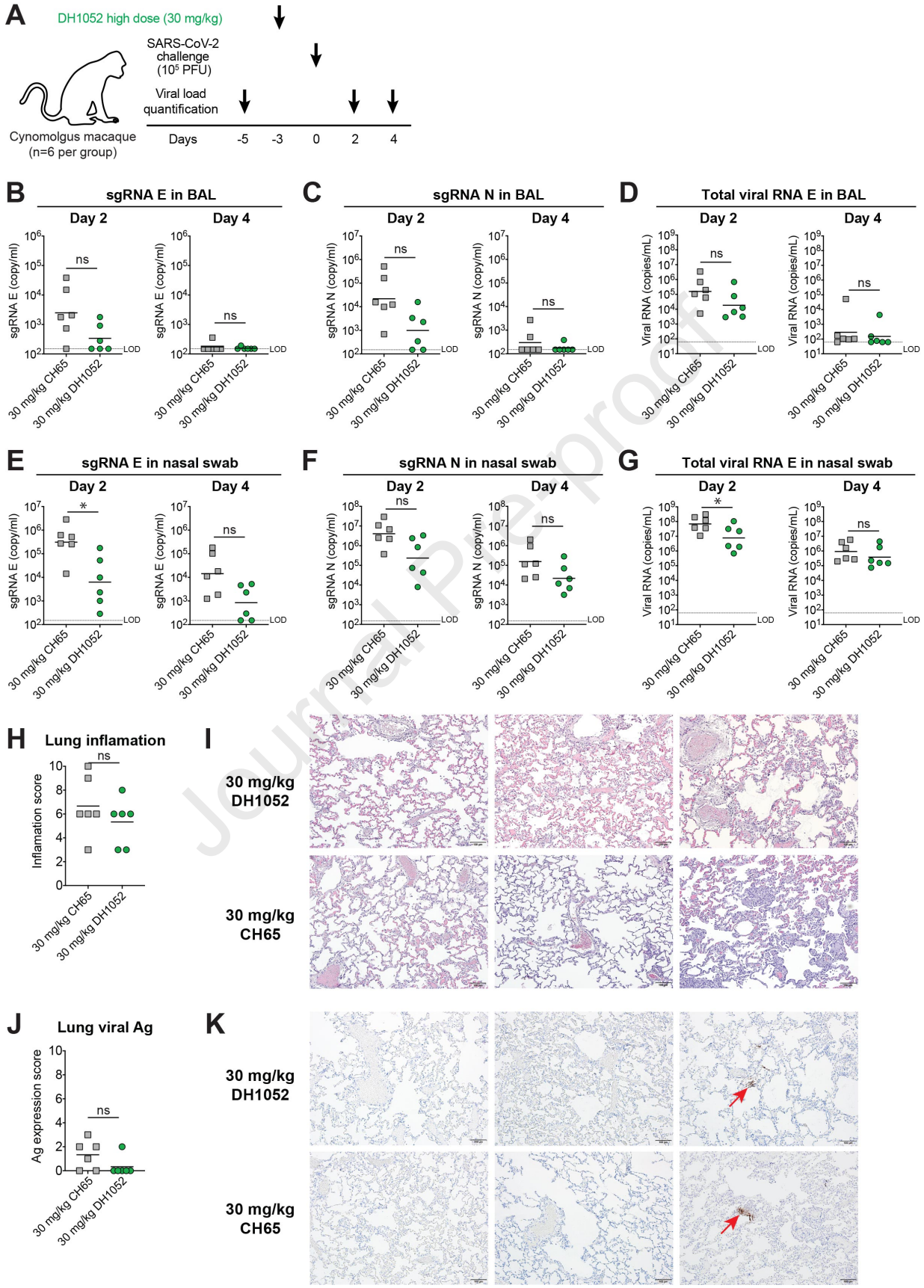

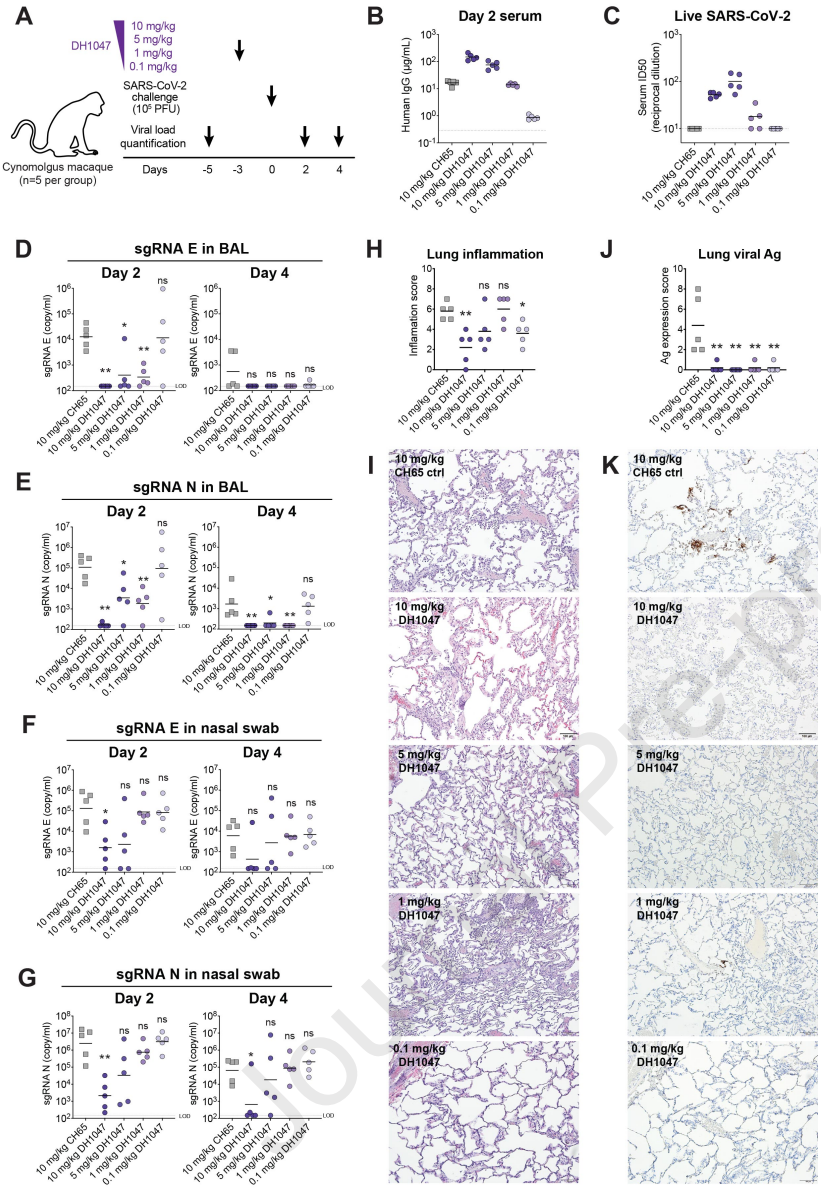

1. Cryo-EM data collection and refinement statistics.

	24MFK DH1041	30MFK DH1052	35MFK DH1047	113KJ DH1043	26MFK DH1050.1
PDB ID	7LAA	7LAB	7LD1	7LJR	7LCN
EMDB ID	EMD-23246	EMD-23248	EMD-23279	EMD-23400	EMD-23277
Data Collection					
Microscope	FEI Titan Krios	FEI Titan Krios	FEI Titan Krios	FEI Titan Krios	FEI Titan Krios
Voltage (kV)	300	300	300	300	300
Electron dose ($e^-/Å^2$)	65.94	66.71	66.77	66.77	65.09
Detector	Gatan K3	Gatan K3	Gatan K3	Gatan K3	Gatan K3
Pixel Size (Å)	1.058	1.058	1.058	1.058	1.058
Defocus Range (μm)	~0.75-2.50	~0.75-2.50	~0.75-2.50	~0.75-2.50	~0.75-2.50
Magnification	81000	81000	81000	81000	81000
Micrographs collected	7362	9375	3440	1900	2154
Reconstruction					
Software	cryoSparc	cryoSparc	cryoSparc	cryoSparc	cryoSparc
Particles	151,384	143,4115	127,401	133,814	426,025
Symmetry	C1	C1	C1	C1	C1
Box size (pix)	350	350	350	350	350
Resolution (Å) (FSC 0.143)*	3.42	2.97	3.4	3.66	3.35
Refinement (Phenix)					
Protein residues	2994	4194	4251	3378	4296
Chimera CC	0.72	0.77	0.79	0.68	0.73
R.m.s. deviations					
Bond lengths (Å)	0.014	0.014	0.012	0.012	0.013
Bond angles (°)	2.235	1.958	1.920	1.899	2.006
Validation					
Molprobity score	1.99	1.25	1.41	1.17	1.53
Clash score	2.19	0.40	0.15	0.23	0.42
Favored rotamers (%)	96.62	98.41	97.65	98.88	97.48
Ramachandran					
Favored regions (%)	88.15	92.97	89.16	90.03	89.05
Allowed regions (%)	10.38	6.50	9.23	9.15	9.36
Disallowed regions (%)	1.47	0.54	1.61	0.82	1.59
EMRinger score	2.68	3.24	2.71	1.95	2.09

*Resolutions are reported according to the FSC 0.143 gold-standard criterion

2. Cryo-EM data processing details.

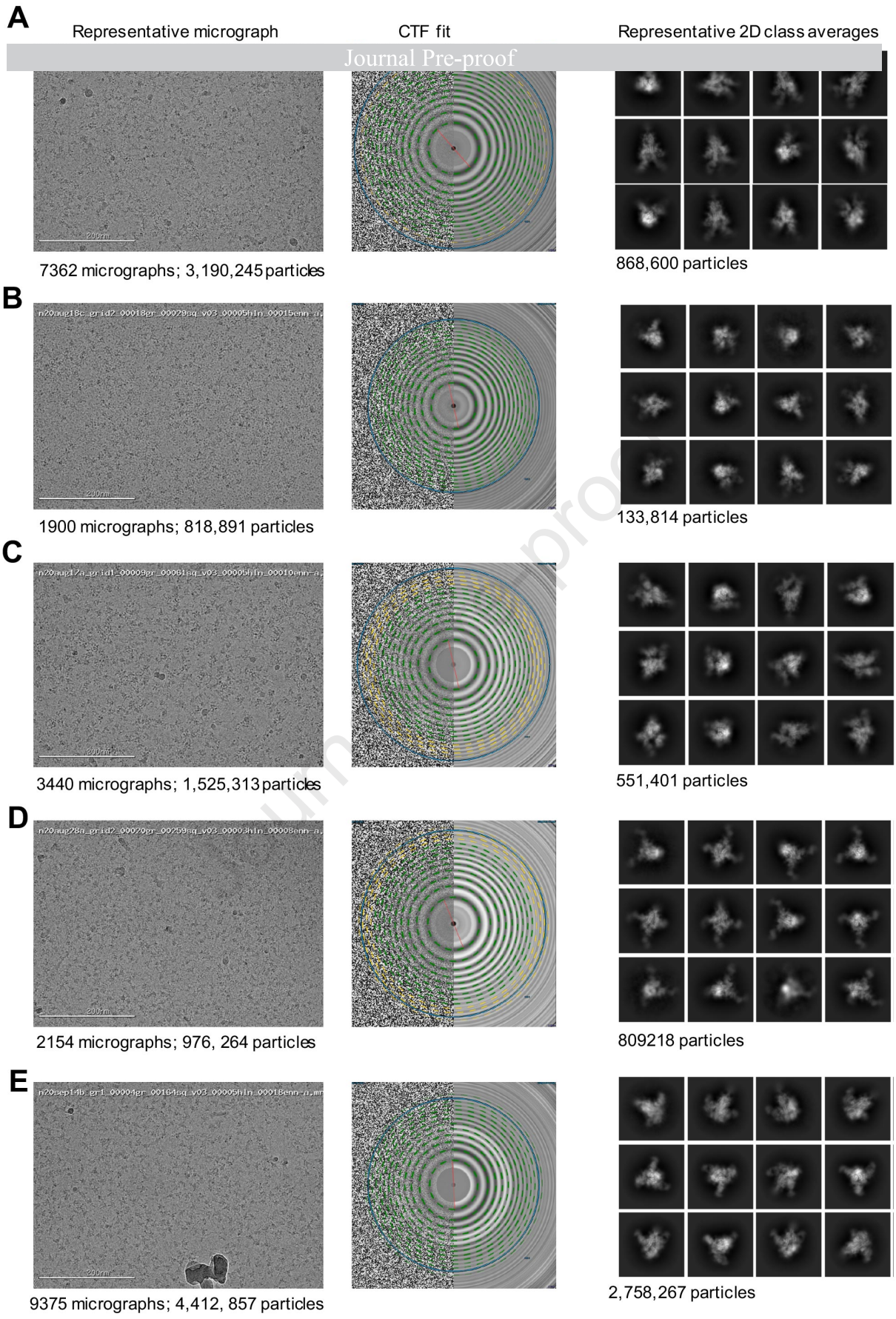

2. Cryo-EM data processing details. (left) Representative micrograph, (middle) CTF fit and (right) Representative 2D class averages for (A) DH1041-Spike-2P (S2P) complex, (B) DH1043-S2P complex, (C) DH1047-S2P complex, (D) DH1050.1-S2P complex, (E) DH1052-S2P complex.

3. Global and Local map resolutions for DH1041/S-2P complex.

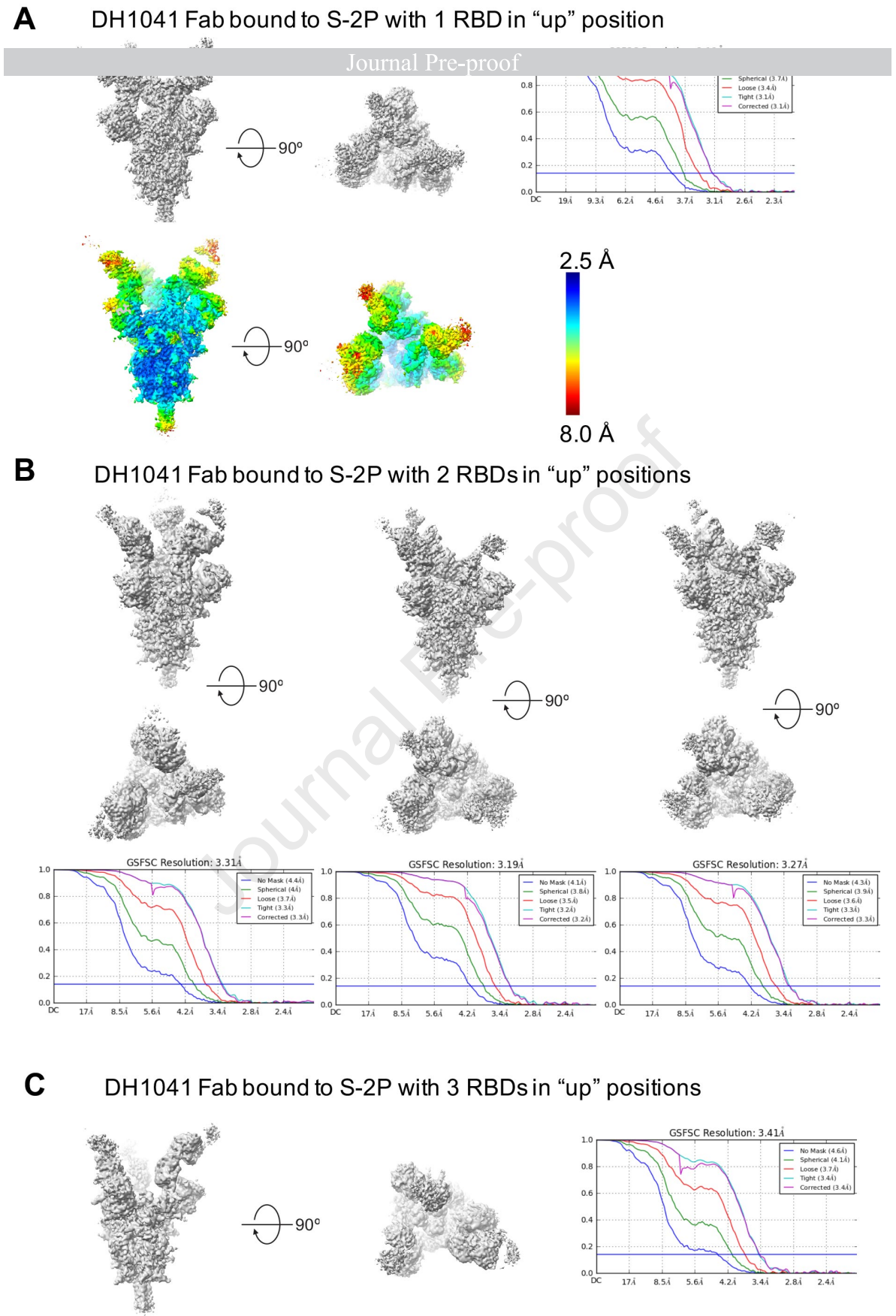

3. Global and Local map resolutions for DH1041/S-2P complex. (A) Cryo-EM reconstruction of DH1041 bound to 1-RBD-up 2P spike. Top row show refined map and FSC curves. Bottom row shows refined colored by local resolution. Zoomed-in view of the S2 region is shown on the right with cryo-EM map shown as blue mesh and underlying fitted model as sticks and colored by element (B) Cryo-EM reconstruction of DH1041 bound to 2-RBD-up 2P spike. (C) Cryo-EM reconstruction of DH1041 bound to 3-RBD-up 2P spike.

4. Global and Local map resolutions for DH1043/S-2P complex.

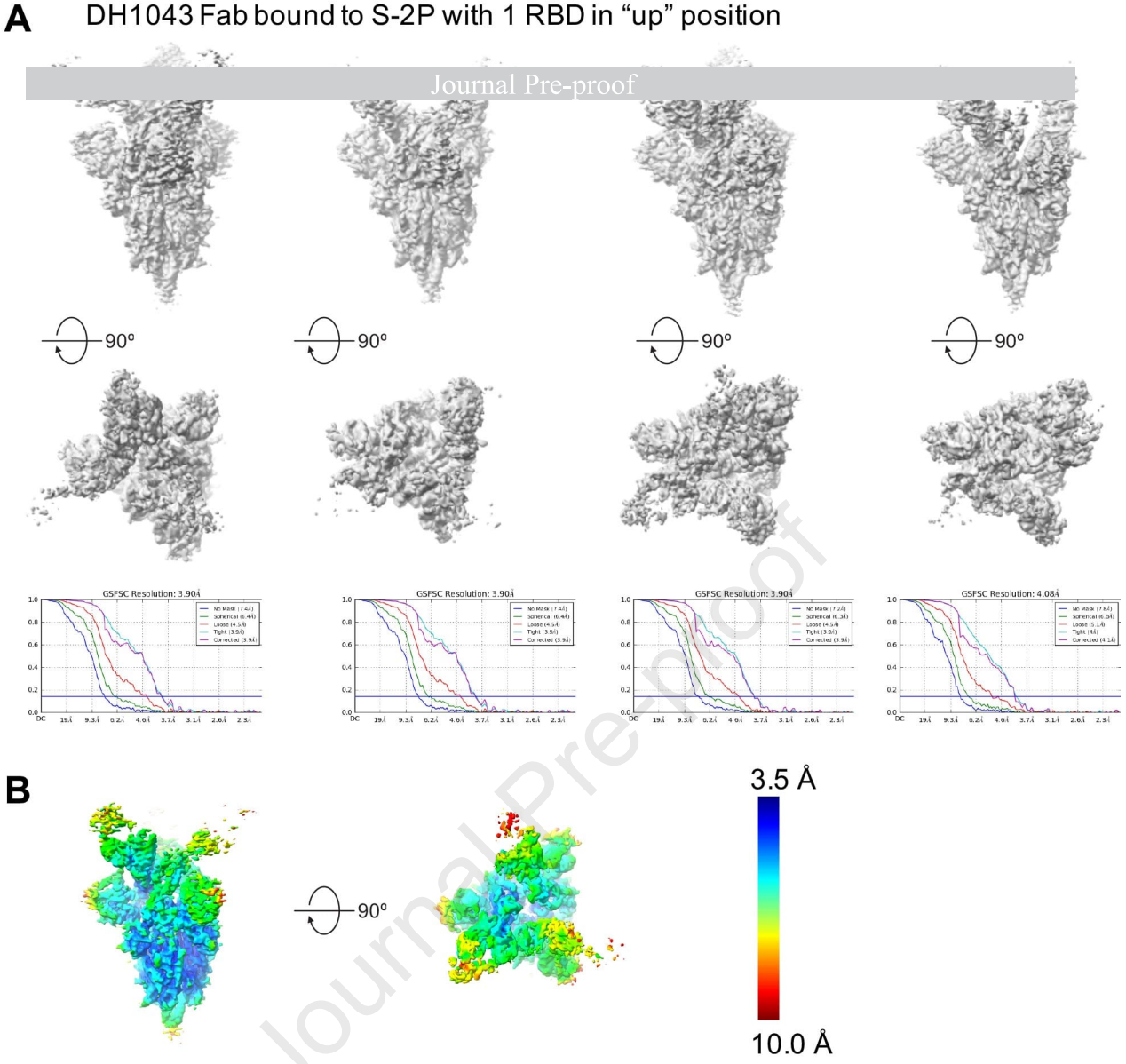

4. Global and Local map resolutions for DH1043/S-2P complex. (A) Cryo-EM reconstructions of DH1043 bound to 1-RBD-up 2P spike Top two rows show refined maps, bottom row shows the FSC curve for each corresponding map. (B) Left. Refined cryo-EM map that was used for model building colored by local resolution. Right. Zoomed-in view of the S2 region with cryo-EM map shown as blue mesh and underlying fitted model as sticks and colored by element. (C) Zoomed-in view of the DH1043 interface with RBD. The cryo-EM map is shown as a blue mesh with underlying fitted model shown in cartoon representation, with the DH1047 HCDR1 loop colored yellow, HCDR2 colored limon, HCDR3 cyan, and LCDR3 light blue.

5. Global and Local map resolutions for DH1047/S-2P complex.

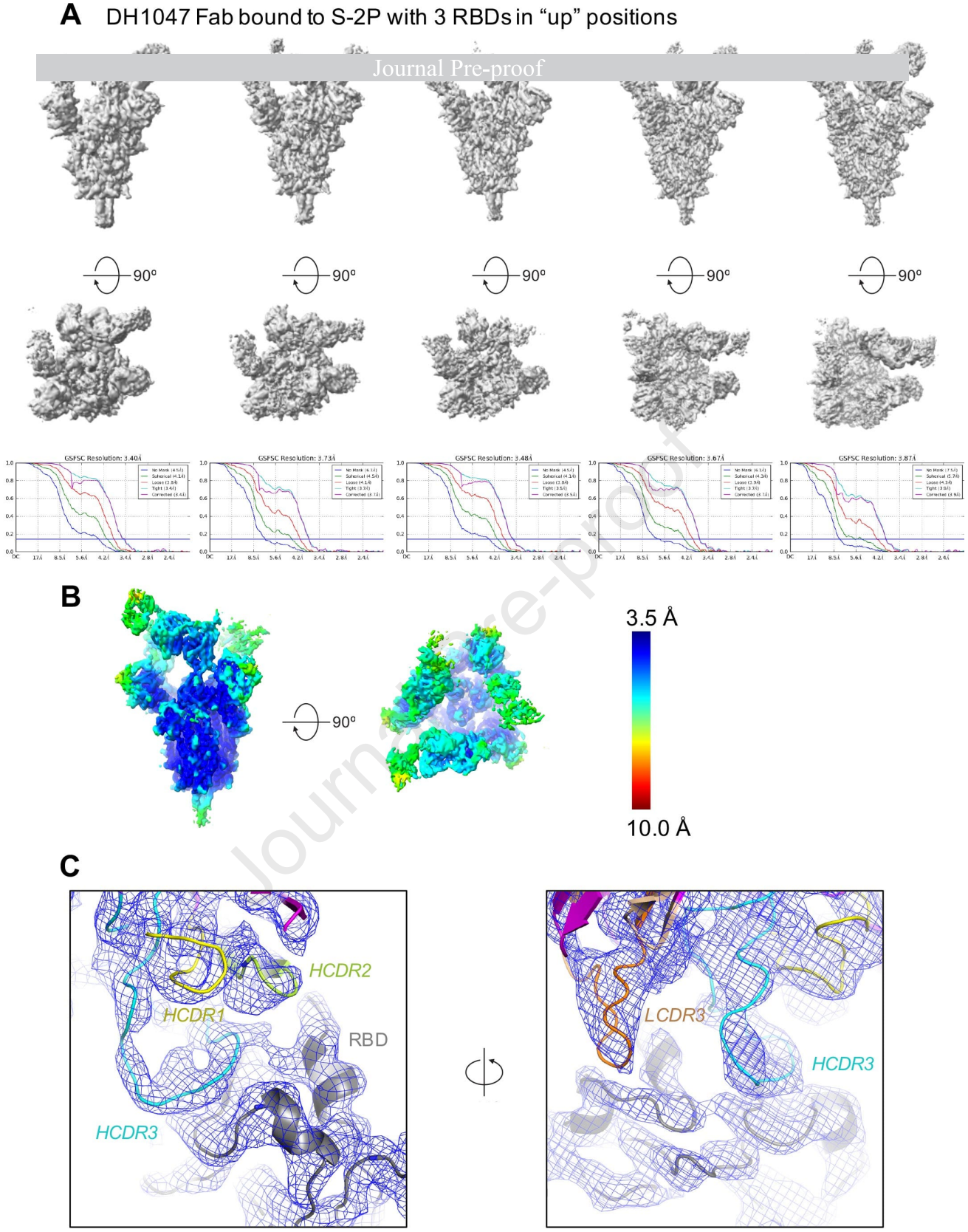

5. Global and Local map resolutions for DH1047/S-2P complex. (A) Cryo-EM reconstructions of DH1047 bound to 3-RBD-up 2P spike. Top two rows show refined maps, bottom row shows the FSC curve for each corresponding map. (B) Left. Refined cryo-EM map that was used for model building colored by local resolution. Right. Zoomed-in view of the S2 region with cryo-EM map shown as blue mesh and underlying fitted model as sticks and colored by element. (C) Zoomed-in view of the DH1047 interface with RBD. The cryo-EM map is shown as a blue mesh with underlying fitted model shown in cartoon representation, with the DH1047 HCDR1 loop colored yellow,HCDR2 colored limon, HCDR3 cyan and LCDR1 orange.

6. Global and Local map resolutions for DH1050.1/S-2P complex.

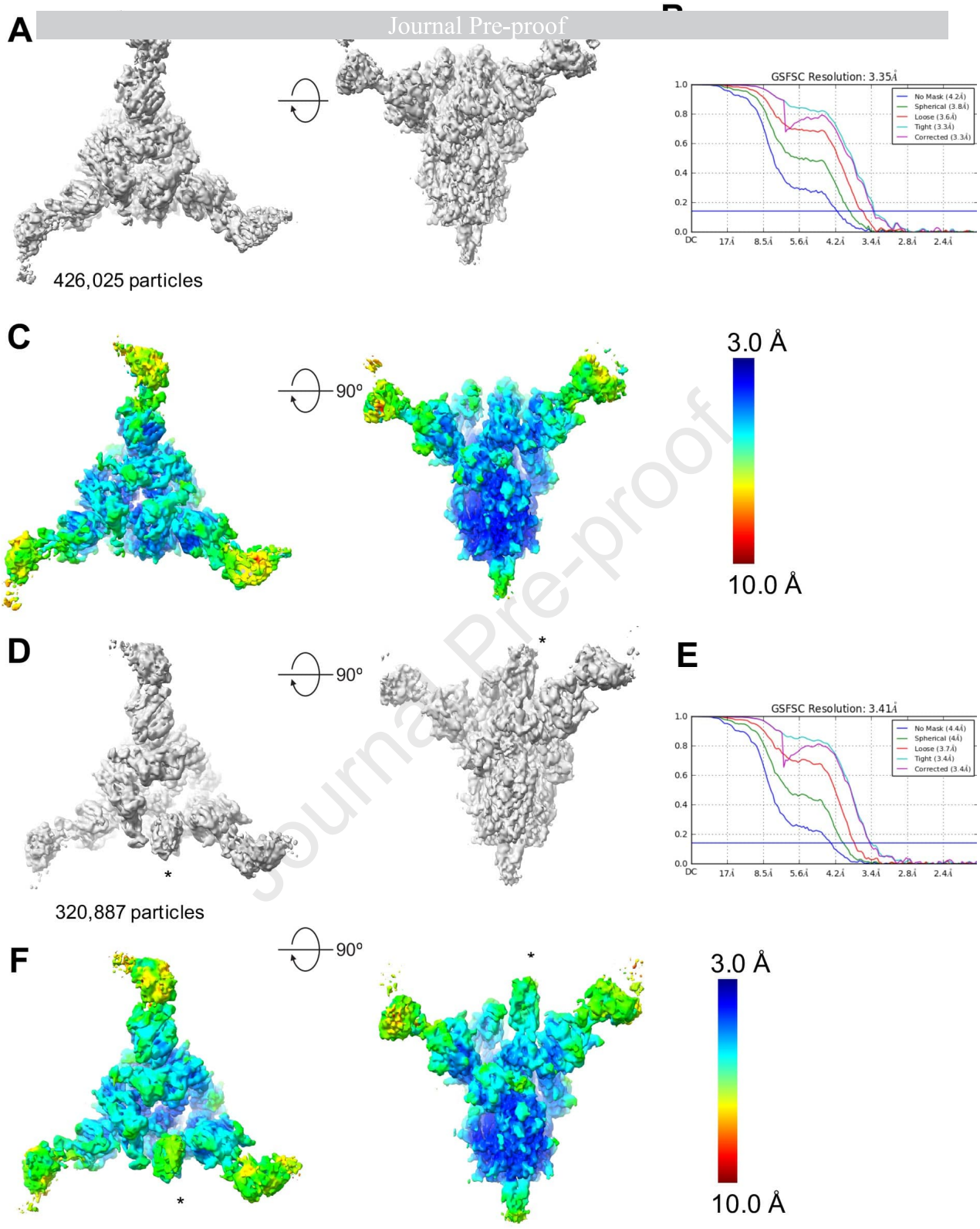

6. Global and Local map resolutions for DH1050.1/S-2P complex. (A) Cryo-EM reconstruction of DH1050.1 bound to 3-RBD-down 2P spike. (B) Fourier shell correlation curves. (C) Left. Refined cryo-EM map colored by local resolution for the DH1050.1 bound to 3-RBD-down 2P spike. Right. Zoomed-in view of the S2 region with cryo-EM map shown as blue mesh and underlying fitted model as sticks and colored by element. (D) Cryo-EM reconstruction of DH1050.1 bound to 1-RBD-up 2P spike. (E) Fourier shell correlation curves. (F) Refined cryo-EM map colored by local resolution for the DH1050.1 bound to 1-RBD-up 2P spike.

7. Global and Local map resolutions for DH1052/S-2P complex.

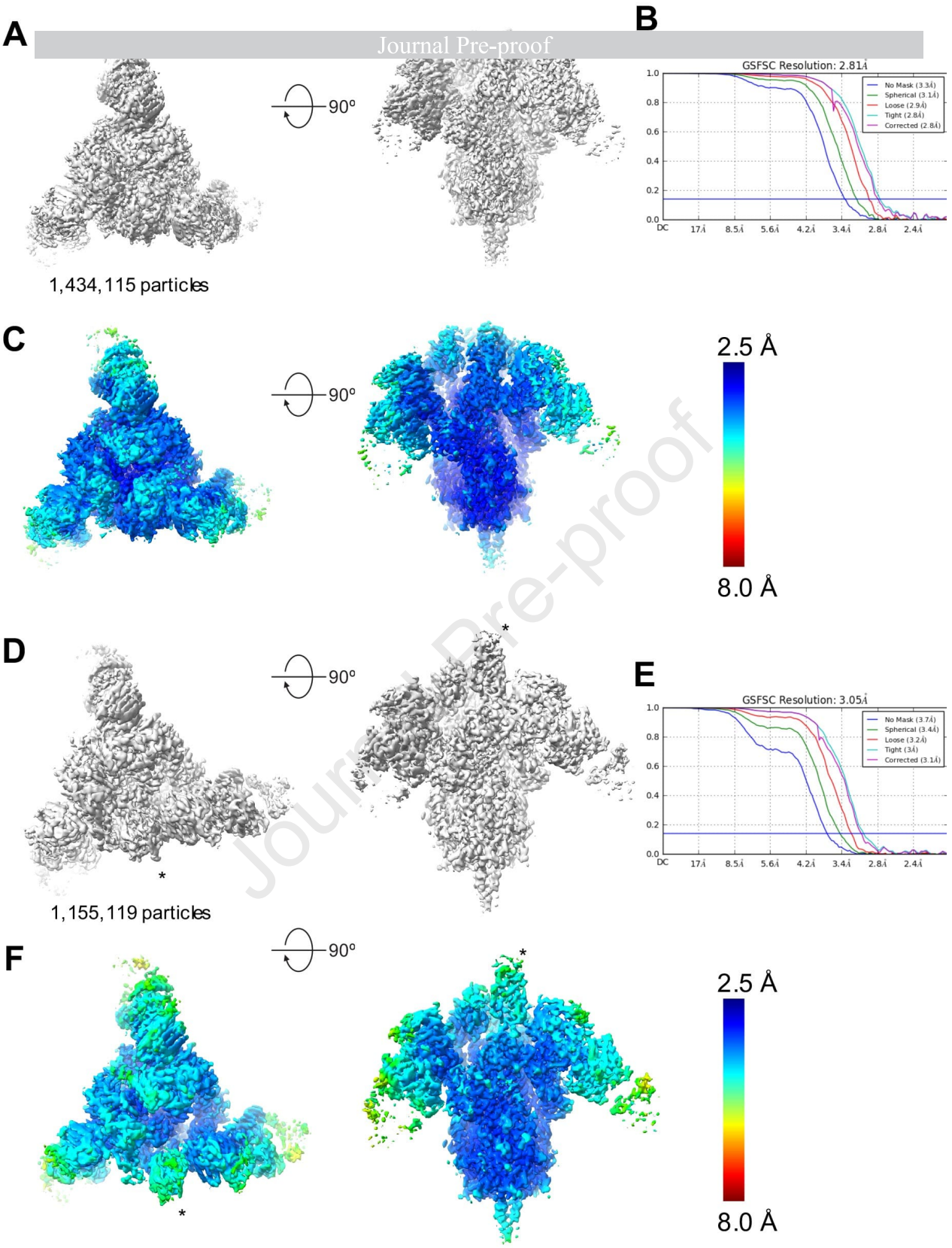

7. Global and Local map resolutions for DH1052/S-2P complex. (A) Cryo-EM reconstruction of DH1052 bound to 3-RBD-down stabilized Spike "2P" (S-2P). (B) Fourier shell correlation curves. (C) Left. Refined cryo-EM map colored by local resolution for the DH1052 bound to 3-RBD-down S-2P. Right. Zoomed-in view of the S2 region with cryo-EM map shown as blue mesh and underlying fitted model as sticks and colored by element. (D) Cryo-EM reconstruction of DH1052 bound to 1-RBD-up S-2P. (E) Fourier shell correlation curves. (F) Refined cryo-EM map colored by local resolution for the DH1052 bound to 1-RBD-up S-2P.